GRAVITATIONAL WAVE DETECTION, DETECTOR CHARACTERIZATION, AND PARAMETER ESTIMATION USING A NETWORK OF INTERFEROMETER DETECTORS

By

AARON MATTHEW ROGAN

A dissertation submitted in partial fulfillment of
the requirements for the degree of

Doctor of Philosophy

Washington State University
Department of Physics And Astronomy

December 2006

To the Faculty of Washington State University:

The members of the Committee appointed to examine the dissertation of Aaron Matthew Rogan find it satisfactory and recommend that it be accepted.

_____

Chair

_____

_____

_____

Acknowledgements

I can not express exactly how important Sukanta Bose has been throughout the course of my research. He has always been there to provide direction when I lost sight of the end goal or just guidance in many instances when I tended to oversimplify matters. He provided what I believe is the best working environment I have ever had the pleasure to be a part of and always was available to me for any reason that I may have needed his support.

Achamveedu Gopakumar has also been a primary source of support for the last part of my dissertation. If not for the discussion with him and if he did not provide the waveforms that were necessary, I can easily say that the work on eccentric binaries would not have been possible in the time it was completed.

I would also like to thank Shawn Seader for the countless number of teleconferences he put up with to get me started with my LIGO work. It was his guidance that really got the ball rolling in that aspect of my dissertation. I would also like to thank Rajesh Nayak for helpful correspondence as well as Massimo Tinto for pointing out to me that in the long-wavelength approximation, the contribution from the GW strain to third pseudo-detector discussed here becomes negligible. If it were not for Curt Cutler's helpful discussions, I could have spent countless hours attempting to find the errors in some of my assumptions on the LISA data.

Thanks are also due to Matthew Mayer, Michael Stoops, Svend Sorensen, Nathan Hearn, George Lake and the WSU IT department for help with computational resources.

GRAVITATIONAL WAVE DETECTION, DETECTOR CHARACTERIZATION, AND PARAMETER ESTIMATION USING A NETWORK OF INTERFEROMETER DETECTORS

Abstract

by Aaron Matthew Rogan, PhD.
Washington State University
December 2006

Chair: Sukanta Bose

Although the existence of gravitational waves have been indirectly proven, the direct detection of the first gravitational wave will mark a significant turning point in the understanding of gravitational waves (GW) and gravity in general. For decades there have been several narrow band bar detectors in operation but it has only been the last decade that the most promising gravitational wave detectors have begun to come online. The broad band detectors possess the ability to see a large portion of the known frequencies that are expected from theories which are physically unavailable to bar detectors.

Considering that GW signals are inherently weak, inspiral signals are very promising sources for both Earth based and space based interferometer detectors due to their known waveforms. The duration that a signal is available to a given detector increases the chances of detection significantly. With several interferometer detectors currently operating across the globe and the commissioning of the first space based detector in the coming years, two of the few remaining hurdles that are covered in this dissertation are maintaining the detector

sensitivity to signals and making the very first direct detection of a GW.

Owning to the fact that these interferometric detectors are composed of some of the most advanced laser systems in existence, they require many monitoring tools that assist in characterizing the state of the detectors. One such tool detailed herein would be GainMon, which is a software tool that allows operators to monitor the long baseline Fabry-Perot cavities for drifts in the unity gain frequencies (UGF).

Once it has been determined that the detector is in an acceptable operating state, the data that it collects must then be studied to determine if a signal is present. If the detector is incapable of recovering source parameters within a certain degree of accuracy then a detection serves as nothing more than a mathematical challenge with little science to be gained. Therefore if a signal is identified, some constraints must be placed on the results that indicate how accurately the recovered signal agrees with the actual source.

Contents

List of Figures

List of Tables

Dedication

This dissertation is dedicated to my father. Although we have not always seen eye to eye, he has always been there when I needed him and helped me through every difficult decision I have ever had to make. Even when he disagreed with the decisions I have made he still stood by me. I would not have come this far without his guidance and support throughout my life.

Chapter 1

Introduction

For millennia now, the stars and the sky have been a source of amazement, curiosity and knowledge. Technological advances like airplanes and automobiles have brought humans closer to each other in a way that could not have been imagined just a few hundred years ago making the Earth seem not so vast as it once was perceived. Similarly, technological advances have brought the heavens closer to us over the centuries as well. When Galileo looked upon the moon's surface for the first time, suddenly Earth's closest satellite was no longer so far out of reach. As telescopic systems advanced, the solar system was increasingly becoming smaller and smaller as our knowledge increased. Although knowledge about the orbits of the planets existed well before the telescope had become an everyday tool for astronomers, what was once no more than a sparkling celestial body had suddenly become almost as defined as the Earth itself. Valleys and craters were apparent on the moon, the rings of Saturn could now be seen and sun spots were finally evident.

For centuries, the telescope has been improved time and time again but for a long time it only provided a single picture of the universe albeit the improvements allowed a deeper

glimpse into the known universe. However, the first images that were obtained with the aid of telescopes would later be proven to be only a small fraction of an enormous "picture". It wasn't until 1932 when Karl Jansky first detected radio waves from the central part of the galaxy that more of the "picture" came into focus [2]. The advent of radio astronomy marked the first new avenue available to astronomers in over 300 years and with this new tool came a whole new understanding of the workings of the universe around us. The development of the optical telescope allowed us to gain a better understanding of objects that were already known to exists. Contrarily, radio telescopes opened our eyes to a universe that could not previously been dreamed. Radio astronomy gave astronomers the ability to see relics of such exotic objects like black holes, pulsars, and radio galaxies.

Astronomy is just now reaching another pinnacle of technology and with it a whole new understanding of the universe will follow. The past decade marks the beginning of a new era in astronomy namely, gravitational wave astronomy. With the first generation of the United States' long baseline gravitational wave detectors just now reaching their design goals, the possibilities are seemingly endless. All astronomy to date has focused on observing the universe using primarily electromagnetic (EM) radiation. Radio astronomy showed the astronomy community that they were not considering all the possibilities that were available in the EM band. Up until now, astronomy focused on simply looking through space-time to gain some understanding of how the universe works and it continues to provide insightful new discoveries. However gravitational radiation is more than just looking at the universe in different wavelengths of light, it is looking at space-time itself. The remarkable distinction between the two methods of observation is electromagnetic radiation is oscillations of electromagnetic fields which propagate through space-time. Gravitational radiation, on

the other hand, is oscillations of space time itself. By measuring these oscillations directly, a more complete picture of the source can possibly be reconstructed. This is important considering that a complete picture of astrophysical sources can can aid in developing a larger "picture" of the universe. Radio astronomy provided the first indirect measurement of a black hole by observing the high frequency EM radiation that the infallling matter generates. However, this is still not a direct measurement of a black hole. Direct measurements of black holes are now possible by precisely measuring the gravitational radiation that they will generate. Gravitational waves can provide a more complete understanding of many other astronomical events as well such as the big bang or supernovae. Just as radio astronomy brought with it more surprises than could have ever been imagined, the most interesting GW sources will be those that have not even been contemplated.

Although there are numerous types of sources that could be available to GW astronomy, one of the more likely candidates for the first detection would be an inspiral source. These sources are comprised of two orbiting compact objects such as white dwarfs (WD), neutron stars (NS) or black holes(BH). Just as EM radiation in produced by accelerating electric charges, GW radiation is generated by accelerating masses. As two compact objects orbit each other about their center of mass, they will impart energy in the form of GW. The loss of energy will result in a reduction in the orbital diameter over time and ultimately cause the merger of the two compact objects. Once the two objects merge they begin to "ringdown", which continues until the now one body achieves a state of equilibrium.

As briefly outlined above, a binary system has three stages of evolution: inspiral, merger and ringdown. However the inspiral stage itself can further be classified into three separate regimes: capture, stationary, and chirping. Each separate regime can be thought of as a part

of the lifetime of the inspiral.

During the capture stage, the inspiral is in its infancy. The two orbiting bodies have just begun to fall towards each other under their mutual gravitational attraction. The gravitational waves emitted during this stage are so small that no current generation GW detector or even any proposed GW detector would be capable of measuring the GW generated at this point in the inspiral. The two compact objects are orbiting at astronomical distances on the order of light years and because of the enormous separations, which results in extremely small GW emission frequencies that are well outside the bandwidth of any current or proposed GW detector. This is by far the longest stage of the inspiral with the source spending millions of years evolving before it would pass into a detectable bandwidth. The amplitude of the GW emissions, length of time spent in any given stage and emission frequency vary drastically depending on the mass of the sources.

Although older forms of GW detectors have been around for years, namely bar detectors, they suffered from intrinsic problems which has prevented any detection to date. Considering the fact that gravitational wave amplitudes are so small, the displacements that need to be measured are proportional to the size of the detector as follows:

$$\Delta L = hL \tag{1.1}$$

where L is the overall length of the detector and h is the signal amplitude. With typical signal amplitudes on the order of 10^{-21} and bar detectors measuring at most a few meters long, the problem becomes attempting to measure length changes smaller than 10 billionths the size of a hydrogen atom. To make matters worse, bar detectors are only sensitive to GW with wavelengths comparable the length of the bar itself. This means that a bar detector

can only see signals in a very narrow band that also have a significantly large amplitude. To combat this issue, the creation of long baseline interferometric detectors was suggested and is now being implemented. These Earth based detectors now employ the use of a Michelson interferometer with arms as long as 4 km. To increase the overall displacements that would be measured many of these detectors utilize a technique known as power recycling whereby they recycle the laser in long Fabry-Perot cavities in an effort to increase the overall effective length of the arms from several kilometers to hundreds of kilometers.

Owing to the fact that a Michelson interferometer is highly sensitive to changes in arm length, interferometric detectors have a significantly larger band of frequencies for which they remain sensitive compared to bar detectors. For example, the Laser Interferometer Gravitational Wave Observatory (LIGO) is sensitive to frequencies ranging from tens of Hz up to several thousand Hz in contrast to the AURIGA [1] resonant bar detector whose frequency band ranges from around 905 Hz to 940 Hz. However, a large portion of known sources will emit GW well beyond the range of frequencies that both of the aforementioned detectors are capable of observing. To combat this issue, the Laser Interferometer Space Antenna (LISA) is scheduled to be flown in the coming decade. This is a space-based version of the Earth based interferometric detectors. However, LISA will have 5 million km arm lengths, which will further increases the size of the measured displacements. Consequently, this will also increase the chances of detection. LISA will be sensitive to frequencies ranging from 0.1 mHz to 1 Hz and within this frequency range there are several guaranteed sources that will be available.

Although interferometry is a well established technology, the remaining challenges are to maintain the detector sensitivity, accurately identify a GW signal and then place bounds on

the accuracy of the extracted parameters. This dissertation will cover the entire strategy of detecting a gravitational wave starting from the theory of gravitational waves to maintaining the GW detectors to the challenges involved with the real time searches currently being implemented. All of these topics will be discussed in great detail in the coming chapters.

The second chapter contains all the relevant background material that will be necessary to understand the remaining chapters. This chapter will outline the fundamentals of gravitational radiation as derived from the the General Relativity principles over 100 years ago as well as an introduction to some of the new developments that have occurred over the past few decades including the principles behind how an interferometer can be used to detect gravitational waves.

The data analysis software for searches using the LIGO interferometers has been established and in production mode for several years now. This software provides users the ability to perform a variety of tasks as well as a variety of searches. The development of the LISA Data Analysis Software Package (LDASP) was driven by the desire to have a similar software suite available for LISA data analysis. The current software outlined in chapter 3 is the first generation of a series of packages that will provide the same utilities that are currently available for the earth based interferometers.

The development of the first optimal statistic for searching for gravitational waves using LISA is outlined in chapter 4. This was the first optimal statistic to be presented to the gravitational data analysis community. The optimal statistic presented in chapter 4 is the only statistic that is defined in the frequency domain so as to make use of the Fast Fourier Transform (FFT) algorithms currently available to real time searches. This statistic incorporates all of LISA dynamics including TDIs and Doppler shifting of the central frequency.

Chapter 5 outlines how accurately LISA will function ,as a gravitational wave detector. This work is unique in that no others have truly modeled the response function of LISA when trying to model LISA's parameter extraction capabilities. By properly accounting for the TDIs and frequency dependance of the response functions, one obtains vastly different parameter errors. This is outlines in a little more detail in the appendix where the parameter errors using eccentric waveforms are obtained. These results are for the simple toy model that has been used throughout the literature to date. A direct comparison with those results obtained in chapter 5 illustrates the vast differences that arise when not properly tracking all of LISA's dynamics.

A real time coherent search using LIGO has been the driving force behind Washington State University's Relativity group since its inception. The backbones were established previously but the code was never properly tested and tuned to the point where it was ready to be integrated into the real time searches. Chapter 6 outlines the final development, testing and tuning of the coherent section of the real time search pipeline. Along side of this, the software tool known as GainMon is also presented. This is the first software of its kind that is used to monitor the unity gain frequency of all LIGO interferometers in an effort to maintain the maximum amount of all interferometer's operational time.

Chapter 2

Gravitational Wave Physics

2.1 What is a metric?

The metric is one of the most important mathematical tools in General Relativity. A metric is a measure of the distance between any two points in a given space-time [3, 5]. The metric contains all the geometry of a specific space-time. For example, a common metric encountered in special relativity is the flat metric, $\eta_{\mu\nu}$. This flat metric is often used to measure the separation between any two space-time events as follows:

$$ds^2 = -dx^{0^2} + dx^{1^2} + dx^{2^2} + dx^{3^2} = \eta_{\mu\nu} dx^\mu dx^\nu \tag{2.1}$$

where μ and ν are indices ranging from 0 to 3. The flat metric, η, has componets that take the form

$$\eta_{\alpha\beta} = \begin{pmatrix} -1 & 0 & 0 & 0 \\ 0 & 1 & 0 & 0 \\ 0 & 0 & 1 & 0 \\ 0 & 0 & 0 & 1 \end{pmatrix}. \tag{2.2}$$

The incorporation of the effects of mass distributions into the theory of Special Relativity resulted in the development of General Relativity. In most cases, except when near an extremely compact object, the space-time can be expressed as nearly flat with small perturbations to the metric introduced in eq. 2.2 as follows:

$$g_{\alpha\beta} = \eta_{\alpha\beta} + h_{\alpha\beta}. \tag{2.3}$$

This is the metric tensor that will be used primarily throughout this chapter and later chapters unless otherwise specified.

The effects of mass on the surrounding space-time is determined by using Einstein's Field Equations, which are analogous to the inhomogeneous wave equation in electromagnetism. The field equations, which yield the space-time dynamics, can be expressed in terms of the Einstein Tensor, G, and the Stress-Energy Tensor, T. In geometrized units, the field equations take the following form:

$$G^{\alpha\beta} = 8\pi T^{\alpha\beta}. \tag{2.4}$$

Equation 2.4 is actually a more compact representation of a total of 16 coupled equations. As with electromagnetism, the proper choice of gauge can help simplify the field equations and from those simplified equations the gravitational wave solutions follows. The common gauge choice used is the transverse traceless gauge (TT gauge). In this gauge, the Einstein tensor is related to the metric perturbations as such:

$$G^{\alpha\beta} = -\frac{1}{2}\left(-\frac{\partial^2}{\partial t^2} + \nabla^2\right) h^{TT\,\alpha\beta}. \tag{2.5}$$

Now for the vacuum solution, the left side of eq. 2.4 is zero leaving the following wave

equation $\left(-\frac{\partial^2}{\partial t^2} + \nabla^2\right) h^{TT\alpha\beta} = 0$, which has a solution that takes a form similar to that in electromagnetism. If $\vec{k}$ is a null vector whose components can be written as, $\vec{k} = \{\omega, \mathbf{x}\}$, then one obtains $h^{TT\alpha\beta} = \Re\left[A^{\alpha\beta} e^{ik^\gamma x_\gamma}\right]$ as the plane wave solution to the wave equation. In the TT gauge, the solution to the wave equation must obey the following constraint:

$$A^{\alpha\beta} k_\beta = 0, \tag{2.6}$$

which implies that $A^{\alpha\beta}$ must be orthogonal to $\vec{k}$ and therefore $A^{\alpha 0}$=$A^{\alpha 3}$ for a wave traveling in the x^3 direction [4]. The TT gauge imposes two further restrictions on the plane wave amplitude:

$$A^\alpha_\alpha = 0 \tag{2.7}$$

$$A_{\alpha\beta} U^\beta = 0, \tag{2.8}$$

where U^β is a constant four velocity [3]. These are further restrictions in the transverse traceless gauge. Equation 2.7 implies that the amplitude matrix is traceless while eq. 2.6 and eq. 2.8 imply that the wave amplitude is transverse to the direction of propagation. In this gauge, the amplitude matrix has only two independent components. For a wave traveling in the z direction, the amplitude matrix takes the following form:

$$(A^{TT}_{\alpha\beta}) = \begin{pmatrix} 0 & 0 & 0 & 0 \\ 0 & A_{xx} & A_{xy} & 0 \\ 0 & A_{xy} & -A_{xx} & 0 \\ 0 & 0 & 0 & 0 \end{pmatrix}. \tag{2.9}$$

These two independent components of the amplitude matrix represent two independent polarization states.

The effects of the individual polarizations can be seen in fig. 2.1. The top panel rep-

resents the "plus" (A_{xx}) polarization while the bottom figure represents the "cross" (A_{xy}) polarization. The difference between electromagnetic radiation and gravitational radiation are most evident from the two polarization states. Electromagnetic radiation polarization states are rotated by 90 degrees with respect to each other as opposed to 45 degrees as with gravitational radiation. This difference arises from the varying spins between the graviton and the photon [6].

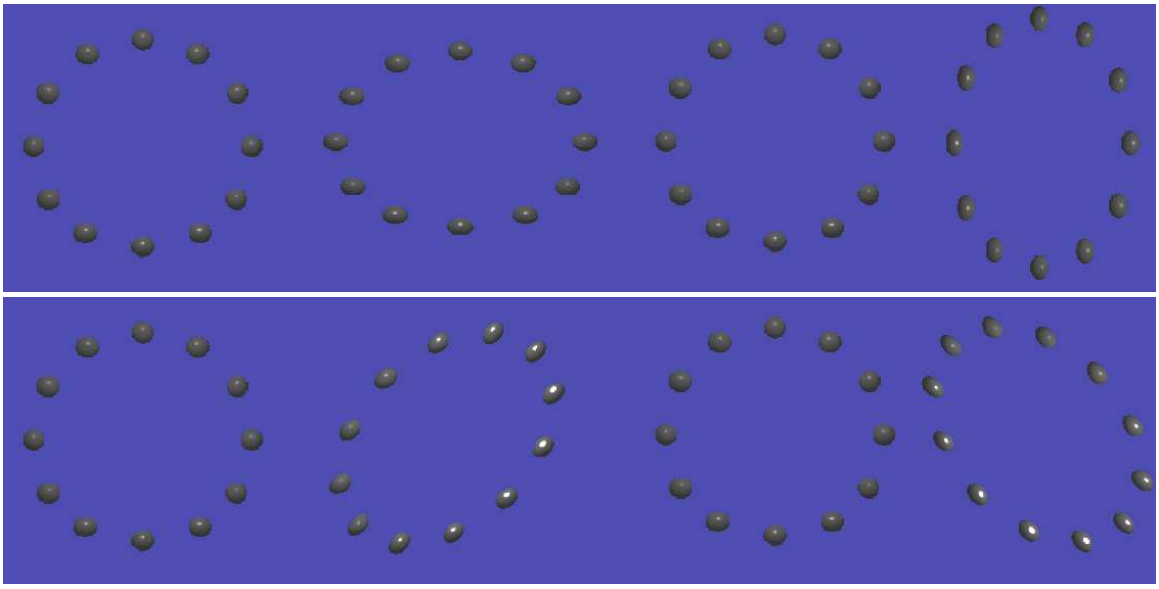

Figure 2.1: These figures illustrate the effect that an impinging gravitational wave would have on a set of freely falling test masses. The top panel illustrates the effects of the plus polarization and the bottom panel illustrates the effects of the cross polarization both for only 3/4 of a wavelength.

2.2 Sources of Gravitational Waves

Just as accelerating charges produce electromagnetic radiation, accelerating masses produce gravitational radiation and similarly there is neither electromagnetic or gravitational monopole radiation. Conservation of mass is what prohibits any monopole radiation but con-

servation of momentum further restricts gravitational radiation to be at least quadrupolar. It can be shown that the quadrupole term, when present, is most dominant in the generation of gravitational waves as the dipole term, when present, is most dominant in the generation of electromagnetic waves. For the sources considered herein, the "quadrupole approximation" is used. The approximation maintains only the quadrupole term in the gravitational potential expansion. This approximation is valid when the size of the source, l, is small compared to the reduced wavelength, λ, it emits [7]. This is the case for all the sources that will be discussed throughout this dissertation.

In this quadrupole approximation, sources with a time varying quadrupole moment will generate gravitational waves. In geometrized units, the metric perturbation is directly proportional to the second time derivative of the moment of inertial tensor as illustrated in eq. 2.10.

$$h_{jk}^{TT} = \frac{2}{r}\ddot{I}_{jk}. \tag{2.10}$$

In eq. 2.10, r is the distance to the source and I_{jk} is the moment of inertia tensor.

Considering how promising inspiral sources are, they will be discussed in great detail throughout the remaining chapters. In general, an inspiral can be broken up into three distinct stages: capture, stationary, and chirping. Each one of these three stages represent a distinct class of signals all in of themselves. Some of these signals are detectable by currently operating GW detectors such as LIGO whereas some would be detectable by the space-based version LISA. However, there are still some signals that neither LISA or LIGO would be able to detect. Before delving into the characterization of these three distinct inspiral stages, the mechanics of the inspiral evolution needs to be addressed.

Qualitatively, the amplitude of the radiation emitted by a binary system can be expressed as follows:

$$h \sim \frac{\mathcal{M}^{5/3} f^{2/3}}{r}, \tag{2.11}$$

where $\mathcal{M} = m_1^{3/5} m_2^{3/5}/(m_1 + m_2)^{1/5}$ is the chirp mass and f is the frequency of the emitted GW. From eq. 2.11 it can be seen that highly eccentric orbits would emit a large portion of their radiation near the pericenter or when the binaries are closest. Therefore, the release of energy at pericenter would act as an impulse which would maintain the pericenter distance while the apocenter distance would decrease [8]. Thus for highly eccentric orbits, the gravitational radiation would circularize the orbits over time. A more precise calculation of how fast the semi major axis changes was first developed by Peters. It was found that the rate of change of the semi-major axes of a binary inspiral to be as follows in SI units:

$$\langle \frac{da}{dt} \rangle = \frac{-64}{5} \frac{G^3 \mu M^2}{c^5 a^3 (1-e^2)^{7/2}} \left(1 + \frac{73}{24} e^2 + \frac{37}{96} e^4\right) \tag{2.12}$$

where μ is the reduced mass and M is the total mass. For circular orbits, the frequency of the emitted gravitational waves are twice the orbital frequency or $f_{GW} = \left(\frac{GM}{\pi^2 a^3}\right)^{1/2}$ which yields the following:

$$\frac{da}{df} = -\frac{2}{3} (GM/\pi^2)^{1/3} f^{-5/3} \tag{2.13}$$

and implies

$$\dot{f} = \frac{96}{5} \pi^{8/3} \left(\frac{G\mathcal{M}}{c^3}\right)^{5/3} f^{11/3} \tag{2.14}$$

These equations provide two very important insights into binary inspirals, the further the

separation of the individual masses then the longer they spend at a given frequency and the lower the total mass of the system then the longer the binary will remain at the same separation.

2.2.1 The Wonder Years

The capture stage is the earliest stage of an inspiral. The beginning of this stage can be classified as the point when when two massive objects just begin to fall in towards each other under their mutual gravitational attraction. Inspirals spend a majority of their lifetime in this stage of the inspiral. In this stage of the inspiral, the two constituent masses are very far apart and remain at the same frequency for a large majority of the inspiral lifetime. Looking at eq. 2.13 and 2.14 for a binary white dwarf system of with $M = 0.6M_{\odot}$ emitting GW at .01 mHz, one can infer that it would take nearly the Hubble time for that system to merge. On the opposite end of the spectrum, super massive black holes will capture each other at a significantly larger separation distance than a white dwarf binary and therefore would also spend a large portion of their time at even lower frequencies. This stage of binary inspirals can therefore be classified as binaries with frequencies below 0.01 mHz. The higher mass binaries will have correspondingly lower frequencies with smaller mass binaries having corresponding larger frequencies within this inspiral classification. Although this stage of binary inspirals are currently beyond the realm of detection, these are possibly the most populated type of inspiral sources considering the length of time that is spent at this early stage of evolution.

2.2.2 Midlife Crisis

The stationary stage of a inspiral evolution is the stage where the inspiral frequencies are large enough so that they would be currently detectable by a space-based GW detector such as LISA. These binary systems have begun to circularize and are emitting GW at frequencies upwards of 0.01 mHz. The orbital separation of these inspirals are significantly closer than with the capture sources and the frequencies are just beginning to slowly evolve over time. However, during this stage the frequency evolution is so slow that it is nearly immeasurable using modern GW detectors. This stage is classified as binaries whose masses can take a large range of values from white dwarf binaries up to stellar mass black hole binaries. Although one should note that the emission frequency is highly dependant upon the masses being considered. During this stage the amplitude of the GW are small, however, provided a long observational period, they are still detectable. Throughout the observational period, the frequency will remain essentially constant with just a slight variation as the systems evolve. Many of these systems would be accessible to LISA.

2.2.3 One Last Breath

The chirping stage of an inspiral is the final stage just before coalescence. This stage can be as brief as a few seconds. The binary systems have completely circularized and the GW amplitudes are increasing significantly with every orbit. The frequencies again are highly dependant upon the masses that make up the binary but can be as low as several mHz and as high as several hundred Hz. Throughout the observational period, the frequency will increase rapidly until the two masses finally merge. Considering the frequency range that

this stage covers, these sources would be available to LIGO.

2.3 Gravitational Wave Detectors

There are two types of gravitational wave detectors that will be discussed throughout the remaining chapters. These two types are Earth based and space based detectors. Each of these detectors have their advantages and disadvantages as well as being sensitive to different stages of an inspiral evolution. At the heart of each type of modern day GW detector is an interferometer that is used to measure the infinitesimal deviations in path length changes.

The basic principle that allows an interferometric observatory to detect GW can be understood by examining the phase difference between two arms of an interferometer as a gravitational wave passes perpendicular to the plane of the interferometer. For the laser light, the metric provides the following interval between the ends of the x-arm of the interferometer in geometrized units:

$$0 = -dx^{0^2} + (1 + h_+)dx^{1^2}, \tag{2.15}$$

where $h_{xx} = -h_{yy} = h_+$. As pointed out in eq. 2.3, the impinging gravitational wave introduces a small perturbation to the flat Minkowski metric. The phase along just the x-arm of an interferometer accumulated from one round trip along that arm can then be expressed as:

$$\Phi_x = \int_0^{\tau_f} 2\pi f dx^0, \tag{2.16}$$

however eq. 2.15 shows that $dx^0 = \sqrt{(1 + h_+)}dx^1$. With this in hand, eq. 2.16 becomes:

$$\Phi_x = 2\pi f \left(\int_0^L \sqrt{(1+h_+)} dx^1 - \int_L^0 \sqrt{(1+h_+)} dx^1 \right) \approx 4\pi f \int_0^L (1 + \frac{h_+}{2}) dx^1 = 4\pi f L (1 + \frac{h_+}{2}), \tag{2.17}$$

where L is the unperturbed length of the interferometer arm and f is the frequency of the laser light. Now for light traveling along the y-arm of the interferometer, the gravitational wave will have the reverse effect as that along the x-arm. If the x-arm is expanding then the y-arm will contract as illustrated in fig. 2.1. Therefore the calculation is very similar just the sign of the metric perturbation is reversed giving $\Phi_y = 4\pi f L(1 - \frac{h_+}{2})$. Now when combined, the phase difference between the x-arm and the y-arm will be:

$$\Delta\Phi = \Phi_x - \Phi_y = 4\pi f L h_+. \tag{2.18}$$

If no impinging gravitational wave is present then the laser light from the x- and y-arms would combine destructively at the antisymmetric port of the interferometer to produce a dark spot on the photodetectors. However when a wave impinges, the phase shift in eq. 2.18 would produce a oscillating bright and dark spot at the photodetector. By carefully monitoring the antisymmetric port of the interferometer, one can measure an impinging gravitational wave.

2.3.1 Laser Interferometer Gravitational Wave Observatory

Although the basics of how an interferometer can be used to identify GW signals has been addressed, each detector has many other issues to contend with to obtain the necessary sensitivities to actually detect a signal. LIGO is one of the Earth based broad band interferometer detectors with a observation window from roughly 40Hz to several thousand Hz. It behaves

just like a traditional Michelson interferometer with a few adjustments. The arm lengths are fixed at 4km for the first Hanford detector (H1) and the Livingston detector (L1) and 2km for the second Hanford detector (H2). The fixed arm lengths allow the LIGO detectors to mitigate noise that arises from fluctuations in the central frequency of the laser source. If not for this fact, any possible signal would be overridden with this noise source, which is several orders of magnitude larger than the signal LIGO is trying to detect. The x and y arms of the LIGO detector make up the largest Fabry-Perot cavities in existence. These cavities are used to increase the effective length of the interferometers arms. By recirculating the laser light though these cavities two hundred times, the impinging gravity wave would cause a resulting phase shift 200 times what is expressed in eq. 2.18. This makes the problem of detecting an impinging wave a little more tractable as the phase difference builds up after each pass.

Laser frequency fluctuations aside, there remain several contributing noise sources that LIGO must first overcome before it can be sensitive to any impinging GW. The two major contributing noise sources that bound the high and low frequency sensitivity curves are shot noise and seismic noise respectively. The noise curves for both LIGO and LISA are illustrated in fig. 2.2. The rise in the curve for LIGO at high frequencies is due to the presence of shot noise which is caused by the uncertainty in the number of photons that define the laser beam. The rise in the noise curve at low frequencies is due to the presence of seismic noise. LIGO is equip with seismic isolation units whose sole purpose is to mitigate the seismic vibrations from various sources such as plate tectonics, construction, incoming and outgoing tides. However, many of these sources can not be completely removed resulting in an increasing noise source at low frequencies that can result in the laser losing alignment with the optics.

Additional software tools have been developed to attempt to counter these effects as best as possible. To date, the software tools have resulted in moving the low frequency cutoff for inspiral searches using LIGO from 100 Hz in S1 to 40 Hz in S5.

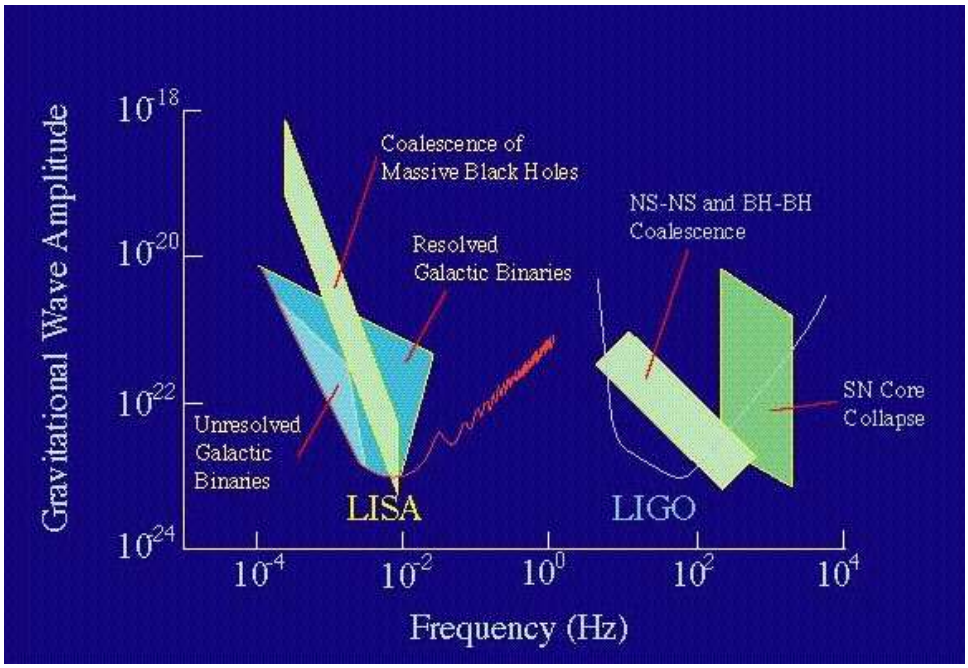

Figure 2.2: This is a plot of the noise curves for both LIGO and LISA. Also illustrated in this figure are the various sources available to both detectors [11].

Unlike traditional optical observatories that focus their aperture towards the direction they are interested in observing, gravitational wave detectors are always looking in all directions simultaneously. The sensitivity any given detector has to a single sky position is determined by slow varying weighting functions that can modulate the signals at the detector's output. These weighting functions are commonly referred to as beam pattern functions or antennae pattern functions [13]. Several Earth based detector beam pattern functions are illustrated in fig. 2.3. What is important to note is that there are several sky positions where one detector may be nearly blind. The angles α and δ refer to the right ascension and declination respectively. Therefore it is possible for a signal to go undetected by a single in-

terferometer but have a very strong signal-to-noise ratio (SNR) in a complementary detector. Another important point is that as the Earth rotates and orbits the sun, these sensitivity plots will vary drastically where the minima in one plot can later become a maxima.

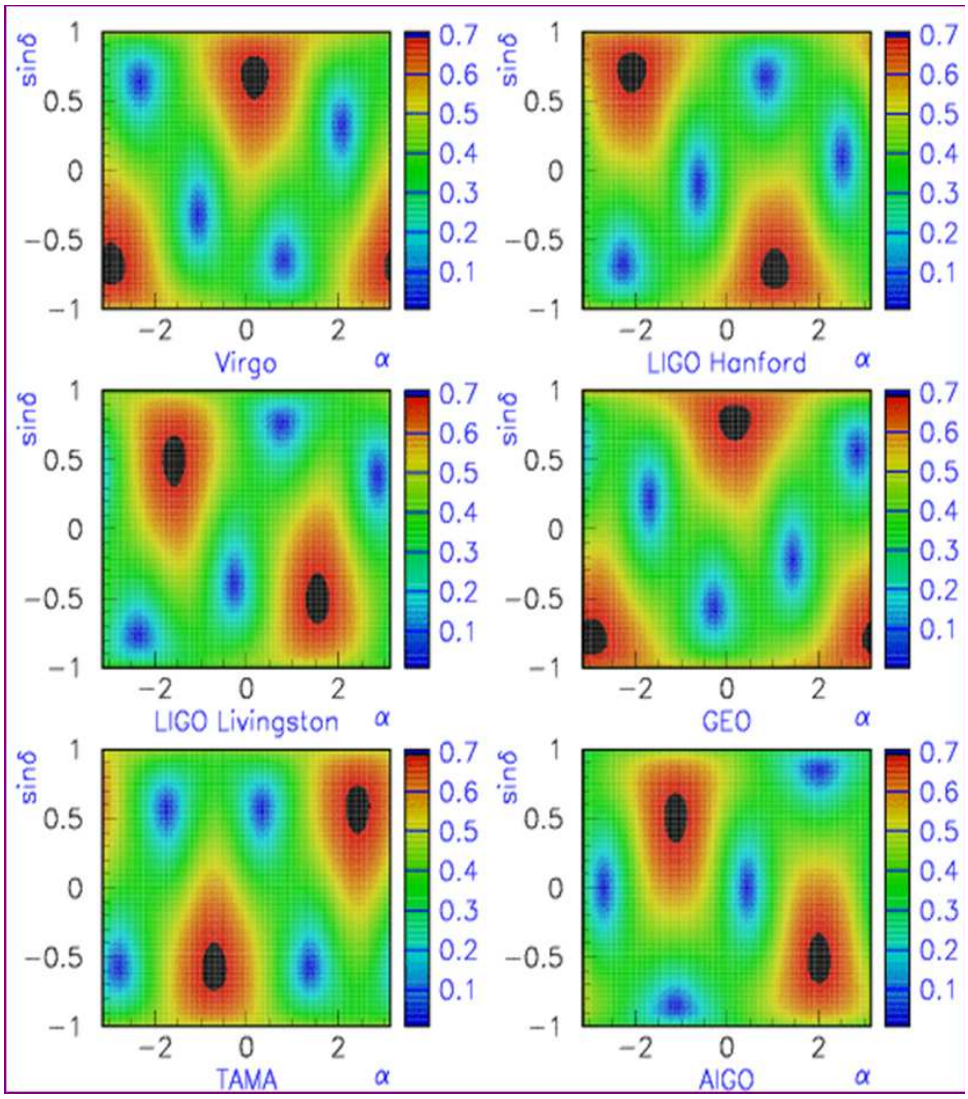

Figure 2.3: This figure shows several beam pattern functions for a variety of Earth based detectors. These are all valid at only a single point in Earth's orbit. The angle α is the right ascension and the angle δ is the declination. [12]

The frequency range that LIGO is sensitive to means that it would be observing the final stage of inspirals, i.e. the chirp stage. Inspiral signals in LIGO's band are on the order of

seconds. This means that the detector orientation with respect to the source is fixed for the duration of the signal and hence no further modulation of the signal will occur. Additionally because these signals are so short lived and the detectors are essentially stationary with respect to the source for the signal duration, a single detector can not triangulate the position of a possible source by itself. The accurate triangulation of a source requires at least two more separate detectors.

2.3.2 Laser Interferometer Space Antenna

LISA is a very different type of interferometric detector. It is a space based version of the ground based interferometers and is sensitive to GW with frequencies ranging from 0.1 mHz up to 1 Hz. LISA is not a traditional 90 degree Michelson interferometer but instead LISA maintains a 60 degree nearly equilateral triangle. This is achieved by flying the three vertices that comprise LISA in three separate orbits around the sun each tilted 60 degrees with respect to the ecliptic and rotated $\pi/3$ with respect to each other. This allows LISA to maintain its orientation without the use of additional thrusters although some microthrusters are used to make fine adjustments when needed. LISA's center will lag the Earth at one of its Lagrange points as it completes one orbit around the sun a year. Due to the flight paths of each craft, the LISA triangle as a whole completes one full retrograde rotation a year as well. The arm lengths of LISA are approximately 5 million km. Again considering that the measurement of a GW is relative, the longer the arms used then the larger displacement the impinging wave will create. Another major departure from your traditional interferometer is the fact that the laser light from one craft is not reflected back from the partner craft.

After the laser light traverses a 5 million km arm, the beam diffraction has reduced the total number of photons that are received at the neighboring craft to such a level that it would be unable to reflect a significant number of photons back to the original craft. Instead the incoming light from any craft is phase locked with another new beam that is returned to the neighboring craft.

A direct results of LISA being a space based interferometer is that it does not suffer from the common low frequency noise that plagues earth based interferometers namely, seismic noise. However, the arm lengths in LISA are not fixed but are allowed to vary as much as 1% which introduces the noise associated with laser frequency fluctuations. Without devising means of mitigating this noise source, LISA would be unable to function effectively as a gravitational wave detector. A strategy called time delay interferometer (TDI) is a means of combining the data obtained from LISA that would effectively remove all noise from laser frequency fluctuations. Much more on the TDI will be discussed later. Once this laser frequency fluctuations are removed from the data, there remain several sources of noise that LISA must still contend with when searching for a signal. The two main sources are shot noise again and proof mass noise that set the limits on LISA's sensitivity at high and low frequencies respectively. Again shot noise is what determines the high frequency sensitivity of LISA. Proof mass noise is the noise associated with the random motions of the proof masses and this dominates the sensitivity of LISA at low frequencies.

Although there are some sources that may merge within the LISA band such as super massive black holes, a large majority of inspiral sources visible to LISA will be in the early stages of inspiral namely, the stationary stage. This means that the signals will be long lasting and visible to LISA for possibly the entire projected mission lifetime.

Whereas the beam pattern functions for Earth based detectors are constant for the inspiral signals for which they would observe, the beam pattern functions for the inspiral signals that would be visible to LISA vary drastically over the observation period. This introduces additional modulations of the data at the photodetectors and these modulations will vary depending upon where the source is located in the sky. This modulation for an originally monochromatic sinusoid can bee seen in fig. 2.4. It the additional complications that arise from the time varying beam pattern functions that provide LISA with the ability to accurately track a source location.

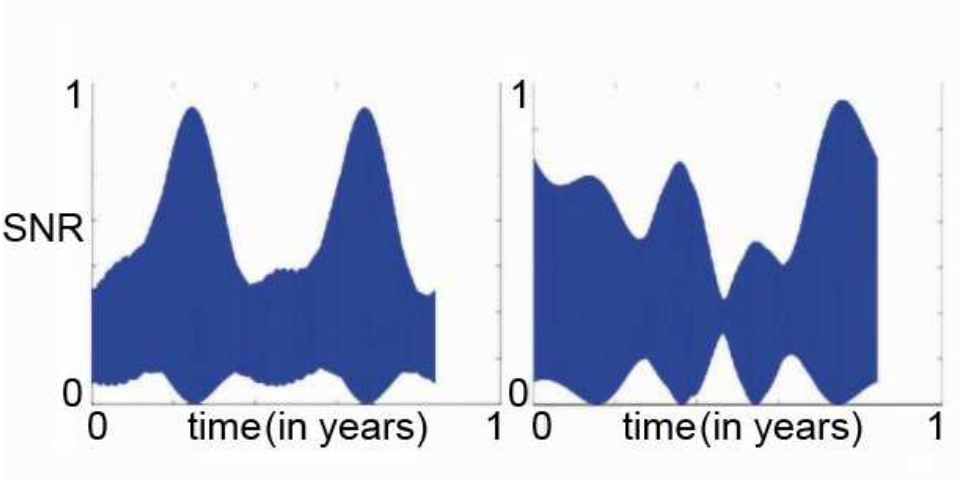

Figure 2.4: This figure shows how the orbital and rotational motions of LISA will modulate a previously monochromatic sinusoid waveform. The values on the vertical axes are normalized to unity. The plot on the left is for a source located within the ecliptic plane whereas the plot on the right is for a source located near either of the poles of the ecliptic coordinate system.

Although much of the complications that arise when using TDI will be relegated for later chapters, the symmetry of these combinations will be addressed here. The natural symmetry of LISA is a $\pi/3$ symmetry arising from a Michelson combination of the LISA data. This is represented in fig. 2.5. What is obvious from the first panel of plots is the $\pi/3$ symmetry. However, other than just mitigating the laser frequency noise, the TDI

combinations also generate a more traditional $\pi/2$ symmetry associated with traditional Michelson interferometers as illustrated in the second panel in fig. 2.5. What should be noted is the normalization scheme used here. The plus polarization for the Michelson combination is normalized to unity. To maintain the relative magnitude difference between the plus and cross polarizations, the cross polarization is normalized to the maximum value obtained in the plus polarization plot. Therefore this plot illustrates that the cross polarization is roughly 1/3 the magnitude of the plus polarization. The TDI combinations in the bottom panel are not normalized at all but do illustrate the same the relative magnitude difference between the plus and cross polarizations.

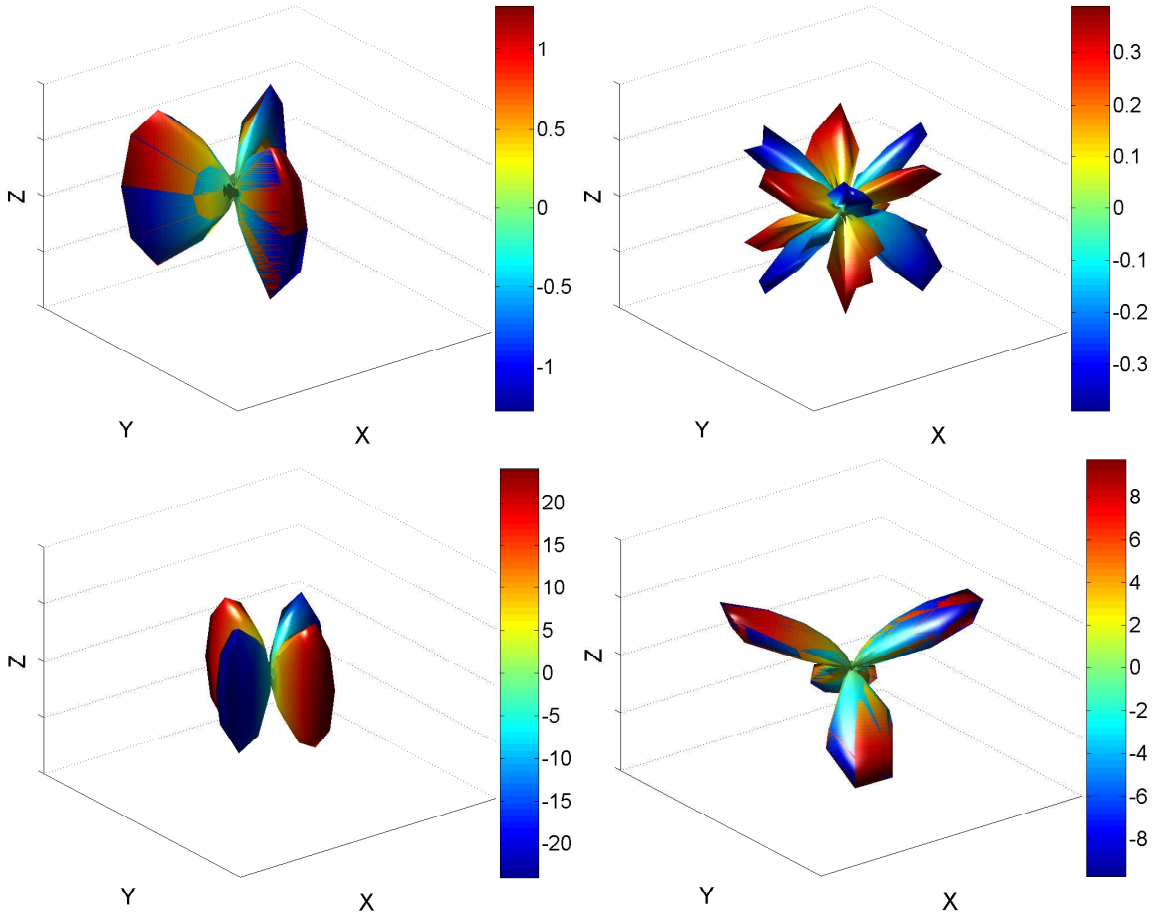

Figure 2.5: These plots illustrate the symmetry of the average sensitivity of the beam pattern functions to all sky positions. The top two plots are the average all sky response of the Michelson combinations to the plus and cross polarizations respectively. The bottom set of plots is the average all sky response of the TDI combinations to the plus and cross polarizations.

Chapter 3

LISA Data Analysis Software Package

3.1 Data Flow

When developing the software tools necessary to simulate and analyze signals with LISA, the first step is to understand the flow of data that will occur. Although this is a rather simple statement, there is a tremendous amount of detail that must be maintained to yield a efficient and portable software analysis package. The flow of data must be such that the overall pipeline completes in a reasonable amount of time, maintains the highest degree of accuracy and is reproducible. For example, the brute force method for this case would be to write the entire modulated waveforms as a function of as many as 12 parameters and then evaluate this at any given region of parameter space that is interesting. This method is the simplest straight forward approach. When utilizing a 30 node beowulf cluster, the computational time required for analyzing just a small sample of the parameter space using the brute force method is on the order of weeks. The actual pipeline developed can achieve better accuracy than the brute force method mentioned above and analyze the same volume

of parameter space in less than a day on a single desktop PC. Once parallelized across a computing cluster, the advantages are obvious.

The pipeline that has been developed has multiple applications. The original motivation for developing this software package was to estimate parameter uncertainties for specific regions of parameter space to ascertain how these uncertainties vary as you traverse the parameter space. As the software developed, the secondary functionality of animating and plotting various features of LISA was incorporated into the software package. This feature can give a better physical understanding of the physics of LISA as well as to present as much data in a closed and concise form as possible for later interpretation. Finally, the latest addition to the software repository was to perform real searches in noisy data using the search statistics developed in chapter 4. This will be very beneficial when LISA comes online and data has begun to accumulate.

The current status of each one of these packages are different. Figure 3.1 illustrates the data flow for all software processes that can occur. The software currently can analyze the parameter uncertainties at any regions of parameter space with little user input. This is all done in the analysis section of the pipeline. The user just needs to specify what region he/she is interested in and the software will automatically produce the appropriate results and properly segregate the resulting data. However, the animation/plotting package is not nearly as intuitive and requires more user input in the form of post processing scripts. In both these cases, the preprocessing is identical. This is not the case for the searches, which require the most preprocessing and post processing by the user. Considering that neither the animation/plotting functionality nor the signal search functionality were never the primary focus of the software, these abilities were never fully completed. What should be noted is

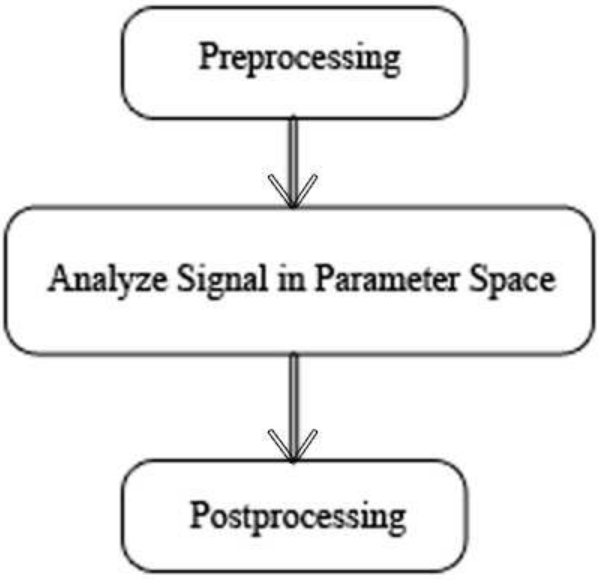

Figure 3.1: This figure illustrates the hierarchy of the data flow for the software. This is not a flow chart for the actual analysis software.

that the general algorithm for these additional functionalities have been established and the remaining tasks leave room for future work and improvements.

The preprocessing section of data flow is where all static variables are assigned. This mainly encompasses the beam pattern functions, the Doppler phase shift and the TDI phase. The beam pattern functions have been explained but the Doppler phase and TDI phase have not. The Doppler phase is the contribution to the phase of any monochromatic signal based upon its relative motion towards or away from a source. The incorporation of TDI results in additional phase terms that will be discussed in a later chapter. This additional phase term is another static variable that is assigned at this stage of the data flow. These three functions are evaluated for all sky positions of interest and roughly every 3 arc seconds of LISA's orbit. This is one of the key features that allows this pipeline to function more efficiently than the brute force method. If one chooses to analyze the signal at the bare minimum discretization that is computationally possible and still able to produce a decent sinusoid

with the brute force method, the result is the sinusoid waveform illustrated in the left plot in fig. 3.2. Remember that the brute force method has to contend with the a balancing act between the calculation costs and the desired resolution that can not be circumvented. On account of the fact that the actual signal phase varies on a much shorter time scale then the beam pattern functions, one can afford to fold in the beam pattern functions slowly over the course of a year. For every 10 minutes the beam pattern functions, Doppler phase and TDI phase are treated as constant while the rest of the phase of the signal is allowed to evolve naturally during this time period. The 10 minute duration is small enough to provide a smooth transition from one value of the beam pattern function, Doppler phase or TDI phase to the next, which is required for the utmost accuracy. This also means that you do not need to calculate the signal phase for the entire year duration but instead only need to calculate it once for a set number of cycles. Whatever the choice for the total number of cycles were, the requirement that they do not span a length of time shorter than the interval at which the static variables span, namely 10 minute, was enforced. For the highest frequency of 0.1 mHz to have a duration that was at minimum 10 minutes, the total number of cycles was determined to be 61. This was the value that was then used for all subsequent frequencies. In doing so, the resolution for the signal phase is increased dramatically as illustrated in the right plot in fig. 3.2. So once the static variables for the beam pattern function, the Doppler phase and TDI phase are created, the calculation of the signal for any point in the parameter space can almost be done on the fly. Something that should be taken away from the plots in fig. 3.2 is even for larger frequencies, the discretization can afford to be very fine. This is something that the brute force method could simply not achieve for every frequency that was to be analyzed. In the past, either the computational time or desired resolution had to

vary with frequency. Previously, the low frequencies could afford to have very course spacing seeing how the phase evolved very slowly but as you increased the frequency so increased the computational time to account for the faster evolving phase. This is no longer an issue considering that the phase is always evaluated for the same number of cycles in advance regardless of the frequency. So the total number of cycles that are evaluated is identical for all frequencies and therefore so is the total computational time required to complete a study regardless of the frequency. This however does introduce the added complication whereby the total time or segment length that is spanned by each frequency now varies. This requires appropriately incorporating the beam pattern functions to compensate for the varied lengths of the segments.

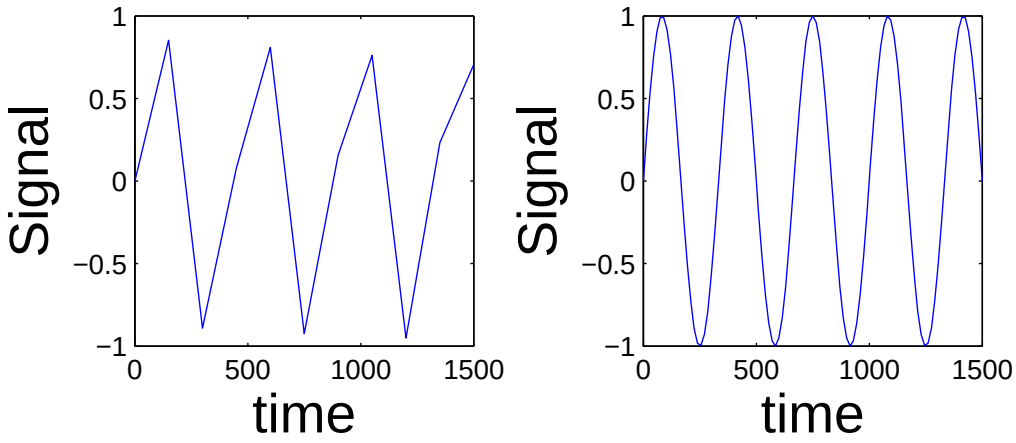

Figure 3.2: The plot on the left is the minimum discretization that can be allowed with a calculation time on the order of weeks for a 30 node beowulf cluster. The plot on the right is a sample of how discreetly the new method allows with the calculation finishing in under a day for a single desktop PC.

An additional complication that had not originally been anticipated came when trying to incorporate eccentric waveforms. The original application used the same discretization for all frequencies which allowed the pipeline to obtain the resolution illustrated in fig. 3.2. However

when considering eccentric waveforms, this discretization again would have to vary depending on the degree of eccentricity. Figure 3.3 illustrates a single cycle for both the plus and cross polarizations for varying values of eccentricity. The top and bottom panels in fig. 3.3 are the plus and cross polarizations respectively. In these plots, the eccentricity increases from left to right with the values $e = 0$, $e = 0.3$ and $e = 0.6$. As is evident in fig. 3.3, the discretization can not be constant throughout the cycle if one is to accurately characterize the features of the eccentric waveform. Additionally, the discretization would have to be a function of the eccentricity parameter as well. These facts once again lead to exhausting the computational resources. A new method had to be specifically designed to combat this particular case that would also leave the current pipeline for the Newtonian waveforms in tact. Considering that the eccentric waveforms are by definition a superposition of monochromatic waveforms, the most natural method was to just break any eccentric waveform up into its individual harmonics. Each harmonic could use the same discretization scheme already developed and then the proper weighting of the individual harmonics would have to follow. Once this was achieved, the eccentric waveforms would have the desired resolution and the computational time in computing these waveforms would be reasonable. This technique proved to be the most efficient and natural way to approach this issue and the end result could obtain SNR values that are as accurate as those that would be obtained from the plots presented in fig. 3.3.

The analysis section of the pipeline is the heart of the software package. This section allows one to analyze any type of monochromatic signal or even slightly chirping signal where the frequency slowly increases over time. The following chapter is dedicated to the theory of signal analysis so for now all that needs to be addressed is how this stage of the pipeline

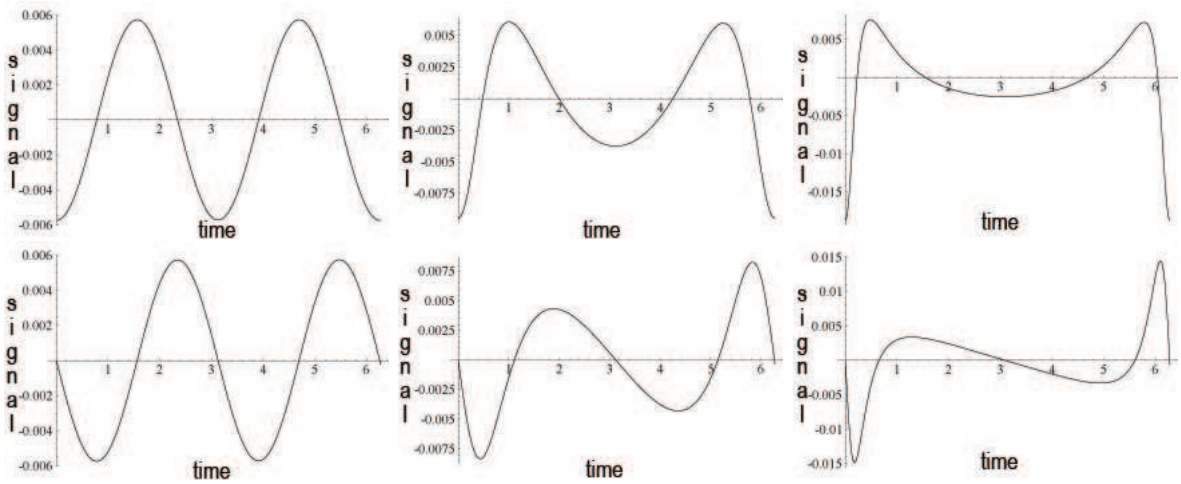

Figure 3.3: The top three plots are for the plus polarization and the bottom three are for the cross polarization. In both sets of three, the eccentricity value increases from left to right with the values $e = 0$, $e = 0.3$ and $e = 0.6$.

functions and the details of signal analysis will be relegated for future chapters. Using the static variables created during the preprocessing section of the data flow, the analysis section of code will calculate the SNR as well as any number of other quantities related to the signal that may be of interest. This stage is ideal for animating how the SNR behaves in any region of parameter space. The routines provided allow one to view the animations as a function of any number of other parameters. For example, using the function EvalSNR.m one can animate the sky position dependance of the SNR as you increase the frequency or as a function of time. The animations serve as a very useful tool in identifying the physical behavior of LISA with respect to various types of sources. Many animations have already been created and are just starting to be cataloged and will soon be available to the public on the following web site: *http* : *//gravity.physics.wsu.edu/*. This stage also provides the means of calculating the variance-covariance matrix in any region of parameter space using the function EvalInfoMatrix.m. The importance of the variance-covariance matrix is something that will be discussed at some length in a later chapter. The last addition also

provided the means to perform matched filtering which is an algorithm for searching for signals embedded in noisy data. A more detailed discussion of what a matched filter is will also be handled in a later chapter.

The post processing section is where one interprets and sifts through the vast amount of data that is generated in the analysis section of the data flow. This stage is very open ended with no real structure considering that the interpretations are the driving force behind this section. Therefore, if one desires to examine how the errors associated with the frequency parameter vary as a function of sky position then one simply reads in the appropriate files generated in the analysis section and combines them in the proper fashion. Similarly for the animations and the searches. In the end, this section is determined purely by what the users intentions were at the onset of the start of the data flow pipeline. The backbones of this section will remain the same and are currently in place but the details of the output will vary from analysis to analysis and hence the existing functions will have to be modified accordingly.

3.2 Analysis Software

Although the preprocessing and postprocessing sections of the data flow are important, they are simple enough that they do not require further detailed descriptions. All the beam pattern functions, Doppler phase and TDI phase values have already been calculated for all possible values they can take and therefore there is no need to repeat this calculation for any future run of the analysis pipeline depicted in fig. 3.4. As already mentioned, there basic structure of the postprocessing section of the data flow is in place but the desired output is

what real shapes this section and that will vary from run to run of the pipeline. So this is why the pre and post processing sections can remain some what opaque for this discussion.

The code that runs a given analysis is one of many types depending on what output the user desires. All of the main codes are named with Eval as a prefix. For example, to calculate the parameter uncertainties, the code to run would be EvalInfoMatrix.m. This will call many other helper functions that I will discuss below. There are similar codes that are used for just evaluating the SNR or evaluating a template mismatch that are also provided. The general behavior of each Eval*.m code is the same other than the output produced. They all utilize the same generalized routines, have the same data management, and have the same organizational schemes.

The pipeline for the analysis section makes up roughly 80% of the analysis software. This stage allows users to define many different classes of signals. This stage also provides the means to perform simple searches or determine the parameter uncertainties in any number of the 12 dimensional parameter space. The first step of the pipeline is where the user defines the dynamic variables for the current run, i.e. frequency, inclination, declination, right ascension, masses etc. This is done in one of two places, either at the command line when running the function or in a configuration file called configureFile.m. The second method is more convenient if the user is going to continually focus on a given region of parameter space since in this case some of these dynamic variables will remain fixed from run to run. There is also the combination option where the user chooses some parameters to be defined at the command line and other to be defined within the configuration file. The last method is the most common usage. For example, this method allows the user to examine the frequency dependance or sky dependance of parameter errors while keeping the source orientation and

masses the same from run to run.

Once the dynamic variables have been set, the code then determines which type of wave form to use: Newtonian or Post-Newtonian (PN). The Newtonian waveforms are accurate for circular orbits which will apply to many source that will be available to LISA. The PN waveforms apply corrections to the Newtonian waveforms to properly account for additional complications such as the periastron advances of eccentric sources that would be available to LISA [15]. Although the PN waveforms reduce to the Newtonian waveforms in the proper limits, the Newtonian waveforms are more desirable when dealing with this limiting case due to the simplicity of the waveforms, which results in noticeably less computational time for the analysis.

After the desired waveform has been selected, the pipeline then loads the beam pattern functions for the entire observation period. This is done using getBeamPatternFuncs.m or getSNRBeamPatternFuncs.m. The main difference between these two functions is that the later of the two is an abbreviated version of the former. The getSNRBeamPatternFuncs.m function does not need to load any of the derivative functions just the basic beam pattern functions. This would be used for a straight up search. However, in order to calculate the parameter uncertainties, all the derivatives of the beam pattern functions are required as well. The process of loading in all the derivatives of the beam pattern functions for the entire observational period takes substantially longer and requires significantly more memory than just loading the beam pattern functions themselves. What should be noted is that there are two time scales that come into play at this stage. The first is the short step time scale, which is the time steps for the monochromatic phase. This time scale is the duration that the 61 total cycles mentioned previously span, which will be different at different frequencies. The

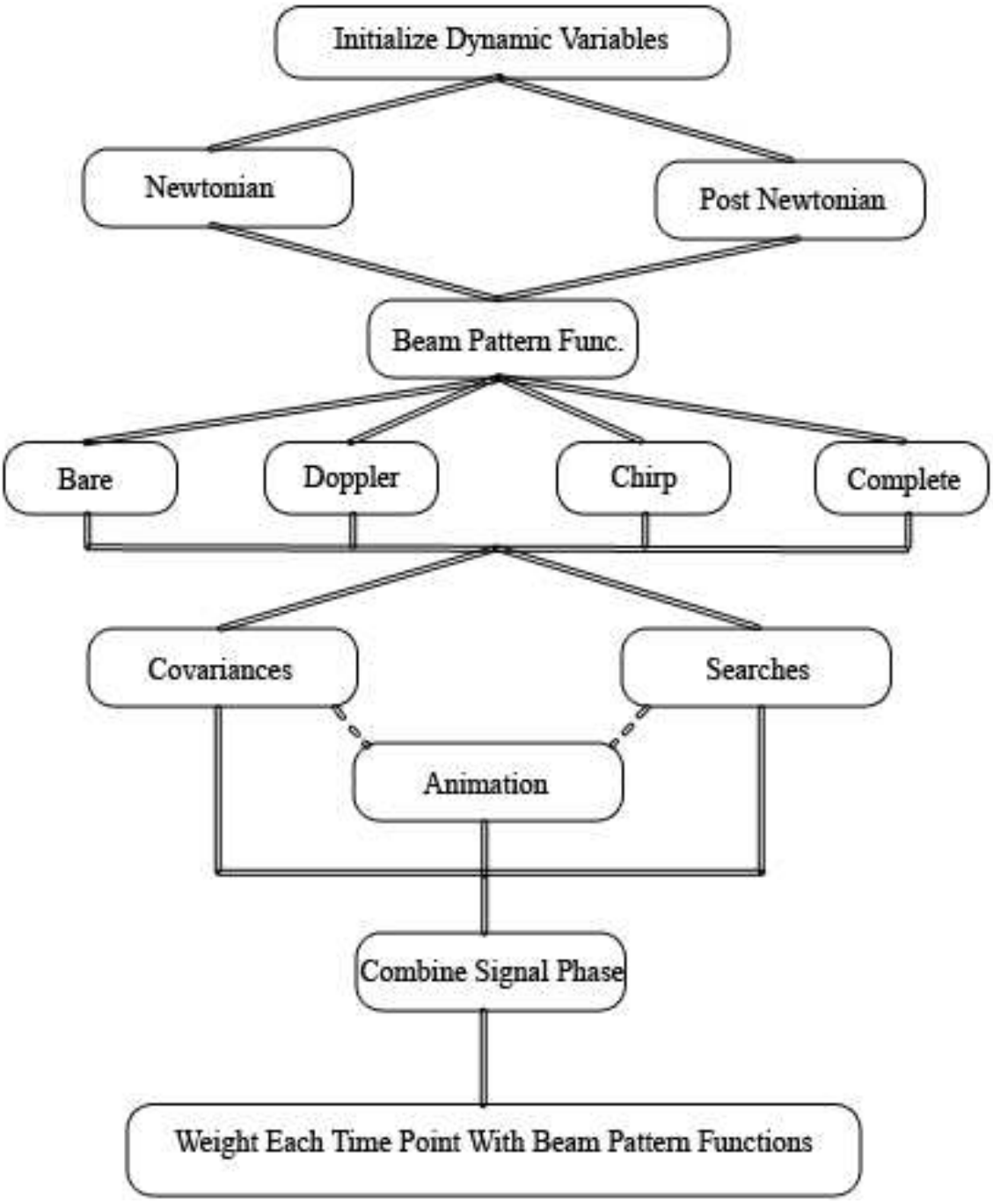

Figure 3.4: This is a flow chart of the analysis pipeline. The pipeline flows from top to bottom.

second time step is the long time step, which is the time step between successive points in the beam pattern functions. To get a handle on how slowly these beam pattern functions and their derivatives vary for a one year observation period, the beam pattern function for just a single arm of LISA is plotted in fig. 3.5. This should be compared with the actual signal that has hundreds of thousands of oscillations in the same observation period as illustrated in fig. 2.4. Figure 3.5 is a plot of the actual discretization used in the analysis pipeline. As is evident in the plot, the discretization was chosen such that the variations were smooth from one point in the orbit to the next.

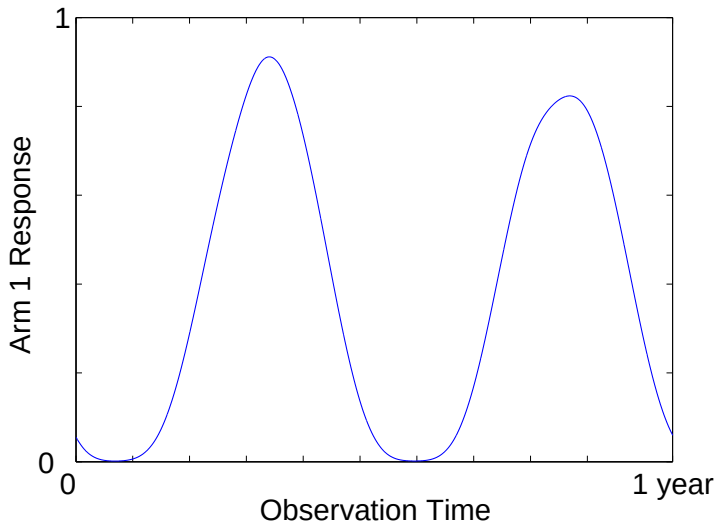

Figure 3.5: This is a plot of the beam pattern function for arm 1 during a 1 year observation period for a source located within the elliptic plane.

Once the beam pattern functions have been loaded, the pipeline is then equip to handle one of four possible cases: bare, Doppler, chirp, and complete. This option is determined by a set of flags. The bare case considers a non-physical signal that does not have any Doppler frequency shifting and assumes a stationary frequency for the entire observation period. The Doppler case is the physical signal with Doppler shifting incorporated but still assumes a

stationary frequency. The chirp case is again non-physical case where Doppler shifting is not incorporated but the frequency is allowed to evolve slowly over the course of the observation period. The final case is the complete case where the Doppler shifting is incorporated and the frequency is allowed to evolve over the course of the observation period. As will be discussed in a later chapter, all the non-physical cases are used to furnish a better understanding of how the modulations that are introduced from each part of a signal's phase contribute to the signal as a whole.

Once all the parameters have been set, the beam pattern functions loaded and the particular case has been selected, there are now two avenues to take. The first is to analyze the parameter uncertainties and the second is to do an actual search. Both of these options allow for the possibility to generate animations. This is why there is the dashed line to that stage of the pipeline. The animation stage is not a necessary stage so the user can turn this stage off and on at will.

The last two stages of the pipeline are in some sense a single step. This amounts to getting the proper phase at each time point as well as weighting each time point by the proper beam pattern weighting coefficient. When all is said and done the overall SNR can be written as a double summation as follows:

$$SNR = \sqrt{\sum_{t_l=0}^{1year} \left(W_{t_l} \sum_{t_s=0}^{long\,time\,step} \sin(\Phi_{t_l} + \Phi_{t_s}) \right) \Delta t_s}, \tag{3.1}$$

where t_l indicates the interval between terms is the long time step, t_s indicates the interval is now the short time step and $\Phi_{t_l} + \Phi_{t_s}$ is illustrated in eq. 3.2 below as just Φ. Regardless of what type of analysis is performed, the phase recombination is identical. During this

stage, all the phase contributions must be tracked. This amounts to properly adding the monochromatic part of the phase to the remaining parts of the phase. Equation 3.2 illustrates the entire phase for the complete signal.

$$\Phi = 2\pi ft + \phi_D + \phi_{TDI} + \phi_{chirp}, \tag{3.2}$$

where ϕ_D is the Doppler phase and ϕ_{TDI} is the TDI phase both of which are calculated in advance. The monochromatic ($2\pi ft$) and chirp (ϕ_{chirp}) part of the phase are the only pieces that vary in the short time steps while the remainder is held constant until the short time steps sum up to the long time step. This method requires precise tracking of the signal phase in order that the remaining phase terms are consistent and accurate. Aliasing effects must also be avoided when combining one long time step with the next consecutive long time step. Once this is done, the signal is complete and interpretation of the results can follow.

Chapter 4

Detecting Signals with LISA

The Laser Interferometric Space Antenna is being designed as a space-based detector to observe low-frequency GWs to complement the high-frequency observation of its Earth-based counterparts. Many of the sources of low-frequency GWs fall in the category of compact binary objects such as neutron star binaries or white dwarf binaries. During the early stages of the inspiral, these compact binaries will produce essentially monochromatic low-frequency gravitational waves, which will be potential sources for LISA.

The first section will begin by enunciating the three noise-independent data combinations, or "pseudo-detectors", that were first obtained in Ref. [16] by combining the frequency shifts of the six laser beams exchanged among the LISA spacecrafts through time-delay interferometry [17]. The following section will then study the antenna patterns of these pseudo-detectors at different points in LISA's orbit, emphasizing how their relative sensitivities to a mildly chirping source vary as a function of sky position and source frequency. The studies bear out the fact that noise-independence of detectors is a property distinct from their geometric independence. Indeed, at GW wavelengths larger than about 0.1 AU, which will be termed

as the long-wavelength limit, the strain of the third pseudo-detector tends to the difference of the strain of the first two.

The optimal statistic for detecting gravitational waves from compact binary inspirals by coherently combining the data of the three pseudo-detectors will then be addressed for both the Newtonian waveforms as well as Post-Newtonian.

The statistic obtained in these calculations tracks the Doppler modulation of the signal phase induced by the motion and time-varying orientation of LISA with respect to a given source, and allows for a slightly "chirping" source [18]. Additionally, an estimate of the number of templates required to institute a search using the statistic developed here follows.

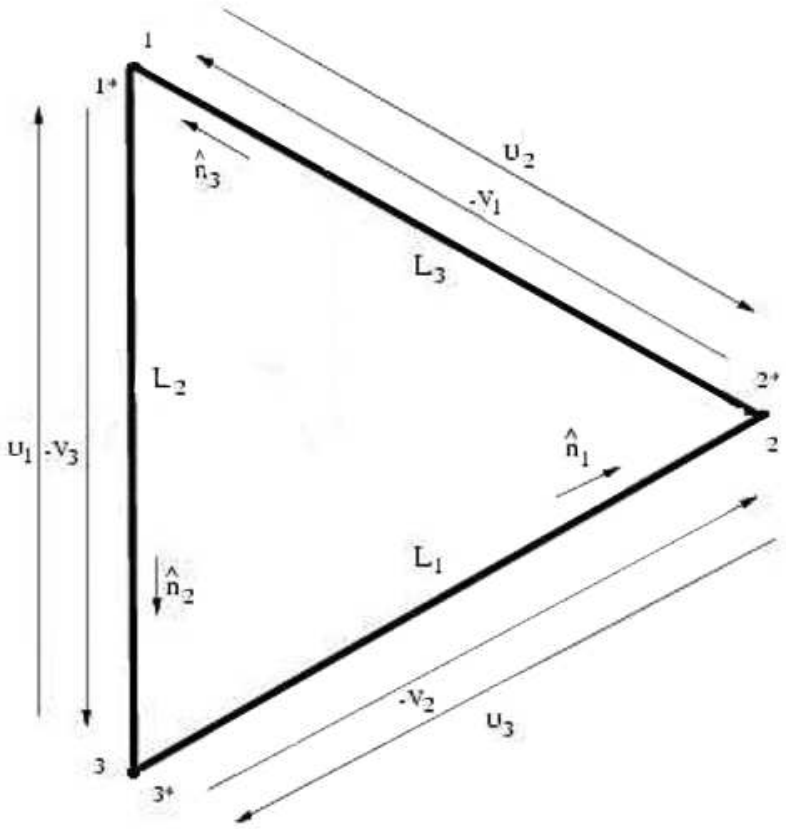

Figure 4.1: LISA consists of 3 spacecrafts located at the vertices of an equilateral triangle. These craft exchange six elementary data streams, labeled U_i and $-V_i$. The U_i beams propagate clockwise, whereas the $-V_i$ propagate counterclockwise.

4.1 The pseudo-detectors

As illustrated in Fig. 4.1, LISA consists of three spacecrafts, labeled 1, 2, and 3, located clockwise at the correspondingly labeled vertices of an almost equilateral triangle. Let the arm-lengths of this triangle be L_1, L_2, and L_3, such that L_i is the length of the arm facing the vertex i. For specifying the orientation of each arm, we assign unit vectors $\hat{\mathbf{n}}_i$ along them, such that their directions are oriented anticlockwise about the triangle. Each spacecraft will have two optical benches (denoted as i and i^* in Fig. 4.1) equipped with independent lasers, beam-splitters and photodetectors. Thus, each spacecraft will shoot two beams towards the other two spacecrafts, respectively, resulting in six one-way beams along the 3 arms.

The effect of an impinging GW on these beams is to cause a shift in the frequency of the laser beam. If ν_0 is the central frequency of all the lasers in LISA, then the fractional shift caused in the beam originating at spacecraft i is

$$C_i(t) \equiv \frac{\Delta\nu_i(t)}{\nu_0} \quad . \tag{4.1}$$

Similarly for the beam from craft i^*. However, what is measured is the frequency fluctuation in the beam from i relative to that originating at $i^* \pm 1$ for the $-V_i$ and U_i data streams respectively. [1] For instance, as shown in Fig. 4.1, $U^1(t) := C_3(t - L_2) - C_1(t)$, is the data stream that is measured by beating the beam transmitted by craft 3 against that of craft 1, measured at time t at craft 1. If a data stream $x(t)$ is acted on by the time-shift operator ζ_i, the result of time-shifting the data is $\zeta_i x(t) = x(t - L_i)$. The label i denotes the arm along which the time-shift is affected. Thus, the time-shift operators are given by,

[1] Note that i, or $i \pm 1$ can take only 1, 2, and 3 as values. Thus, when $i = 3$, one must really take $i + 1$ as $(i + 1)\%3$ which is just 1. Similarly, when $i = 1$, we take $i - 1$ as 3.

$$\zeta_i = e^{i\Omega_i L_i} \,. \tag{4.2}$$

One can thus define the 6 inter-craft steams as follows[20]

$$\begin{aligned} U^1 &= \zeta_2 C_3 - C_1 \,, \quad U^2 = \zeta_3 C_1 - C_2 \,, \quad U^3 = \zeta_1 C_2 - C_3 \\ V^1 &= C_1 - \zeta_3 C_2 \,, \quad V^2 = C_2 - \zeta_1 C_3 \,, \quad V^3 = C_3 - \zeta_2 C_1 \,. \end{aligned} \tag{4.3}$$

Note that a delay of $\sum_{i=1}^{3} \alpha_i L_i$ is effected by the operator $\prod_{i=1}^{3} \zeta_i^{\alpha_i}$.

These shifts, however, are expected to suffer from several noise sources, two of which, namely, laser-frequency fluctuation and optical-bench motion, tower over others. Let the random velocities of the optical benches be $\mathbf{v}_i$ and $\mathbf{v}_{i^*}$, and the frequency shifts suffered by the laser in the optical fibers connecting the optical benches in craft i be η_i. Then the intra-craft beams originating at crafts 1 and 1^* are [20]:

$$\begin{aligned} y_1 &= C_1 - C_{1^*} + \eta_1 - 2\hat{\mathbf{n}}_3 \cdot \mathbf{v}_1 \\ y_{1^*} &= C_{1^*} - C_1 + \eta_1 + 2\hat{\mathbf{n}}_2 \cdot \mathbf{v}_{1^*} \,. \end{aligned} \tag{4.4}$$

Also, the intra-craft beams associated with these crafts get modified to:

$$\begin{aligned} U^1 &= \zeta_2 (C_3 - \hat{\mathbf{n}}_2 \cdot \mathbf{v}_3) - (\hat{\mathbf{n}}_2 \cdot \mathbf{v}_{1^*} + C_{1^*}) \quad , \\ V^1 &= -\zeta_3 (C_{2^*} + \hat{\mathbf{n}}_3 \cdot \mathbf{v}_{2^*}) + (C_1 - \hat{\mathbf{n}}_3 \cdot \mathbf{v}_1) \,. \end{aligned} \tag{4.5}$$

Following the work of Tinto and Armstrong [17], it was shown by Dhurandhar et al. that by acting on the 6 inter-craft streams, U_i, V_i, and the 3 intra-craft streams, $W_i := (y_i - y_{i^*})/2$, with certain polynomials of time-delay operators, $p_i^{(A)}$, $q_i^{(A)}$, and $r_i^{(A)}$, one can form pseudo-detectors,

$$x^A(t) = \sum_{i=1}^{3} \left[p_i^{(A)} V^i(t) + q_i^{(A)} U^i(t) + r_i^{(A)} W^i(t) \right] \quad , \tag{4.6}$$

that have the laser-frequency noise eliminated. Above, A is the pseudo-detector index. Thus, the polynomials $p_i^{(A)}$, $q_i^{(A)}$, and $r_i^{(A)}$ form a representation of the $x^A(t)$.

Of the several possible pseudo-detectors, only 3 are independent [16, 59]. The three that will be discussed here are given in terms of the ordered set,

$$\{p_1^{(A)}, p_2^{(A)}, p_3^{(A)}; q_1^{(A)}, q_2^{(A)}, q_3^{(A)}; r_1^{(A)}, r_2^{(A)}, r_3^{(A)}\}, \tag{4.7}$$

as follows:

$$\begin{aligned} x^1 &= \{1-\zeta, 1+2\zeta, -2-\zeta; 1+2\zeta, 1-\zeta, -2-\zeta; \\ &\quad \zeta^2-1, \zeta^2-1, 2(1-\zeta^2)\}, \\ x^2 &= \{-\zeta-1, 1, \zeta; -1, 1+\zeta, -\zeta; 1-\zeta^2, -1+\zeta^2, 0\}, \\ x^3 &= \{1, 1, 1; 1, 1, 1; -1-\zeta, -1-\zeta, -1-\zeta\}\,. \end{aligned} \tag{4.8}$$

In the above expressions, it is assumed that all arm lengths are almost identical. Therefore, $\zeta_1 \simeq \zeta_2 \simeq \zeta_3 \equiv \zeta$. It is also important to note that these data combinations diagonalize the noise covariance matrix [22]. Although the laser-frequency noise is eliminated in the $x^A(t)$, there is still noise associated with the acceleration of the proof mass used onboard each craft along with photon shot noise. The raw shot noise is characterized by the noise power-spectral density $P_{\rm shot} = 1.8 \times 10^{-37}[f/1{\rm Hz}]^2{\rm Hz}^{-1}$ and the raw noise associated with the on board proof mass is characterized by $P_{\rm proof} = 2.5 \times 10^{-48}[f/1{\rm Hz}]^{-2}{\rm Hz}^{-1}$ as outlined in Ref.[37]. The proof mass noise enters in the very low frequency band of LISA and the shot noise enters the higher end of LISA's sensitivity band. However, these raw noise sources will be modulated differently for the pseudo-detectors in Eq. (4.8). The resulting noise spectra

for each pseudo-detector is [19]:

$$\begin{aligned} P_{x^1}(f) &= P_{x^2}(f) = 32\sin^2(\pi fL)\sin^2(3\pi fL)([6+4\cos(2\pi fL) \\ &+ 2\cos(4\pi fL)]P_{\rm proof} + [2+\cos(2\pi fL)]\,P_{\rm shot}) \quad , \\ P_{x^3}(f) &= 8\left[1+2\cos(2\pi fL)\right]^2\sin^2(3\pi fL)\left[4\sin^2(\pi fL)P_{\rm proof}+P_{\rm shot}\right] . \end{aligned} \tag{4.9}$$

Therefore, the data analysis challenge is to detect signals in this remaining noise.

4.2 Newtonian Waveforms

The energy lost through gravitational radiation will eventually circularize many eccentric sources that are potential candidates for LISA. For this reason, Newtonian waveforms have been implemented as first step approach to the data analysis challenge. These waveforms can be modified appropriately to account for radiation reaction and other PN effects while maintaining significantly accurate waveforms. Before examining how eccentricity will effect the detection statistic, the simpler circular orbit case is examined in depth. Using the knowledge gained from the simplified model, the modifications for eccentric waveforms can be obtained straightforwardly.

4.2.1 The Signal

A gravitational wave propagating in the $\hat{\mathbf{w}}$ direction away from the source will create a perturbation at spacetime location $(t, \mathbf{r})$ given by

$$h_{kl}(t,\mathbf{r}) = h_+(t-\hat{\mathbf{w}}\cdot\mathbf{r})(\theta_k\theta_l - \phi_k\phi_l) + h_\times(t-\hat{\mathbf{w}}\cdot\mathbf{r})(\theta_k\phi_k + \theta_l\phi_l) \tag{4.10}$$

where $h_+(t)$ and $h_\times(t)$ are the two GW polarizations. The sky position $\{\theta, \phi\}$ defines the

Cartesian components of the propagation direction, i.e., $\hat{\mathbf{w}} = (\sin\theta\cos\phi, \sin\theta\sin\phi, \cos\theta)$. Also, θ_k and ϕ_k define the plane transverse to $\hat{\mathbf{w}}$:

$$\hat{\boldsymbol{\theta}} := \frac{\partial\hat{\mathbf{w}}}{\partial\theta} \quad , \quad \hat{\boldsymbol{\phi}} := \frac{1}{\sin\theta}\frac{\partial\hat{\mathbf{w}}}{\partial\phi} \, . \tag{4.11}$$

In the time domain, the strain induced along the ith arm is

$$h_i(t) = h_{kl}(t) n_i^k n_i^l = h_+(t)\xi_{i+}(w_1, w_2) + h_\times(t)\xi_{i\times}(w_1, w_2) \quad , \tag{4.12}$$

where we used Einstein's summation convention over the repeated indices k and l. Above,

$$\xi_{i+} = (\hat{\boldsymbol{\theta}}\cdot\hat{\mathbf{n}}_i)^2 - (\hat{\boldsymbol{\phi}}\cdot\hat{\mathbf{n}}_i)^2 \quad , \quad \xi_{i\times} = 2(\hat{\boldsymbol{\theta}}\cdot\hat{\mathbf{n}}_i)(\hat{\boldsymbol{\phi}}\cdot\hat{\mathbf{n}}_i) \tag{4.13}$$

are the beam-pattern functions of the ith arm for the two polarizations.

An impinging GW causes a change in the light-travel time along an arm that can be calculated by solving the null geodesic equation in the corresponding perturbed spacetime. This in turn causes a time-varying Doppler shift, which clearly depends on the difference in the GW strains at the two crafts at the end of the arm. One also expects this shift to be dependent on the position of the source relative to the arm, $\hat{\mathbf{w}}\cdot\hat{\mathbf{n}}_i$. The fractional frequency shift associated with data stream V_i is given by [20]

$$\frac{\delta\nu_i(t)}{\nu_0} = \frac{-1}{2(1-\hat{\mathbf{w}}\cdot\hat{\mathbf{n}}_i)}\left[h(t-\hat{\mathbf{w}}\cdot\mathbf{r}_{i+1}) - h(t-\hat{\mathbf{w}}\cdot\mathbf{r}_{i-1}-L)\right] \tag{4.14}$$

where $\mathbf{r}_i$ is the position vector of the ith craft in the LISA frame. The speed of light is set to unity.

Next would be to consider the effect of a signal from a compact binary on $\delta\nu_i(t)/\nu_0$. The two polarization amplitudes for the ith arm are

$$h_{i+}(t) = H(\Omega_0)\left[\frac{1+\cos^2\iota}{2}\cos 2\psi\cos(\Phi_i(t)+\delta_c) + \cos\iota\sin 2\psi\sin(\Phi_i(t)+\delta_c)\right] \quad (4.15)$$

$$h_{i\times}(t) = H(\Omega_0)\left[-\frac{1+\cos^2\iota}{2}\sin 2\psi\cos(\Phi_i(t)+\delta_c) + \cos\iota\cos 2\psi\sin(\Phi_i(t)+\delta_c)\right] \quad (4.16)$$

where $\Phi_i(t)$ is the phase received at that arm, $\{\psi, \iota\}$ are the polarization and inclination angles of the binary source and δ_c is the initial phase at the origin of the LISA frame. For a nearly monochromatic signal $\Phi_i(t) = \Omega_0(t - L_i\tau_i) + \phi_D$ where

$$\phi_D(t) = \Omega_0 d_\odot \sin\theta\cos\left(\frac{2\pi t}{P} - \phi\right) \quad and \quad \tau_i := \frac{1}{2}\left(1 - \frac{\hat{\mathbf{w}}\cdot\hat{\mathbf{r}}_i}{\sqrt{3}}\right) \quad (4.17)$$

with $d_\odot = 1AU$ and P=1 year. The last two terms in $\Phi_i(t)$ above are attributed to the relative motion of LISA with respect to a given source. Above, $H(\Omega_0)$ is the signal amplitude at LISA defined as:

$$H(\Omega_0) = 1.188\times 10^{-22}\left[\frac{\mathcal{M}}{1000\ M_\odot}\right]^{5/3}\left[\frac{R}{1\text{Gpc}}\right]^{-1}\left[\frac{\Omega_0}{2\pi\ 1\text{mHz}}\right]^{2/3} \quad (4.18)$$

where $\mathcal{M}$ is the chirp-mass and R is the distance to the source. By using Eqs. (4.12) and (4.15) in the frequency-shift expression Eq. (4.14), and taking the Fourier transform of the result gives

$$\begin{aligned}\frac{\delta\tilde{\nu}_i(\omega)}{\nu_0} &= H(\Omega_0)T\Big[\text{sinc}\left((\omega-\Omega_0)\,T\right)e^{-i\delta_c}\left(l_+^*(\psi,\iota)F^*_{V_{i+1};+}(\Omega_0) + l_\times^*(\psi,\iota)F^*_{V_{i+1};\times}(\Omega_0)\right)\\ &+ \text{sinc}\left((\omega+\Omega_0)\,T\right)e^{i\delta_c}\left(l_+(\psi,\iota)F_{V_{i+1};+}(\Omega_0) + l_\times(\psi,\iota)F_{V_{i+1};\times}(\Omega_0)\right)\Big]\ , \end{aligned} \quad (4.19)$$

where ω is the angular frequency variable. The angles $\{\psi, \iota\}$ have been separated out in the factors $l_{+,\times}$, which are defined in terms of the Gel'fand functions [24] as follows:

$$
\begin{aligned}
l_\times &= -i\left(T_2^2(\psi,\iota,0) - T_2^{-2}(\psi,\iota,0)\right) \quad , \\
l_+ &= \left(T_2^2(\psi,\iota,0) + T_2^{-2}(\psi,\iota,0)\right) \, .
\end{aligned} \tag{4.20}
$$

On the other hand, the orientation of the ith arm resides in the functions,

$$
\begin{aligned}
F_{V_{i+1};+,\times} &= -ib_i\,\xi_{i;+,\times}\,\mathrm{sinc}\left(\Omega_0 L_i k_i^-\right) e^{i\tau_i\Omega_i L_i} \\
F_{U_{i+1};+,\times} &= ib_i\,\xi_{i;+,\times}\,\mathrm{sinc}\left(\Omega_0 L_i k_i^+\right) e^{i\tau_i\Omega_0 L_i} \quad ,
\end{aligned} \tag{4.21}
$$

where

$$
b_i := \frac{\Omega_0 L_i}{2} \quad and \quad k_i^\pm = \frac{(1 \pm \hat{\mathbf{w}}\cdot\hat{\mathbf{n}}_i)}{2} \quad , \tag{4.22}
$$

are both real quantities. The $F_{U_i;+,\times}$ determine the fractional frequency shift in the U_i data stream.

The GW strain contributing to the data combinations, x^A, can now be found by using the fractional frequency-shift expression (4.19) in Eq. (4.6). In the Fourier domain, the strains are:

$$
\begin{aligned}
\tilde{h}^A(\omega) = iH(\Omega_0)T\sum_i^3 \Big[\quad & e^{-i(\delta_c+\sigma_i^A)}\mathrm{sinc}\left((\omega-\Omega_0)\,T\right)\; T_2^{\rho *}\; D_{\rho i}^{A*} e^{-i\tau_i\Omega_0 L_i} \\
& + e^{i(\delta_c+\sigma_i^A)}\mathrm{sinc}\left((\omega+\Omega_0)\,T\right) T_2^{\rho}\; D_{\rho i}^{A} e^{i\tau_i\Omega_0 L_i} \Big]
\end{aligned} \tag{4.23}
$$

where there is an implicit sum over $\rho = \pm 2$. Also, we define

$$
D_{\pm 2\,j}^A := \pi b_j |M_j^A| \, \left(\xi_{j_+} \mp i\xi_{j_\times}\right) \quad , \tag{4.24}
$$

where

$$M_i^A := q_{i-1}^A \mathrm{sinc}\left(\Omega_0 L_i k_i^+\right) - p_{i+1}^A \mathrm{sinc}\left(\Omega_0 L_i k_i^-\right) \tag{4.25}$$

and $\sigma_i^A = \arg(M_i^A)$.

The time-domain expression of the GW strain in the pseudo-detector A is obtained by taking the Fourier transform of $\tilde{h}^A(\omega)$, and is found to be

$$h^A(t) = H(\Omega_0) \sum_{j=1}^{3} \Re\left[e^{-i\delta} E_j^{A*}\, S_j(t)\right] \quad , \tag{4.26}$$

where $\delta = \delta_c + \pi/2$,

$$S_j^A := e^{i\Phi_j + i\sigma_j^A}/g^A \quad \text{and} \quad E_j^A := g^A T_2{}^{\rho}\, D_{j\,\rho}{}^{A}\,. \tag{4.27}$$

Above, g^A is a normalization constant such that

$$\langle S_j^A, S_j^A \rangle = 1 \quad , \tag{4.28}$$

which implies that for an observation duration (i.e., signal integration time) T,

$$g^A = \left[\frac{T}{2\pi P_A(\Omega_0)}\right]^{1/2} . \tag{4.29}$$

When considering a slightly chirping source, the straight substitution of $\Omega_0 t$ with $\Omega_0 t + \frac{1}{2}\dot{\Omega}_0 t^2$ will suffice where

$$\dot{\Omega} = \frac{48}{5}\left(\frac{G\mathcal{M}}{2}\right)^{5/3} \Omega^{11/3}. \tag{4.30}$$

This requires a modification to $h^A(t)$ which occurs in the S_i^A term:

$$S_j^A := e^{i\Omega_0(t - L_j\tau_j) + i\phi_D(t) + i(\frac{1}{2}\dot{\Omega}_0 t^2 + \sigma_j^A)}/g^A. \tag{4.31}$$

Note that apart from the normalization constant, S_j^A is a pure phase term. We will find this

useful when deducing the matched filter in the following section.

4.2.2 The Optimal Statistic

Given three independent pseudo-detectors, x^A, we now ask what is the optimal detection statistic to look for GW signals, h^A, in them. In the absence of any prior probabilities and costs, the optimal detection strategy is the one that minimizes the rate of false dismissals for a given rate of false alarms. This is termed as the Neyman-Pearson criterion. Under this criterion and in zero-mean Gaussian noise, the detection statistic is the likelihood ratio, λ, defined as [25]

$$\ln \lambda = \sum_{A=1}^{3} \left(\langle h^A, x^A \rangle_{(A)} - \frac{1}{2} \langle h^A, h^A \rangle_{(A)} \right) \quad , \tag{4.32}$$

where the first term is the cross-correlation of the expected signal, h^A, in each pseudo-detector and the respective data, x^A. The second term is an overall normalization that is independent of the data. The cross-correlation can be performed in either the frequency domain or time domain. It is defined to be

$$\langle a, b \rangle = \frac{2}{P(f)} \int_0^\infty a(t)\, b(t) dt = 2\Re \int_0^\infty \frac{\tilde{a(f)}^* \, \tilde{b(f)}}{P(f)} df \tag{4.33}$$

where $\tilde{a(f)}$ is the Fourier transform of $a(t)$. Substituting for h^A from Eq. (4.26), we get:

$$\sum_{A=1}^{3} \langle h^A(t), x^A(t) \rangle_{(A)} = \sum_{A=1}^{3} \sum_{i=1}^{3} \Re \left[e^{-i\delta} \, E_i^{A*} \, C_i^A(t) \right] \quad , \tag{4.34}$$

where

$$C_i^A(t) := \langle S_i(t), x^A(t) \rangle_{(A)} \, . \tag{4.35}$$

The double summation in Eq. (4.34) can be replaced with the single sum over a new index k,

$$\sum_{A=1}^{3}\sum_{i=1}^{3} Y_i^A := \sum_{k=1}^{9} Y^{\lceil \frac{k}{3} \rceil}_{(k-1)\%3+1} \quad , \tag{4.36}$$

where $A = \text{Ceiling}(k/3) = \lceil \frac{k}{3} \rceil$ and $i = \text{Mod}(k-1,3)+1 = (k-1)\%3+1$. Below, we will simplify the expressions by identifying $Y^{\lceil \frac{k}{3} \rceil}_{(k-1)\%3+1}$ with Y^k, which will comprise the components of the 9-dimensional vector $\mathbf{Y}$. We use this algorithm to map the D_i^A, E_i^A, and C_i^A to the components, D^k, E^k, and C^k of 9-dimensional vectors $\mathbf{D}$, $\mathbf{E}$, and $\mathbf{C}$, respectively.

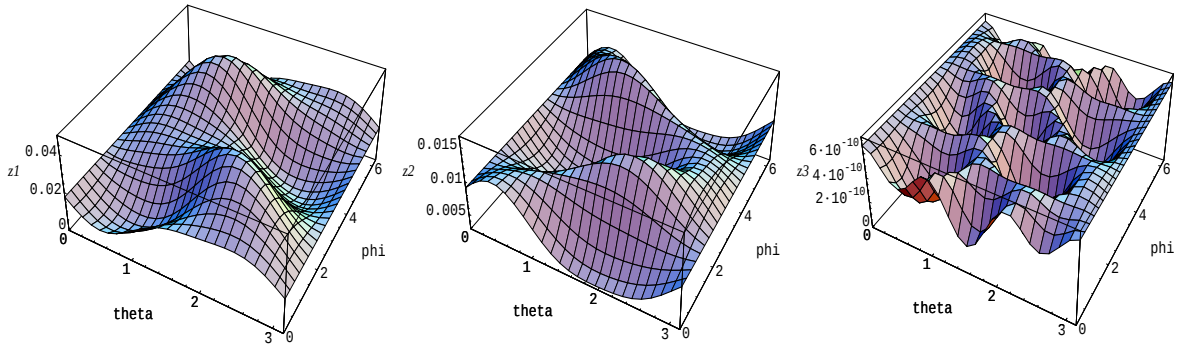

Figure 4.2: Sensitivities $z_A := \sum_{i=1}^{3} E_A^{i*} E_i^A/(g^A)^2$ of the three pseudo-detectors as functions of sky positions, $\{\theta, \phi\}$, in radians. These plots have been evaluated for $\Omega_0 = 1$ mHz at the "initial" orbital position of LISA labeled $t = 0$. As illustrated above, direction of maximum sensitivity varies from one pseudo-detector to another.

In the new notation, the cross-correlation statistic becomes

$$\sum_{A=1}^{3} \langle h^A(t), x^A(t) \rangle_{(A)} = \sum_{k=1}^{9} \Re\left[e^{-i\delta}\, E_k^*\, C^k\right] = \Re\left[e^{-i\delta}\, \mathbf{E}\cdot\mathbf{C}\right] \tag{4.37}$$

and

$$\sum_{A=1}^{3} \langle h^A(t), h^A(t) \rangle_{(A)} = H^2(\Omega_0) \parallel \mathbf{E} \parallel^2 \equiv \kappa^2 \quad , \tag{4.38}$$

where $\parallel \mathbf{Y} \parallel$ denotes the norm of vector $\mathbf{Y}$. Therefore, κ^2 is a measure of the drop in the

peak power $H^2(\Omega_0)$ owing to LISA's non-optimal orientation to a given source. The relative sensitivities of the three pseudo-detectors to different sky positions can now be studied by plotting the analogue of κ^2 for each individual pseudo-detector, as shown in Fig. 4.2. This figure, plotted for $\Omega_0 = 1$ mHz, verifies the fact found in Ref. [16] that the third pseudo-detector has a much smaller sensitivity than the first two. It also, shows that the *peak* sensitivity of the pseudo-detector labeled as $A = 1$ is the best of the three. However, at any given location on LISA's orbit, there are sky positions to which pseudo-detector 2 has the best sensitivity. We also plot in Figs. 4.3 and 4.4, the sensitivities of pseudo-detector 1 and the optimal combination of all the pseudo-detectors, for three different locations on LISA's orbit. These figures show that for all sky positions the optimal-sensitivity is better than the usually best pseudo-detector, labeled $A = 1$.

The likelihood ratio now takes the following form:

$$\ln \lambda = \kappa \sum_{A=1}^{3} \langle \hat{h}^A, x^A \rangle_{(A)} - \frac{1}{2}\kappa^2, \tag{4.39}$$

where

$$\hat{h}^A \equiv \frac{h^A}{H(\Omega_0) \parallel \mathbf{E} \parallel}. \tag{4.40}$$

This can be maximized over κ and δ to give

$$\ln \lambda \mid_{\hat{\kappa},\hat{\delta}} = \frac{1}{2} \mid \mathbf{Q} \cdot \mathbf{C} \mid^{\mathbf{2}} . \tag{4.41}$$

Note that the parameters $\{\psi, \iota\}$ appear only in $\mathbf{Q}$.

To make further progress, let us introduce the normalized network (or multi-detector) vector,

$$\mathbf{Q} := \mathbf{E}/\parallel \mathbf{E} \parallel \ , \tag{4.42}$$

such that $\parallel \mathbf{Q} \parallel = 1$. $\mathbf{Q}$ can be expressed in terms of its components as follows:

$$\mathbf{Q} := Q^{+2}\hat{\mathbf{D}}_{+2} + Q^{-2}\hat{\mathbf{D}}_{-2}, \tag{4.43}$$

where

$$\hat{\mathbf{D}}_{\pm 2} := \frac{\mathbf{D}_{\pm}}{\parallel \mathbf{D} \parallel} \quad \text{and} \quad Q^{\pm 2} := \frac{T_2^{\pm 2} \ \parallel \mathbf{D} \parallel}{\parallel \mathbf{E} \parallel}\,. \tag{4.44}$$

Above, we have used the fact that $\parallel \mathbf{D}_+ \parallel = \parallel \mathbf{D}_- \parallel \equiv \parallel \mathbf{D} \parallel$. The statistic in Eq. (4.41) has all the $\{\psi, \iota\}$ dependence on $\mathbf{Q}$. Therefore, it stands maximized with respect to those parameters when $\mathbf{Q}$ gets aligned with $\mathbf{C}$. The fact that this is realizable was shown in Ref. [27]. The maximized statistic is

$$\ln \lambda|_{\hat{\kappa},\hat{\delta},\hat{\psi},\hat{\iota}} = \frac{1}{2} \parallel \mathbf{C}_{\mathcal{H}} \parallel^{\mathbf{2}}, \tag{4.45}$$

where $\mathbf{C}_{\mathcal{H}}$ is the projection of $\mathbf{C}$ on the 2-dimensional complex space $\mathcal{H}$ spanned by $\{\hat{\mathbf{D}}_{+2}, \hat{\mathbf{D}}_{-2}\}$. Since it is always possible to choose a pair of real basis vectors to define this two-dimensional space, we take these vectors to be

$$\hat{\mathbf{v}}^{\pm} := \left(\hat{\mathbf{d}}_1 \pm \hat{\mathbf{d}}_2\right) / \parallel \hat{\mathbf{d}}_1 \pm \hat{\mathbf{d}}_2 \parallel \ , \tag{4.46}$$

where $\mathbf{d}_1 = \Re(\mathbf{D}_{+2})$ and $\mathbf{d}_2 = \Im(\mathbf{D}_{+2})$. Thus, we may define the network search statistic as

$$\Lambda := \parallel \mathbf{C}_{\mathcal{H}} \parallel^2 = |C^+|^2 + |C^-|^2 = (c_0^+)^2 + (c_{\pi/2}^+)^2 + (c_0^-)^2 + (c_{\pi/2}^-)^2 \ , \tag{4.47}$$

where $C^{\pm} := \hat{\mathbf{v}}^{\pm} \cdot \mathbf{C} =: c_0^{\pm} + i c_{\pi/2}^{\pm}$.

The above statistic is still a function of the sky position through the parameters $\{w_1, w_2\}$.

Since it is not possible to maximize the statistic over these parameters analytically, one must resort to a numerical maximization scheme as described in the next section. By comparing the values of the statistic for each pixel in the sky with a threshold value, Λ_0, a decision on the presence or absence of a signal in the data can be made. The threshold itself is determined by the false-alarm probability that one can afford. Note that in the absence of a signal, Λ is a random variable that has a χ^2 probability distribution,

$$p_0(\Lambda) = \frac{\Lambda}{4} \exp\left(-\Lambda/2\right) \quad , \tag{4.48}$$

with 4 degrees of freedom [24]. The false-alarm probability is

$$Q_0 = \int_{\Lambda_0}^{\infty} p_0(\Lambda) d(\Lambda) = \left(1 + \frac{\Lambda_0}{2}\right) \exp\left(-\Lambda_0/2\right) \, . \tag{4.49}$$

In the presence of a signal, the probability distribution of Λ is non-central χ^2,

$$p_1(\Lambda) = \frac{\sqrt{\Lambda}}{2\kappa} \exp\left(-\frac{\Lambda + \kappa^2}{2}\right) I_1\left(\kappa\sqrt{\Lambda}\right) \quad , \tag{4.50}$$

with the non-centrality parameter as κ^2, which is a measure of the signal strength [24]. Above, I_1 is the modified Bessel function.

4.2.3 Template Spacing and Computational Costs

The Λ statistic in Eq. (4.45) must be maximized over the remaining intrinsic parameters, namely, $\boldsymbol{\vartheta} = \{\Omega_0, w_1, w_2\}$. The maximization can be achieved numerically using a discrete template bank over this three-dimensional parameter space. The drop in the value of the statistic and, therefore, the signal-to-noise ratio that one can afford determines how coarsely one can space the templates. In practice, there are limits posed by the available computa-

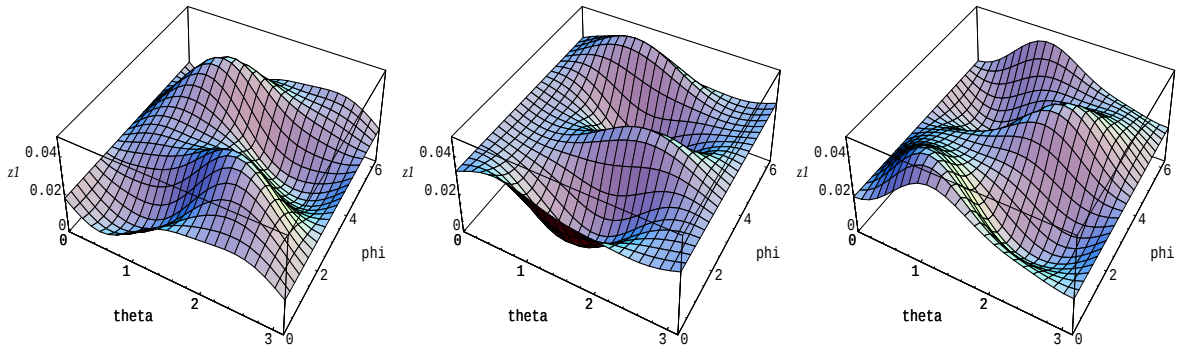

Figure 4.3: Sensitivity z_1, as defined in Fig. 4.2, evaluated at $\Omega_0 = 1$ mHz for three different angular orbital positions (in radians), $\{0, \frac{\pi}{3}, \frac{2\pi}{3}\}$, with respect to the "initial" location denoted in Fig. 4.2. The left plot above is identical to the left plot in Fig. 4.2 since it corresponds to the same pseudo-detector and orbital location. Note that the sky positions corresponding to the sensitivity maxima vary from one location to another on LISA's orbit.

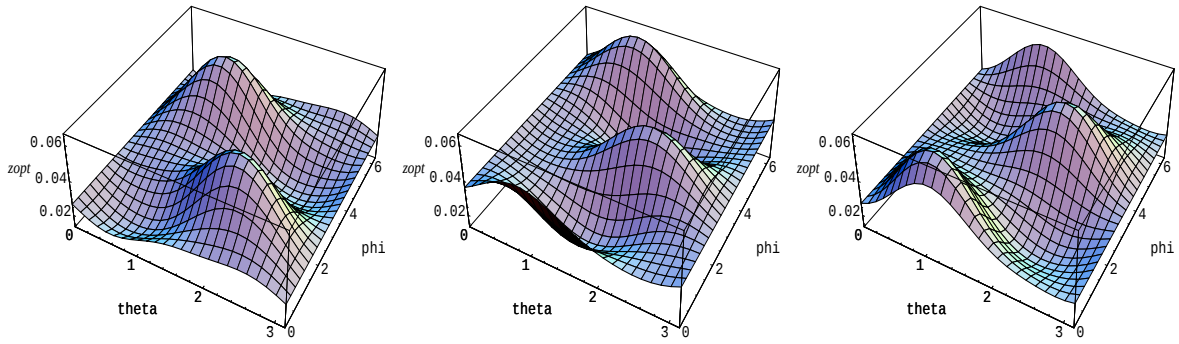

Figure 4.4: Network sensitivity $z_{opt} := \| \mathbf{E} \| /(g^1)^2$ evaluated at $\Omega_0 = 1$ mHz for the same orbital positions that appear in Fig. 4.3. It is manifest that pseudo-detector 3 makes negligible contribution to the z_{opt} at this frequency. Note that $g^1 = g^2$. At any given sky position, the optimal statistic has better sensitivity than any z_A.

tional resources on how fine the spacing can be. The loss in SNR is related to the template spacing through the ambiguity function [25].

The ambiguity function corresponding to the Λ statistic is derived from it by replacing the data x^A there by a signal $h^A(\boldsymbol{\vartheta}')$. We distinguish the signal parameter values from those of the template by denoting the former with a prime. The parameter values of a template used in a search may not be the same as those of a signal hiding in the data. Let the

parameter mismatch be $\Delta\boldsymbol{\vartheta} := (\boldsymbol{\vartheta}' - \boldsymbol{\vartheta})$. Then the ambiguity function is a real quantity expressed as

$$m(\boldsymbol{\vartheta}, \Delta\boldsymbol{\vartheta}) := p_k{}^l Q'^k \, Q'^*_l \Theta_{(k)(l)}, \tag{4.51}$$

where Q'^k depends only on the signal parameters and

$$\begin{aligned} \Theta_{(k)(l)} &= \langle S'^{\,k}, S^k \rangle^*_{(k)} \langle S'^{\,l}, S^l \rangle_{(l)} \\ &= e^{i\Psi_k} e^{i\Psi_l} \mathrm{sinc}(\Omega'_k T - \Omega_k T) \mathrm{sinc}(\Omega'_l T - \Omega_l T), \end{aligned} \tag{4.52}$$

and $p_k{}^l := v^{+l} v^+_k + v^{-l} v^-_k$ is an amplitude factor. It is important to note that as $\Delta\boldsymbol{\vartheta} \to 0$, one has $m(\boldsymbol{\vartheta}, \Delta\boldsymbol{\vartheta}) \to 1$, which is the maximum value it can attain. The correlation phase, Ψ_k, is defined as

$$\Psi_k = L(\Omega'_k \tau'_k - \Omega_k \tau_k) = \Omega_k \frac{\hat{r}_{k1}}{2\sqrt{3}} \Delta w_1 + \Omega_k \frac{\hat{r}_{k2}}{2\sqrt{3}} \Delta w_2 - \tau_k \Delta\Omega_k. \tag{4.53}$$

The drop in the value of $m(\boldsymbol{\vartheta}, \Delta\boldsymbol{\vartheta})$ caused by non-zero, but small $\Delta\vartheta^\mu$, can be ascertained by Taylor expanding it about the maximum at $\Delta\boldsymbol{\vartheta} = 0$ [26, 27]. The first order term is zero since by definition the statistic has a maximum when the template parameters match the signal parameters. Thus,

$$1 - m(\boldsymbol{\vartheta}, \Delta\boldsymbol{\vartheta}) \simeq \gamma_{\alpha\beta} \Delta\vartheta^\alpha \Delta\vartheta^\beta \quad , \tag{4.54}$$

$\gamma_{\alpha\beta}$ is determined from the second order term in that expansion:

$$\gamma_{\alpha\beta} = -\frac{1}{2} \left(\frac{\partial^2 m(\boldsymbol{\vartheta}, \Delta\boldsymbol{\vartheta})}{\partial\Delta\vartheta^\alpha \partial\Delta\vartheta^\beta} \right) \Bigg|_{\Delta\boldsymbol{\vartheta}=0}. \tag{4.55}$$

It defines the metric on the 3-dimensional parameter space.

The computational cost for the search can be reduced by taking advantage of the Fast Fourier Transform algorithms [28] and computing the cross-correlation components, $\mathbf{C}$, in the Fourier domain. This defines the strategy for searching for the source frequency, Ω_0. To search for the remaining parameters, $\{w_1, w_2\}$, one must design a bank of "templates" with values of these sky positions spaced such that the loss in SNR is never more than the desired fraction, say, μ. To find the metric, g_{ij}, on the two-dimensional space $\mathcal{P}$, spanned by $\{w_1, w_2\}$, one must project $\gamma_{\alpha\beta}$ orthogonal to Ω_0,

$$g_{ij} = \gamma_{ij} - \frac{\gamma_{0i}\gamma_{0j}}{\gamma_{00}} \quad , \tag{4.56}$$

where i and j span only the $\{w_1, w_2\}$ space, and the index 0 denotes the Ω_0 axis. The volume of a $\mathcal{P}$ is then given by

$$\mathcal{V} = \int_{\mathcal{P}} \sqrt{\det\|g_{ab}\|} d^P\vartheta \quad , \tag{4.57}$$

where $P = 2$ is the dimensionality of the space. The number density of templates, $\rho_P(\mu)$, is determined as a function of μ to be [27]:

$$\rho_P(\mu) = \left(\frac{1}{2}\sqrt{\frac{P}{\mu}}\right)^P \quad . \tag{4.58}$$

Setting the fractional SNR loss $\mu = 3\%$ yields a template density of $\rho_2(0.03) = 16.6$. Therefore, the total number of templates is just the overall parameter volume times the template density, i.e., $N_{\text{templates}} = \mathcal{V} \times \rho_P(\mu)$.

The parameter volume, obtained via the metric computation, turns out to be about 5 for $\Omega_0 = 1$ mHz. Considering that the template density per unit volume is only 16.6 implies that the number of sky-position templates required for a search with 3% loss of SNR

will be around 80. The smallness of this number is not surprising, given how slowly the ambiguity function varies as a function of $\Delta\theta$ and $\Delta\phi$, as shown in Fig. 4.5. What should be noted is that although the total number of templates needed is small, this only ensure that a signal will not go undetected but still does not provide the necessary resolution to properly identify actual source parameters. This topic will be discussed in greater detail in the following chapter.

As is manifest from Eq. (4.51), in principle, this variation can arise from either the time delays in Θ_{kl} or the weights $p_k{}^l$. However, for wavelengths much larger than the LISA arm length, the ability to discern between different sky positions through the time delays in Θ_{kl} is negligible. The main contribution to $m(\boldsymbol{\vartheta}, \Delta\boldsymbol{\vartheta})$, therefore, arises from the $p_k{}^l$. A detailed study of the angular resolution achievable by LISA is covered in the following chapter or the reader may refer to the following chapter Refs. [66, 67].

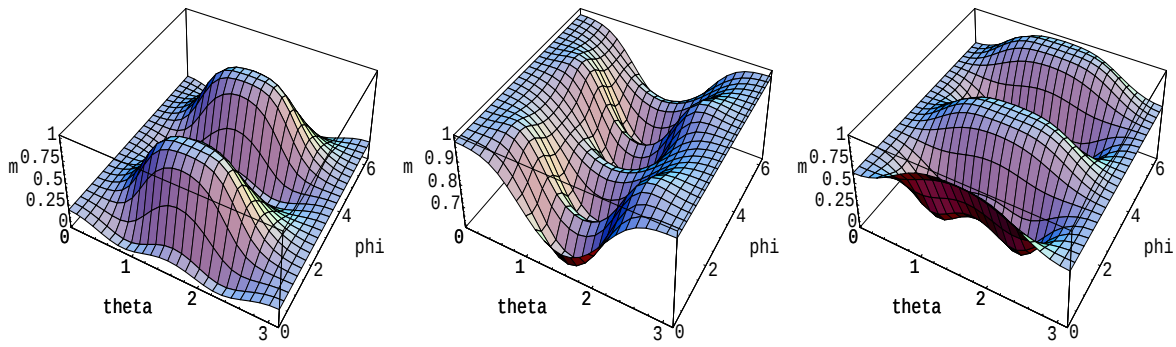

Figure 4.5: The ambiguity function m plotted as a function of the template parameters, $\{\theta, \phi\}$, for three different source sky positions (in radians), namely, $\{\theta', \phi'\} = \{\pi/2, 4\pi/3\}$, $\{\pi/6, \pi/3\}$, and $\{\pi/2, \pi\}$.

To get a handle on the computational costs associated with a search of this nature, one must determine the overall number of sampling points in a single data train. For our analysis, a chosen a sampling rate of 1 Hz was used. Therefore, the number of sampling points is just

the length of the data train, T. The number of floating point operations associated with an FFT with T sampling points is:

$$N_{\mathrm{fl-opts}} = T \log_2 T. \tag{4.59}$$

Considering that this must be done for each template, the resulting expression for the total number of floating point operations for an arbitrary template bank is just $N_{\mathrm{templates}} \times N_{\mathrm{ft-opts}}$. However, the real quantity of interest is the number of operations per second,

$$C^{\mathrm{flops}} := \frac{N_{\mathrm{templates}} \times N_{\mathrm{ft-opts}}}{T} = N_{\mathrm{templates}} \log_2 T\,. \tag{4.60}$$

Therefore, the computational costs of implementing a real-time search with about 80 templates is trivial since the number of flops scales logarithmically with the integration time. In the analysis presented here, the template bank is only valid in a time frame where the beam pattern functions are relatively constant. This can be anywhere from a few hours to a day. Therefore there would be separate banks for each integration period. This results in a little overhead associated with switching to the new template bank for each integration period but it is minimal and has been ignored here.

4.3 Eccentric Waveforms

The Laser Interferometer Space Antenna (LISA) is projected to detect numerous galactic stellar-mass compact binaries [37] of which a good fraction is expected to possess moderate to large values of orbital eccentricity in the LISA band. It was demonstrated that a natural consequence of an asymmetric kick imparted to neutron stars (NSs) at birth is that a ma-

jority of them in binaries should have highly eccentric orbits with short orbital periods [38]. Assuming stationary distribution for NS-NS binaries in the galaxy, Gusev et al. argued that LISA will see a number of NS–NS, NS–black hole (BH) and BH–BH binaries in eccentric orbits [43]. Moreover, using Monte Carlo simulations to model galactic globular clusters, it has been predicted that LISA may see several stellar-mass BH binaries in highly eccentric orbits [44]. Observing these binaries with LISA is of great astrophysical interest because for many of them it will provide at least the total mass [15], angular resolution sufficient to identify their location [44] and, in principle, a bound on the mass of gravitons [41].

Owing to the possibility of signals from many eccentric binary compact objects (EBCOs) populating LISA's data, we examine how one must search for them. To beat the noise from laser-frequency fluctuation and optical-bench motion, we take the data to be the first generation time-delay interferometric (TDI) observables A, E, and T [16]. We make a start here by focusing on the relatively simple, yet astrophysically relevant, case of EBCOs satisfying the following two conditions. First, we consider only those EBCOs whose orbital dynamics are negligibly affected by gravitational radiation reaction, thus, allowing us to treat individual signal harmonics as monochromatic in an observation period of a few years. However, we keep the orbital dynamics to be fully first post-Newtonian (1PN) accurate. This is because for stellar-mass compact binaries in eccentric orbits, with orbital frequency around 1mHz, it is more important to include the frequency shift due to periastron advance (which appears at the 1PN order) than that caused by radiation reaction, appearing at the 2.5PN order [15]. The second requirement is that here we limit the orbital eccentricities to be less than 0.6. This allows us to simplify the TDI analysis by effecting the long-wavelength approximation, where the wavelengths of the dominant harmonics are larger than LISA's

arm-length.

The data analysis problem for our eccentric binaries is essentially that of tracking multiple Doppler-shifted lines, with frequencies defined by the source masses, orbital angular frequency, and eccentricity. There are a few relevant extrinsic parameters as well, namely, the initial phase of the signal, and the initial and final harmonics, since the LISA noise curve may make it sub-optimal to search for power below and above certain frequencies. This problem is reminiscent of tracking multiple pulsars with multiple detectors, studied by Cutler and Schutz [36]. There are some important differences though: In our case (a) the line strengths of the different harmonics are not independent, (b) the antenna-pattern functions of LISA's arms are frequency dependent, but are all determined by the same sky-position, and (c) the current analysis is in TDI observables. Owing to point (a) above, the optimal statistic is not a simple linear sum of the statistics of individual harmonics (even if the harmonics are well separated such that the detector noise at their frequencies are uncorrelated). Rather, as we show below, the optimal search statistic for this case has important cross terms between harmonics, bearing testimony to the linear dependence of the different harmonics.

4.4 The gravitational waveforms and the associated LISA signal

We present a recent prescription that provides accurate gravitational-wave polarizations associated with compact binaries of arbitrary masses moving in slowly precessing eccentric orbits with negligible inspiral [47]. This prescription is heavily influenced by the orbital

phasing formalism given in Refs. [45, 46]. Consider a (non-spinning) EBCO with component masses m_1 and m_2, such that the total mass is $m = m_1 + m_2$ and the symmetric mass ratio is $\eta = m_1 m_2/m^2$. Let its luminosity distance be R and its orbital inclination relative to the line of sight be ι. Let r and φ denote the relative separation and the orbital phase of the binary. Then the dominant quadrupolar contributions to the two polarization components of the source moving in non-circular orbit are [45]:

$$\begin{aligned} h_+(t) &= \frac{(1+\cos^2\iota)}{2}\left[h_x(t)\cos 2\varphi(t) - h_y(t)\sin 2\varphi(t)\right] + \sin^2\iota\; h_z(t) \\ &= \frac{(1+\cos^2\iota)}{2} H(t)\sin\left(2\varphi(t) + 2\gamma(t)\right) + \sin^2\iota\; h_z(t)\,, \qquad (4.61) \\ h_\times(t) &= \cos\iota\left[h_x(t)\sin 2\varphi(t) + h_y(t)\cos 2\varphi(t)\right] \\ &= \cos\iota\; H(t)\sin\left(2\varphi(t) + 2\gamma(t)\right)\,, \qquad (4.62) \end{aligned}$$

where we define the following dimensionless quantities

$$\begin{aligned} h_{x,y}(t) &= -h_0\left(\frac{Gm}{c^2 r} \pm \frac{r^2\varphi'^2}{c^2} - \frac{r'^2}{c^2}\right), \quad h_z(t) = \frac{2\,h_0\, rr'\varphi'}{c^2}\,, \qquad (4.63) \\ H(t) &= \sqrt{h_x^2(t) + h_y^2(t)}\,, \quad \gamma(t) = \arctan\left(\frac{h_y(t)}{h_x(t)}\right), \qquad (4.64) \end{aligned}$$

where $h_0 \equiv 2Gm\eta/c^2R$ and the prime denotes a time derivative. In Eqs. 4.63, the temporal evolutions are provided by the 1PN accurate evolution of r, φ, and their time derivatives. in a suitably defined center-of-mass frame. With the help of 1PN accurate quasi-Keplerian parameterization for compact binaries in eccentric orbits [39], we provide the following 1PN accurate parametric descriptions of these variables in terms of the eccentric anomaly, u [see sec. IV in Ref. [45] for the computational details]:

$$
\begin{aligned}
r &= \left(\frac{Gm}{n^2}\right)^{1/3}(1-e_t\cos u)\left[1+\mathcal{O}\left(\frac{1}{c^2}\right)\right], \\
r' &= \frac{e_t(Gmn)^{1/3}}{(1-e_t\cos u)}, \left[1+\mathcal{O}\left(\frac{1}{c^2}\right)\right] \quad \varphi' = \frac{n\sqrt{1-e_t^2}}{(1-e_t\cos u)^2}\left[1+\mathcal{O}\left(\frac{1}{c^2}\right)\right], \qquad (4.65)
\end{aligned}
$$

where n is the 1PN accurate mean motion, defined by $n = 2\pi/P$, P being the orbital period. Also, e_t is the eccentricity associated with the 1PN accurate Kepler equation (KE), $l \equiv n\,t = u - e_t\,\sin u$, where l is termed as the mean anomaly.

The parametric description for the orbital phase requires special consideration and is given by

$$
\varphi(l) = p\,n\,t + W(l) + \varphi_0\,, \qquad (4.66)
$$

where φ_0 is the initial orbital phase. The quantities W and p are, respectively,

$$
W(l) = p(v - u + e_t\sin u), \quad p = 1 + \frac{3\zeta^{2/3}}{1-e_t^2}\,, \qquad (4.67)
$$

with

$$
v = 2\arctan\left[\left(\frac{1+e_\varphi}{1-e_\varphi}\right)^{1/2}\tan\frac{u}{2}\right], \quad e_\varphi = e_t\Big[1+\zeta^{2/3}\,(4-\eta)\Big], \qquad (4.68)
$$

and $\zeta \equiv Gmn/c^3$. The explicit time evolution of $h_+(t)$ and $h_\times(t)$ is found by solving the 1PN accurate KE given above. The most efficient and accurate (numerical) way of solving it, adapting a method found by Mikkola [40], was recently employed in Ref. [47].

Let (θ, ϕ) denote the sky-position of a GW source in the ecliptic coordinate system with its origin at the solar system barycenter, and $\hat{\mathbf{w}}(\theta,\phi)$ be the unit vector pointing at that source. Then the strain in LISA's ith arm caused by GWs arriving from it is

$$h_i(t) = h_+(t)\xi_{i+}(\theta,\phi) + h_\times(t)\xi_{i\times}(\theta,\phi) \quad , \tag{4.69}$$

where $\xi_{i+}(t) = (\hat{\boldsymbol{\theta}}\cdot\hat{\mathbf{n}}_i(t))^2 - (\hat{\boldsymbol{\phi}}\cdot\hat{\mathbf{n}}_i(t))^2$ and $\xi_{i\times}(t) = 2(\hat{\boldsymbol{\theta}}\cdot\hat{\mathbf{n}}_i(t))(\hat{\boldsymbol{\phi}}\cdot\hat{\mathbf{n}}_i(t))$ are that arm's antenna-pattern functions. Here, $\hat{\mathbf{n}}_i(t)$ is a unit vector along LISA's ith arm, $\hat{\boldsymbol{\theta}} \equiv \partial\hat{\mathbf{w}}/\partial\theta$, and $\hat{\boldsymbol{\phi}} \equiv \partial\hat{\mathbf{w}}/\partial\phi$. The length of each arm is taken to be $L_i \equiv L$, for all i.

Following Ref. [36], the total signal can be written as:

$$h_i(t) = \sum_{a=1}^{4} \lambda^a h_{ia} + \xi_{i+} h_z(t)\,. \tag{4.70}$$

Above, the basis waveforms are:

$$\begin{aligned} h_{i1}(t) &= \mathcal{F}_{i+}(t)H(t)\cos(2\chi(t))\,, \quad h_{i2}(t) = \mathcal{F}_{i\times}(t)H(t)\cos(2\chi(t))\,, \\ h_{i3}(t) &= \mathcal{F}_{i+}(t)H(t)\sin(2\chi(t))\,, \quad h_{i4}(t) = \mathcal{F}_{i\times}(t)H(t)\sin(2\chi(t))\,, \end{aligned} \tag{4.71}$$

with the sky-position-dependent $\mathcal{F}_{i+,\times}$ related to $\xi_{i+,\times}$ as follows:

$$\begin{pmatrix} \xi_{i+} \\ \xi_{i\times} \end{pmatrix} \equiv \begin{pmatrix} \cos 2\psi & \sin 2\psi \\ -\sin 2\psi & \cos 2\psi \end{pmatrix} \begin{pmatrix} \mathcal{F}_{i+} \\ \mathcal{F}_{i\times} \end{pmatrix}\,, \tag{4.72}$$

and

$$\chi(t) \equiv pl(t) + W(t) + \gamma(t) + \varphi_D(t:\theta,\phi) \quad , \tag{4.73}$$

where ψ is the initial polarization angle and φ_D is the Doppler phase. The expansion coefficients here are the same as those for long-duration monochromatic sources [48]

$$\begin{aligned} \lambda^1 &= h_{+0}\cos 2\varphi_0 \cos 2\psi - h_{\times 0}\sin 2\varphi_0 \sin 2\psi\,, \\ \lambda^2 &= h_{+0}\cos 2\varphi_0 \sin 2\psi + h_{\times 0}\sin 2\varphi_0 \cos 2\psi\,, \\ \lambda^3 &= -h_{+0}\sin 2\varphi_0 \cos 2\psi - h_{\times 0}\cos 2\varphi_0 \sin 2\psi\,, \\ \lambda^4 &= -h_{+0}\sin 2\varphi_0 \sin 2\psi + h_{\times 0}\cos 2\varphi_0 \cos 2\psi\,, \end{aligned} \tag{4.74}$$

where $h_{+0} \equiv (1+\cos^2\iota)h_0/2$ and $h_{\times 0} \equiv \cos\iota\ h_0$. For eccentricities less than 0.6, the contribution of h_z to the total strain is found to be negligible [47].

4.5 The GW signal in TDI observables

There are three noise-independent TDI observables, termed as A, E, T, following Ref. [16]. In the long-wavelength (LW) limit, whereby the antenna-pattern functions can be treated as frequency independent, the magnitudes of the GW strain in these are,

$$\begin{aligned} A^{\rm GW} &\simeq \Big[\left(2\mathcal{F}_{2+}(t) - \mathcal{F}_{1+}(t) - \mathcal{F}_{3+}(t)\right)\left(\lambda^1 S(t) - \lambda^3 C(t)\right) \\ &\quad + \left(2\mathcal{F}_{2\times}(t) - \mathcal{F}_{1\times}(t) - \mathcal{F}_{3\times}(t)\right)\left(\lambda^2 S(t) - \lambda^4 C(t)\right)\Big] , \\ E^{\rm GW} &\simeq \sqrt{3}\Big[\left(\mathcal{F}_{3+}(t) - \mathcal{F}_{1+}(t)\right)\left(\lambda^1 S(t) - \lambda^3 C(t)\right) \\ &\quad + \left(\mathcal{F}_{3\times}(t) - \mathcal{F}_{1\times}(t)\right)\left(\lambda^2 S(t) - \lambda^4 C(t)\right)\Big] , \end{aligned} \tag{4.75}$$

and $T^{\rm GW} \simeq \mathcal{O}\left((nL)^4\right)$. Above, we defined

$$S(t) = \sum_J 6\sqrt{2}\left(\omega_J L/c\right)^3 \left(\alpha_J \cos\left(\omega_J t\right) - \beta_J \sin\left(\omega_J t\right)\right) , \tag{4.76}$$

$$C(t) = \sum_J 6\sqrt{2}\left(\omega_J L/c\right)^3 \left(\alpha_J \sin\left(\omega_J t\right) + \beta_J \cos\left(\omega_J t\right)\right) , \tag{4.77}$$

where $\omega_J \equiv n(J+2p)$, and the frequency index J varies within an integral range, $\{J_0, J_c\}$, determined by the relative strength of the signal harmonics and LISA's sensitivity curve. Also, α_J and β_J are eccentricity-dependent 1PN accurate Fourier components [47]. Just like $h(t)$, the TDI observables can also be linearly expanded over the λ^a, viz., $X^{\rm GW} \simeq \sum_a \lambda^a X_a$, where X is A, E, or T. Thus, the 1PN EBCO waveforms are parameterized by twelve parameters, $(R, \varphi_0, \psi, \iota, m, \eta, n, e_t, \theta, \phi, J_0, J_c)$, with the first four being interchangeable with

the λ^a.

4.6 The detection statistic

For eccentric binaries, the GW polarization components are constituted of several harmonics of the orbital frequency. A suitable representation of the EBCO signal in terms of these harmonics is given in Ref. [47]. Past experience with the monochromatic signals suggests that the optimal statistic will entail cross correlations between the TDI observables and the GW templates in that data [19, 49]:

$$\begin{aligned} U_A &\simeq 2\langle A_1, A_1\rangle = 2\langle A_3, A_3\rangle\,, \quad V_A \simeq 2\langle A_2, A_2\rangle = 2\langle A_4, A_4\rangle\,, \\ Q_A &\simeq 2\langle A_1, A_2\rangle = 2\langle A_3, A_4\rangle\,, \quad P_A \simeq 2\langle A_1, A_4\rangle = -2\langle A_2, A_3\rangle\,, \end{aligned} \tag{4.78}$$

where for each harmonic of frequency ω, we defined

$$\langle X_a, X_b\rangle \equiv \frac{8(\omega L/c)^2 \sin^2(3\omega L/2c)}{T_{\rm obs} S_X^{\rm LW}(\omega)} \int_0^{T_{\rm obs}} X_a(t) X_b(t)\,. \tag{4.79}$$

Above, $T_{\rm obs}$ is the integration time and $S_X^{\rm LW}(\omega)$ is the noise PSD in observable X, in the LW limit. One obtains analogous quantities for E and T. In the LW limit, these can be further combined into network TDI templates, $Z = Z_A + Z_E$, where Z is U, V, Q, or P.

As has been explored in multiple papers [48, 19, 49, 50], the detection statistic derived from maximizing the likelihood ratio over the four parameters, λ^a, is the $\mathcal{F}$-statistic:

$$\mathcal{F} = \frac{1}{T_{\rm obs} D}\left[U\,|N_v|^2 + V\,|N_u|^2 - 2\Re\left(W N_v N_u^*\right)\right] \quad , \tag{4.80}$$

where $W \equiv Q + iP$, $D \equiv UV - |W|^2$ and, in the LW limit,

$$
\begin{aligned}
N_u &\simeq \int_0^{T_{\rm obs}} dt\Big[\sqrt{3}\,(2\mathcal{F}_{2+}(t)-\mathcal{F}_{1+}(t)-\mathcal{F}_{3+}(t))\,A(t)+(\mathcal{F}_{3+}(t)-\mathcal{F}_{1+}(t))\,E(t)\Big]\sum_J \frac{\kappa_J e^{\omega_J t}}{S_A^{\rm LW}(\omega_J)}\\
N_v &\simeq \int_0^{T_{\rm obs}} dt\Big[\sqrt{3}\,(2\mathcal{F}_{2\times}(t)-\mathcal{F}_{1\times}(t)-\mathcal{F}_{3\times}(t))\,A(t)+(\mathcal{F}_{3\times}(t)-\mathcal{F}_{1\times}(t))\,E(t)\Big]\sum_J \frac{\kappa_J e^{\omega_J t}}{S_A^{\rm LW}(\omega_J)}\,,
\end{aligned}
\tag{4.81}
$$

such that $\kappa_J \equiv 2\sqrt{6}(\omega_J L/c)^3\,(\alpha_J + i\beta_J)$.

4.7 The Signal-to-Noise Ratio

In this section, we compute the SNRs associated with the above search statistic for EBCO signals with different eccentricities in LISA data. However, for simplicity, here we explore the behavior of the SNR as a function of the eccentricity for signals in Michelson variables. (In a subsequent paper, we study its behavior in TDI variables and also explore the accuracy with which LISA will measure the astrophysical characteristics of EBCOs.) The Michelson data combinations can be simply written in terms of the individual arm strains, $\epsilon_i \equiv \delta L_i/L$, as follows:

$$
h^I(t) = \epsilon_1(t) - \epsilon_2(t)\,, \tag{4.82}
$$

$$
h^{II}(t) = \frac{1}{\sqrt{3}}\left[\epsilon_1(t)+\epsilon_2(t)-2\epsilon_3(t)\right]\,, \tag{4.83}
$$

where the superscripts I and II refer to the Michelson data combinations.

The results presented here assume the LW approximation, For a monochromatic signal with frequency up to about a millihertz, this causes less than a few percent loss in SNR relative to the exact case [51]. For the LW approximation to be valid for an EBCO signal,

the highest harmonic that contributes a non-negligible fraction of the total EBCO power should remain within a millihertz. This holds when the fundamental frequency and the eccentricity are low enough. This is because the contribution of the higher harmonics to the overall signal tapers off with increasing frequency. For that reason, eccentricities only up to $e_t = 0.6$ are presented. We are also accounting for the fact that the noise PSD is different at the different frequencies. It should be noted that a full rigorous solution that does track the individual frequency components with the rigid adiabatic approximation is currently being studied.

One can now see in Fig. 4.6 how the SNR behaves as one varies the eccentricity. This behavior is expected to hold for a more general EBCO as well. The three plots shown in Fig. 4.6 are for the same region of the parameter space, except for the eccentricity, which takes on the values $e_t = 0,\ 0.4,\ 0.6$, respectively. The other parameter values are $n/2\,\pi = 1\text{mHz}$, $\psi = 0$, and $\iota = 3\pi/10$ rads. These plots are normalized such that the largest SNR value among these plots is unity. This figure demonstrates the expected property that, all other parameters remaining equal, an EBCO with a larger eccentricity will emit more energy than one with a smaller eccentricity.

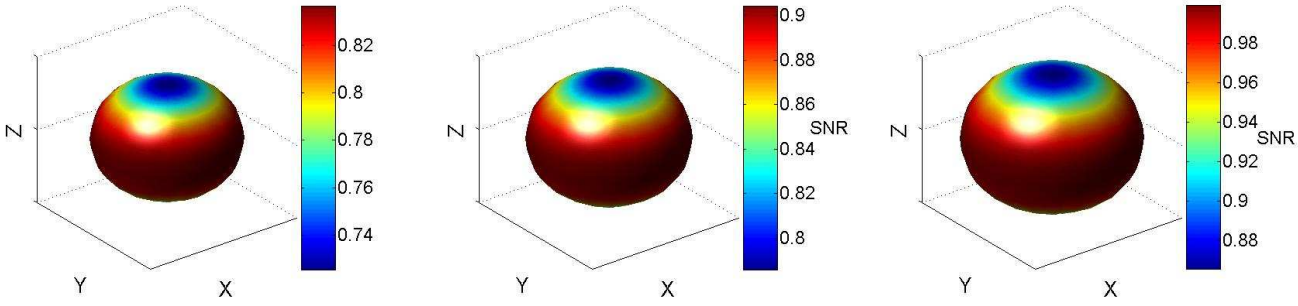

Figure 4.6: Normalized SNR, plotted as a function of sky position, for three different EBCOs, which have all other parameters identical, except $e_t = 0,\ 0.4,\ 0.6$ (left to right). The plots are normalized such that the highest SNR among the points plotted here is unity (which occurs in the left plot). Here, the ecliptic is oriented horizontally.

Chapter 5

Estimating Signal Parameters with LISA

Unlike LISA's existing earth-based counterparts, which include LIGO [53], VIRGO [54], TAMA [55], GEO [56], and LCGT [57], it will enjoy guaranteed sources, specifically galactic binaries, such as AM CVn, HP Lib, WD 0957-666, RXJ1914+245, and 4U1820-30 [58, 59]. In fact, LISA will be so sensitive that the population of galactic binaries of compact objects, which comprise white dwarfs (WDs), neutron stars (NSs), and black holes (BHs), will create source confusion noise that towers over LISA's instrumental noise near the sweet spot of its observation band [60, 61, 62]. This can potentially affect the detection of other GW sources.

The confusion noise from WD binaries will be especially worse below about 3 mHz, where a good fraction of it, with low signal strengths, will be unresolvable. This is due to the large population of existing binaries that are predicted by many populations models. Recent studies have suggested that there can be upwards of 10^8 galactic binaries that could contribute to this background confusion noise [35]. Galactic binaries that are bright enough

or orbiting fast enough form a potentially resolvable population extending up to about 20 mHz. LISA's ability to resolve this latter class of sources will largely depend on how well one can estimate their signal parameters. Population models have determined that the source that LISA will be able to resolve within a 1 year integration time can be as many as 5943 for white dwarf binaries or as low as 6 for binaries containing stellar mass black holes [35]. Although the development of algorithms for resolving the component sources is still at its nascency [63, 64, 65], it is already clear that the smallness of the parameter errors is of utmost significance to the success of any of these algorithms. The focus of this chapter is to study the role of different sources of these errors and determine the limits on how small these errors can be kept.

The problem of parameter-estimation accuracy has been studied for a variety of LISA sources in the past. Cutler did the first systematic study on this subject for monochromatic sources and super-massive black hole mergers [66]. Takahashi and Seto [67] studied the problem exclusively in the context of low-mass compact binaries. They placed emphasis on the determination of the chirp parameter and its role in unraveling the distance to a binary, following an idea due to Schutz [68]. Barack and Cutler [69] studied this problem in the context of extreme-mass-ratio inspiraling binaries. Vecchio and Wickham [51] extended earlier parameter estimation studies to beyond the long-wavelength approximation by including the frequency-dependent modulation of LISA's beam-pattern functions arising at higher frequencies. They showed that invoking this approximation results in at most a 3% loss in the SNR, but can have significant effects on the parameter accuracy (anywhere from 5% to a factor of 10) in the source frequency range $3\text{mHz} \lesssim \nu \lesssim 10\text{mHz}$.

All of these works, however, assumed that the data being filtered are two linearly indepen-

dent LISA data streams, called Michelson variables, which measure the differential changes of length in LISA's three arms. While these early works were instrumental in deriving useful lower-limits on the parameter errors of high signal-to-noise ratio sources, the attainability of these limits is unclear because the Michelson variables will suffer from the presence of excess noise arising from the laser frequency fluctuations and optical bench motion. The first noise source alone is sufficient to ruin LISA's characteristic strain sensitivity by several orders of magnitude. Fortunately, this critical problem has been addressed by the introduction of the TDI variables that were addressed in the previous chapter.

In this chapter, like Takahashi and Seto, the parameter estimation accuracy of low-mass compact binaries that are not necessarily monochromatic are considered. But unlike that work, the accuracy limits here are based on TDI variables and do not use the long-wavelength approximation. An in depth study of the role that the chirp-parameter, which is tantamount to a monotonic increase in the inspiral frequency, has in affecting the accuracies of all signal parameters is discussed. The effects of the Doppler-phase modulation is also studied to the same end. The study shows in what regions of the parameter space the effects of searching for the chirp parameter or the effect of Doppler-phase modulation are not negligible. This can be useful in simplifying prototypical studies for those sources for which these effects are small. On the other hand, parameter regions where a search for the chirp in a signal can hurt the accuracy of the other parameters estimates are identified. Moreover, it is demonstrated that the sensitivity sky-pattern of a network of TDI variables is very different from that of a network of Michelson variables. A similar difference exists in parameter accuracies achievable by these two types of networks. Since any realistic search will be conducted in a network of the former type, inferences based on a network of the latter type will be off.

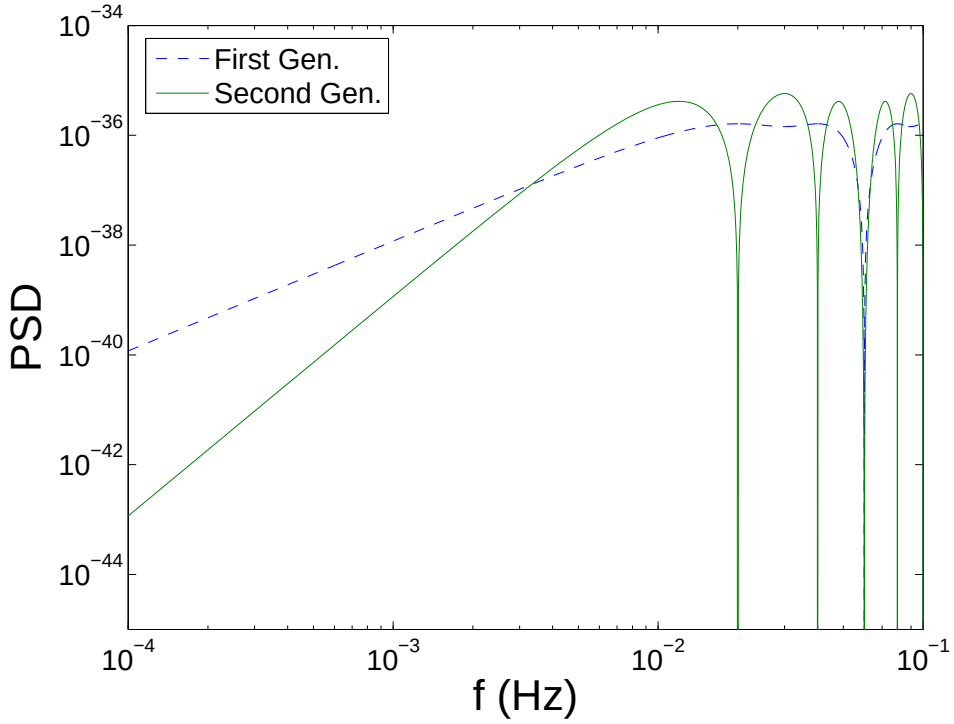

Figure 5.1: Plots of the first and second generation noise power-spectral densities (in units of Hz^{-1}).

5.1 Estimating signal parameters

In estimating the parameters of a signal, an observer has to confront the inherently noisy nature of the detector or receiver, which introduces a degree of randomness in the parameter measurements. Thus, an ensemble of multiple copies of the detector will return a distribution of parameter values that is affected by the characteristics of the detector noise. The spread in the distribution indicates the noise-limited accuracy of the detector.

Before continuing it is important to note that even in the absence of instrumental noise, a typical detector has physical limits on its measurement accuracy. In this context, there are two important time-scales that affect LISA's observations: The first arises from LISA's orbital baseline, the mean light-travel time for which is close to 1000s. Thus, the frequency

of a wave with wavelength equal to this distance is about 1mHz. The other scale arises from LISA's 5 million-km arm-length, which corresponds to a light-travel time of 16.67s. Thus, waves with frequencies that are odd-integral multiples of 0.03Hz will drive the two craft at the ends of an arm out of phase by 180 degrees. This makes LISA's sensitivity oscillatory at the higher end of its band (see Eqs. (5.1) and Fig. 5.1.)

To ascertain how large the noise-limited errors will be in the parameter values, the parameter values themselves are taken to be the maximum likelihood estimates (MLEs). Owing to noise, the MLEs, $\hat{\boldsymbol{\vartheta}}$, can deviate from the true values of the signal parameters and can influence the determination of other parameters. The magnitude of these deviations and influences can be quantified by the elements of the variance-covariance matrix, $\gamma^{mn} = \{\hat{\vartheta}^m, \hat{\vartheta}^n\}$ [25].

A relation between the γ^{mn} and the signal is available through the Cramer-Rao inequality, which dictates that

$$\| \boldsymbol{\gamma} \| \quad \geq \quad \| \boldsymbol{\Gamma} \|^{-1} \quad , \tag{5.1}$$

where $\boldsymbol{\Gamma}$ is the Fisher information matrix [13]:

$$\begin{aligned} \Gamma_{mn} &= \sum_{A=1}^{2} \left\langle \partial_m h^A(\boldsymbol{\vartheta}), \partial_n h^A(\boldsymbol{\vartheta}) \right\rangle_{(A)} \\ &\equiv \sum_{A=1}^{2} \frac{2}{P^A(f)} \int_0^T \left[\partial_m h^A(t;\boldsymbol{\vartheta})\right] \left[\partial_n h^A(t;\boldsymbol{\vartheta})\right] dt \,. \end{aligned} \tag{5.2}$$

In this chapter, the values of Γ_{mn} for signals from low-mass compact binaries in LISA data are determined. Therefore, $\Gamma_{mm}^{-1/2}$ gives the lower bound on $\Delta\vartheta^m$ (which is the expected random error in the MLE of ϑ^m). The two are equal in the limit of large SNR.

Since the amplitude and the initial phase are extrinsic parameters, one can analytically maximize the likelihood ratio with respect to them [49]. Here, it is assumed that this has been done. In such a case, the Fisher information matrix is six-dimensional. The errors in the phase and the amplitude can be derived in terms of the errors in the remaining six parameters as demonstrated, e.g., in Ref. [80]. This is the method used to compute the error in H. One can similarly infer the error in δ.

The errors in the sky-position angles will be presented in terms of the error in the measurement of the sky-position *solid angle*, defined as:

$$\Delta\Omega_S = 2\pi \left(\Delta\vartheta^5 \Delta\vartheta^6 - \langle \Delta\vartheta^5 \Delta\vartheta^6 \rangle \right) . \tag{5.3}$$

The error in the measurement of the source-orientation solid angle similarly defined:

$$\Delta\Omega_L = 2\pi \left(\Delta\vartheta^3 \Delta\vartheta^4 - \langle \Delta\vartheta^3 \Delta\vartheta^4 \rangle \right) \quad , \tag{5.4}$$

where the subscript L denotes the orbital angular momentum of the binary.

5.1.1 Scaling of parameter errors with SNR

Although the expressions above can be used to compute the error estimates for any parameter values, the results for specific values of some of these parameters are illustrated: Unless specified otherwise, an integration time of one year, an emission frequency of $\nu = 3$ mHz, and source orientation angles $\psi = \pi/3$ and $\iota = \pi/4$ are used. The emission frequency is chosen to be large enough so that the Doppler-phase modulations have a significant effect. The source orientation is chosen somewhat arbitrarily, except to ensure that the signal is not linearly polarized.

All the parameter estimates studied below are obtained by normalizing the estimates given in Eq. (5.2) by the network sensitivity, $\left[\sum_{A=1}^{2}\langle h^A,\ h^A\rangle_{(A)}\right]^{-1}$. Thus, the parameter-estimate values shown in the plots here are for a signal with an SNR of 1. To get an estimate for an arbitrary SNR, one simply multiplies the value shown in the plots by the SNR scale given in Table 5.1.

Table 5.1: The table lists how the errors in different parameters scale with the SNR. Since all the error plots are given for an SNR of unity, to assess the error for any other SNR one simply needs to multiply the plot value with the scale read from this table.

	$\Delta\Omega_S$	$\Delta\Omega_L$	$\Delta H/H$	$T\Delta\nu$	$T^2\Delta\dot{\nu}$
SNR scale	SNR^{-2}	SNR^{-2}	SNR^{-1}	SNR^{-1}	SNR^{-1}

An alternative way of understanding the parameter estimate normalization is through the Fisher information matrix. The idea here is to first divide the Fisher information matrix by the network template norm, $\sum_{A=1}^{2}\langle h^A,\ h^A\rangle_{(A)}$, as follows:

$$\widehat{\Gamma}_{mn} = \frac{\Gamma_{mn}}{\sum_{A=1}^{2}\langle h^A,\ h^A\rangle_{(A)}}\,. \tag{5.5}$$

One then obtains the normalized error estimates from the covariance matrix derived by inverting $\widehat{\Gamma}_{mn}$.

5.2 Doppler-phase modulation

When a template does not track the Doppler-phase modulation of a signal, over time it gets increasingly phase-incoherent relative to the latter. We quantify the degree of coherence between the two by the template mismatch:

$$m(\boldsymbol{\vartheta}, \boldsymbol{\vartheta}') = \frac{\sum_{A=1}^{2} \langle h^A(\boldsymbol{\vartheta}), h^A(\boldsymbol{\vartheta}') \rangle_{(A)}}{\sqrt{\sum_{B=1}^{2} \langle h^B(\boldsymbol{\vartheta}), h^B(\boldsymbol{\vartheta}) \rangle_{(B)} \ \sum_{C=1}^{2} \langle h^C(\boldsymbol{\vartheta}'), h^C(\boldsymbol{\vartheta}') \rangle_{(C)}}} \ , \tag{5.6}$$

where the value of the "template parameter" $\boldsymbol{\vartheta}'$ is, in general, different from that of the "signal parameter" $\boldsymbol{\vartheta}$. This quantity is inherantly different from the fitting factor. The fitting factor is a measure of the fraction loss in SNR that occurs when searching for a signal with templates from different regions of parameter space. With the fitting factor you maximize the quantity in eq. 5.6 over all the search parameter space. This allows for the possibility for a trigger to occur in a completly different region of parameter space than where the signal resides. The fitting factor is used understand how difficult it is for a signal to go undetected. In a heirachical search, once a detection has been made you then need to recover the source parameters. This will require laying a finer template bank in the region of parameter space that generated the original trigger. The template mismatch is a measure of the fraction drop in SNR that occurs when you try and dig out the actual source parameters with an imperfect template. The plot of the above function, with $h^A(\boldsymbol{\vartheta}')$ as the template without Doppler shifting and $h^A(\boldsymbol{\vartheta})$ as the signal with that shifting accounted for, is given in Fig. 5.2. As can be inferred from that figure, when the Doppler-phase modulation is not accounted for in the search templates, the SNR suffers an appreciable drop across the entire LISA band. It also exhibits large oscillations with a period that depends on LISA's orbital speed and that decreases linearly with increasing source frequency, as is characteristic of Doppler frequency shifting. It is important to note the locations of the nodes in the plot: The first minimum is at approximately f =1/2L, which occurs when the phases of a gravitational wave impinging along an arm are different by 180° at the two craft at the two ends of that arm.

In conclusion, since the effect of discounting Doppler-phase modulation is so marked on

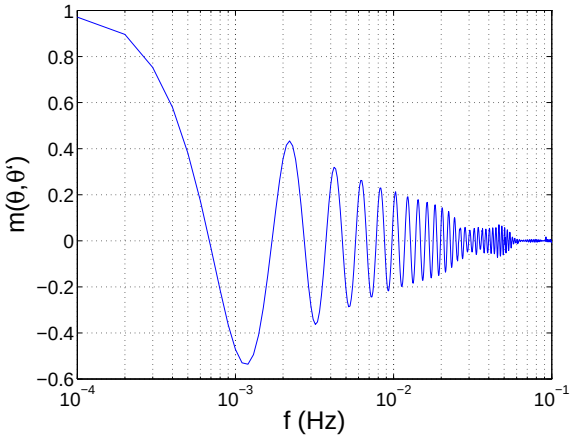

Figure 5.2: This is a plot of the template mismatch between two similar templates, one with the Doppler-phase modulation included and the other without it.

the SNR at any LISA frequency of interest, one must account for its effect on parameter estimation throughout the LISA band.

5.3 Effect of source frequency evolution

For binary compact object that are spiraling in fast enough, LISA will be able to measure their chirp mass and luminosity distance. Expression (4.18) shows that the amplitude, $H(\omega)$, of a signal from such an object depends jointly on r and $\mathcal{M}_c$. However, neither of these parameters affects any other part of a *monochromatic* (or $\dot{\nu}$) signal, as given in Eq. (4.26). Thus, one can not separately estimate either of them purely from the amplitude. Nevertheless, if a signal has an appreciable amount of inspiral or frequency evolution, defined in Eq. (4.30), then the measurement of $\dot{\nu}$, along with $H(\omega)$, determines both the chirp mass and the source distance.

In order to ascertain the individual masses of the binary, additional information is necessary. Traditional astronomical methods using optical or radio measurements can be used

to help identify the total mass of the binary system. However for many unknown sources or optically invisible sources this is not an option. In some cases where the binary orbit is noticeably eccentric, the accurate tracking of the emission frequency can provide information on the total mass of the system. This datum, together with the chirp mass, can be used to infer the individual masses of the system [15].

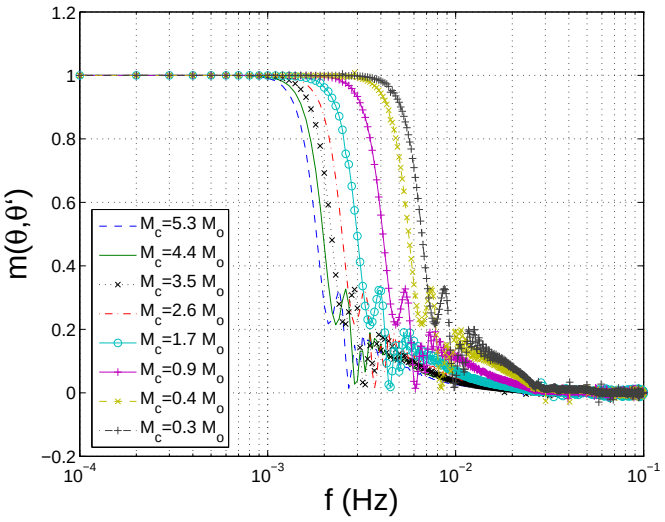

Figure 5.3: Template mismatches of low-mass compact binaries with a range of chirp masses are plotted as functions of frequency. Here the template mismatch is between two template families, one with a physical set of eight parameter values and another with the chirp (ϑ^0) set to zero, artificially, for all source frequencies. For the above plots, the sources are located on the ecliptic, with $\theta = \pi/2$, $\phi = \pi/2$, and their orientation is $\iota = \pi/4$, $\psi = \pi/3$. As a reference, an equal-mass binary, with $m_1 = m_2 \equiv 0.35\ M_\odot$ has $\mathcal{M}_c = 0.3\ M_\odot$. Template mismatches for equal-mass binaries with m =1,2,3,...6 $M_\odot$ can also be read from here.

Before analyzing the quantitative effects of a chirping waveform on parameter estimation, the role that a non-negligible $\dot{\nu}$ plays in searching for a signal is briefly studied. Specifically, the template mismatch defined in Eq. (5.6) to determine the fractional loss in the SNR while searching for a chirping source with monochromatic (i.e., $\dot{\nu} = 0$) templates is used. When subtracted from unity, the above function measures the fractional drop in the SNR owing to a parameter mismatch of $\Delta\boldsymbol{\vartheta} \equiv \boldsymbol{\vartheta} - \boldsymbol{\vartheta}'$. In Fig. 5.3, $m(\boldsymbol{\vartheta}, \boldsymbol{\vartheta}')$ with $\Delta\vartheta^m = 0$, for all

$m \neq 0$ is plotted; the "template parameter", ϑ'^0, is set to zero, while the "signal parameter", ϑ^0, is determined by Eq. (4.30) for any given emission frequency and chirp mass. For any given chirp mass, note how rapidly the SNR drops as a function of frequency. Also, since at any given frequency the chirping causes a smaller mismatch between the two template families for a smaller chirp mass, the SNR drop occurs at a higher frequency for a smaller chirp mass. Just like Fig. 5.2, this template mismatch too has oscillatory features. However, owing to the polynomial frequency behavior of $\dot{\nu}$, the oscillations here do not exhibit the linear decrease in the node-spacing found in Fig. 5.2.

Now the role of $\dot{\nu}$ in the estimation of the signal parameters is examined. As shown in Sec. 5.1, the expansion of the template parameter space in order to include another parameter affects the parameter estimation through the Fisher information matrix, which is a different construct than the template mismatch. Once a detection has been made using the most appropriate template, the error values presented here provide the standard deviation that should be expected for an ensemble of signal measurements made by LISA. However, one still needs to establish for what ranges of ω and $\mathcal{M}_c$ it is possible to measure a non-vanishing chirp in a signal. Outside these ranges, including $\dot{\omega}$ in ones template-parameter space can result in worse estimates for other parameters. A smaller parameter volume for estimating parameters is also desirable because it leads to a lesser computational burden: This is more so since the problem of detection in the presence of LISA's source confusion noise is intricately linked with the problem of parameter estimation.

Figure 5.4 shows that for binaries with $\mathcal{M}_c \simeq 5.3\ M_\odot$, the error in the estimation of its chirp is at least as large as the value of the chirp itself (for an SNR of 10) for $\nu \lesssim 2.5$ mHz. As shown in Fig. 5.5, this is very close to the frequency where the inclusion of the chirp starts

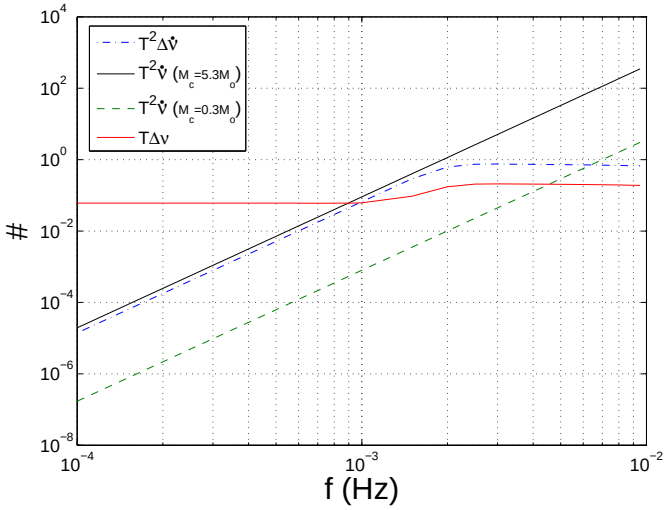

Figure 5.4: These plots illustrate the values (in number of cycles) of the chirp parameter for two values of the chirp mass ($\mathcal{M}_c = 0.3M_\odot$ and $5.3M_\odot$), along with the errors in determining the chirp and frequency for an SNR of 10. All plots are for an observation period of $T =$ 1 year. Note how for the larger chirp mass the error in determining the chirp remains comparable to the value of the chirp itself up to about 1.5mHz, before improving at higher frequencies.

hurting the estimation of the frequency. On its own merit, this would argue for the dropping of the $\dot{\nu}$ parameter from the search templates (i.e., setting $\vartheta^0 = 0$) for $\mathcal{M}_c \gtrsim 5.3\ M_\odot$ and $\nu \lesssim 2.5$ mHz. However, the template mismatch plot shows that doing so can vastly reduce the probability for detecting the correct signals with $\nu \gtrsim 1$ mHz. Therefore a region in the parameter space where entertaining the prospects of a proper detection requires taking a beating in estimating the source parameters has been identified. This adds an additional layer of challenge in the quest for cleaning what is deemed as the resolvable part of the confusion noise spectrum.

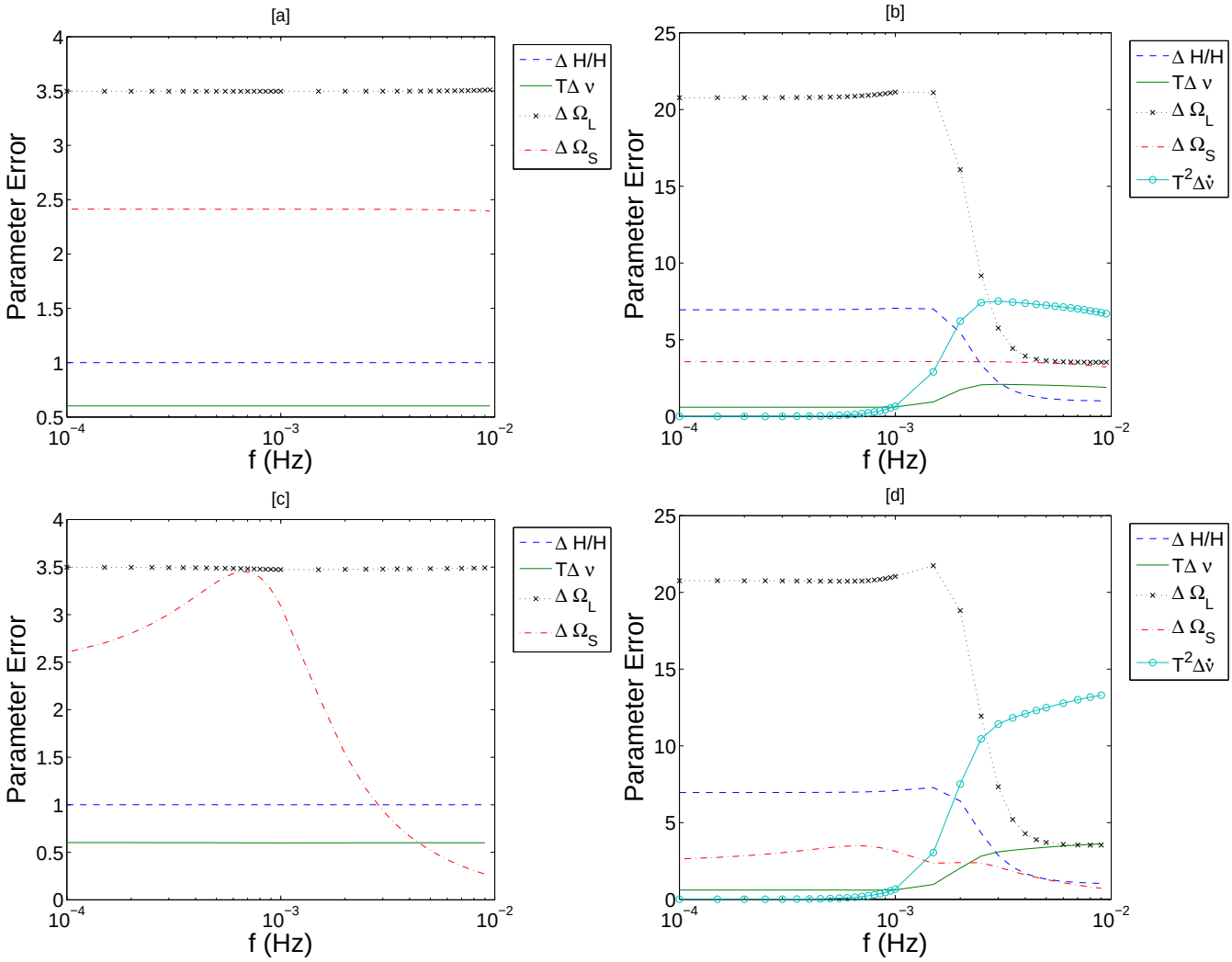

Figure 5.5: These figures show how the errors in the different signal parameters behave as a function of the source frequency for the following four cases (a) with no Doppler-phase modulation and no chirp, (b) with chirp only, but no Doppler-phase modulation, (c) with Doppler-phase modulation, but no chirp, and (d) with both Doppler-phase modulation and chirp included. The sky-position assumed is: $\theta = \pi/2$, $\phi = \pi/2$; also, $\iota = \pi/4$, $\psi = \pi/3$.

5.4 Frequency Dependence of parameter errors

Imagine a one-parameter family of sources, which have everything else identical, except for the emission frequency, ν. The parameter-estimation errors for such a family are not invariant across LISA's bandwidth. This is because both the Doppler-frequency shifting and the frequency evolution increase with ν. Additionally, the sensitivity of LISA itself varies

across the band, as shown in Fig. 5.6. For nearly monochromatic signals, the latter effect gets essentially factored away when considering *SNR-normalized* estimates. Figure 5.5 shows the frequency dependence of the parameter errors, normalized for an SNR of unity, for four different cases: Case (a) depicts these errors when a signal has no Doppler-phase modulation, and no frequency evolution (where the latter is unphysical). Case (b) presents the same when there is frequency evolution natural to the binary, but no Doppler-phase modulation (such as if LISA were at the SSB). Case (c) includes the effect of Doppler phase modulation but has the frequency evolution (artificially) turned off. Finally, plot (d) has effects from both the Doppler phase modulation and the frequency evolution.

It is interesting to note that in Fig. 5.5a the error in the estimate of each of the parameters is essentially independent of the emission frequency. The primary contribution to the frequency dependence of the Fisher information matrix in Eq. (5.2) arises from LISA's own sensitivity reflected in its noise PSD. The elements of this matrix depend on $P^A(f)$, which is the same for both $A = 1, 2$. However, when the parameter errors are obtained by scaling this matrix by the template norm, as described in Eq. (5.5), the factor of $P^A(f)$ for near-monochromatic signals gets canceled away, thus rendering the plots in Fig. 5.5 mostly flat.

Next is to consider the effect of Doppler-phase modulation on the parameter estimation accuracy. Comparing Figs. 5.5a and 5.5c shows that the errors in all parameters are mostly unaffected except for the error in sky-position. That error actually worsens with frequency in the 0.1-1 mHz band, before rapidly improving at higher frequencies. This is because at wavelengths longer than 1 AU, the Doppler-phase modulation acts like noise on the sky-position dependent σ_i^A term in the phase of the signal in Eq. (4.35), thus, affecting

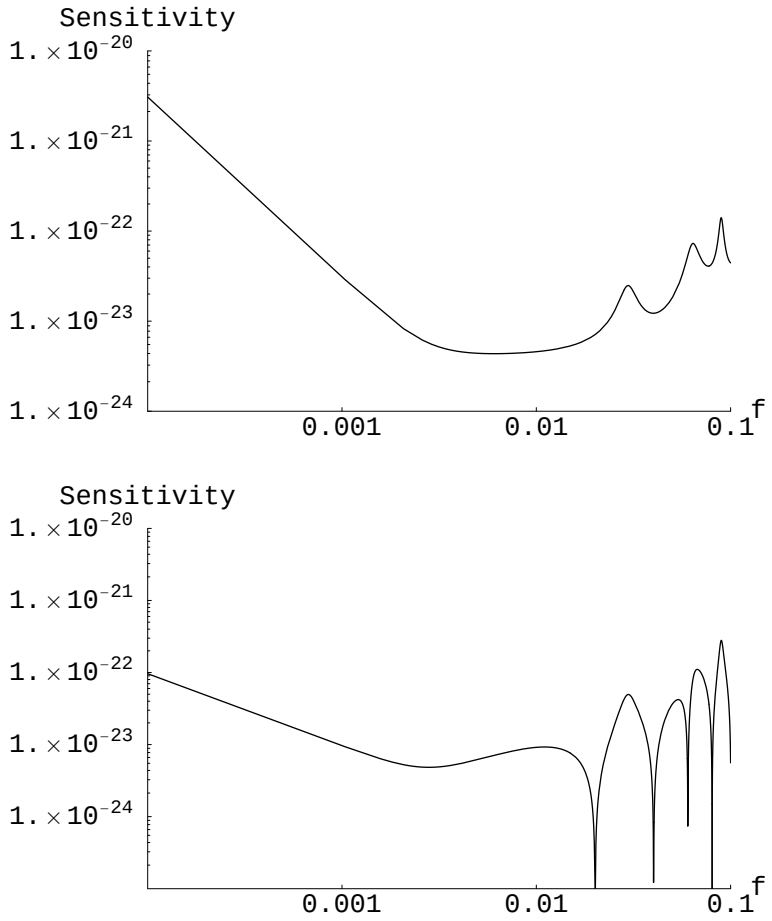

Figure 5.6: These are plots for the sensitivity of LISA as a function of the frequency (in Hz) for the first and second generation TDIs, respectively.

sky-position estimation. On the other hand, at high frequencies, it does a better job at resolving a binary's direction than do the beam-pattern-function induced modulations of the amplitude and the phase.

The effect of the chirp can be understood by comparing Figs. 5.5c and 5.5d (or, alternatively, Figs. 5.5a and 5.5b): It worsens the estimation of the amplitude and source orientation at low frequencies, i.e., for $\nu \lesssim 1.5$ mHz. It also reduces the accuracy of its own estimate and that of the source frequency at high frequencies, i.e., for $\nu \gtrsim 1.5$ mHz. Here, one may wonder why at frequencies below 1.5 mHz, the chirp's inclusion ruins the determi-

nation of the source orientation, but not the frequency. The answer is that during the course of a year one integrates through a very large number of cycles of a signal, which averages out the noise in the estimation of the frequency arising from the chirp. The same would be true about the orientation if one were to integrate for a large number of LISA orbits (or years). Interestingly, at frequencies higher than 2 mHz, while the chirp leaves the estimation of the source orientation unaffected, it hurts the estimation of the source frequency. This is because starting at around a milli-Hertz, the chirp acts as a source of noise in the determination of the frequency.

In summary, the general behavior of the SNR normalized parameter-estimation errors as functions of ν can be understood as follows. Primarily, there are two competing parts of the signal that provide information about the source: The amplitude modulation and the phase modulation. The amplitude is modulated differently throughout the course of a year depending on the source location and orientation. The amplitude modulations provide information about these two source parameters in a manner that the SNR-normalized error in them remains invariant across LISA's band (as can be inferred from Fig. 5.5 a). Whereas tracking the phase provides information about the source location, source frequency, frequency evolution and, hence, the chirp mass. The main difference between the two modulations is that the phase modulation is highly dependent on the emission frequency of the source, whereas amplitude modulation is not. Since the amplitude modulation is less sensitive to the emission frequency, its contribution to any parameter estimate is relatively unchanged over LISA's band. Contrastingly, phase modulation provides less information at low emission frequencies. This is due to the relatively fewer cycles one obtains in a given observation time for low frequencies compared to higher ones. For the frequency range that LISA is

projected to observe, this translates into roughly a factor of 10^3 less cycles that would be obtained for the smallest observable frequencies with respect to the largest ones. However, as the frequency increases the contribution from the phase modulation eventually surpasses that due to the amplitude modulations.

5.4.1 Excluding frequency evolution from the templates

The preceding discussion shows that at any given LISA frequency *searching for* the frequency evolution of a binary affects the determination of one or the other parameter, except the sky position. For a source with an initial frequency, $\nu \gtrsim 1.5$ mHz, its inspiral hurts the error in the estimation of ν by a factor of over 3.5 relative to that of sources with $\nu \lesssim 1$ mHz. It has been verified that increasing the integration time to 2 years reduces this relative error factor to about 2, confirming what is shown in Ref. [67]. This reduction may be insufficient for the resolution of the galactic binary confusion noise. This makes a case for a mission lifetime that is longer than 2 years. Otherwise, the only other option available for maintaining the parameter accuracies is to exclude the chirp parameter from the search templates, since doing so improves the SNR-normalized parameter estimates. This, however, has different consequences for the parameter accuracies of binaries with different chirp masses.

The template mismatch plots in Fig. 5.3 show that for the lowest astrophysically interesting chirp mass, $\mathcal{M}_c \simeq 0.3 M_\odot$, such an exclusion has little effect on the SNR until about 4 mHz, which happens to be just below the high-frequency-end of the confusion noise arising from extreme mass-ratio inspiral (EMRI) sources. The effect on the estimates of the other parameters is a systematic bias by an amount that depends linearly on $T^2\dot{\nu}$ [81], which is

about 0.1 (cycles) for $T = 1$year and at $\nu = 4$ mHz. While this introduces a negligible bias in the estimates of all parameters, it has the advantage of reducing the level of the random estimation errors to the same level as that shown in Fig. 5.5a. At frequencies as high as even 6 mHz, the SNR drop due to such an exclusion would be more than 30%, thus, jeopardizing both the prospects of an accurate detection and the adequate parameter resolution required for cleaning the WD-WD confusion noise.

On the other hand, note that for a binary with $\mathcal{M}_c \geq 5.3 M_\odot$, such an exclusion causes the same fractional drop in the SNR at frequencies as low as 1.5 mHz, which is where the parameter estimates start getting affected (see Fig. 5.5b or 5.5d). Thus, for binaries with $\mathcal{M}_c \geq 5.3 M_\odot$, turning off the chirp parameter in the search templates is unlikely to improve the parameter estimation for $\nu \geq 1.5$ mHz. Among the sources most affected from this "chirp search" problem are galactic low-mass binaries containing a black hole.

5.5 Sky-position dependence of parameter errors

In this section, the behavior of the parameter errors as functions of the direction to a binary is addressed. Illustrated below is the sky-position dependence of the SNR-normalized parameter errors for the same source polarization state and frequency as the one chosen in Sec. 5.4 for the frequency plots in Fig. 5.5. The source frequency choice, viz., $\nu = 3$ mHz is interesting for multiple reasons: As observed above, it is close to the high-frequency-end of the unresolvable WD-WD confusion noise. Figure 5.5d shows that it is also in the region of transition in the behavior of the parameter errors as functions of frequency. All the same, it is not too small for the Doppler-phase modulation to have a negligible effect on the

parameter accuracies.

When studying these errors as functions of frequency in Fig. 5.5, the sky position of the source remains fixed. For this reason, while computing the SNR-normalized errors, the possibility that the SNR may vary with the sky position was not a concern. This possibility is addressed below. The dependence of the SNR on the polarization state can be studied similarly.

5.5.1 Sky-position dependence of the SNR

The SNR normalization performed on the Fisher information matrix in Eq. 5.5 is useful in that the parameter errors computed from such a matrix can be easily scaled for a signal of any SNR using the scaling factors given in Table 5.1. In this context, it is important to note that the SNR of a standard candle is not uniform across the sky owing to the non-uniform sensitivity of LISA to different sky positions. This quantity is plotted for four different cases in Figs. 5.7 and 5.8, where the latter set is the 3D rendition of the former set. These plots, called "sky plots", are normalized so that the maximum value attained in each case is unity. These four cases are identical to those considered for studying the frequency dependence of parameter errors in Figs. 5.5. As in that study, here too Fig. 5.7a (or, equivalently, Fig. 5.8a) is for an artificial signal, with $\dot{\nu}$ set to zero), when compared with Fig. 5.7b, it allows one to graphically assess how useful or detrimental the presence of frequency evolution is in detecting a signal. Similarly for Fig. 5.7c, when compared with Fig. 5.7d. Note that as per the definitions of cases (a) and (b), Figs. 5.7a and 5.7b have the Doppler-phase modulation turned off.

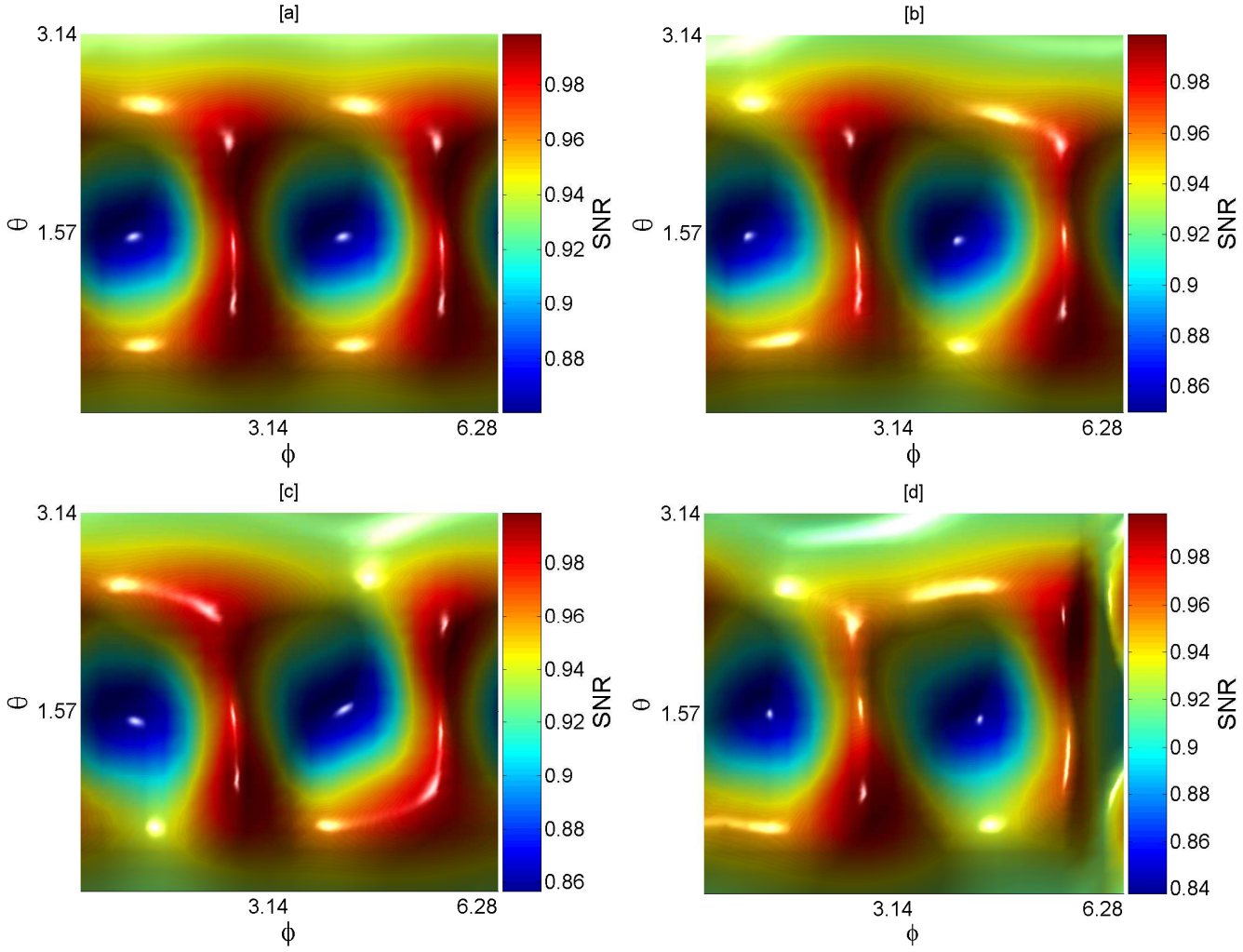

Figure 5.7: These are plots of the template-norm-squared for the same four cases of LISA motion and source frequency evolution considered in Fig. 5.5. The plot for each case is normalized to have a maximum value of unity. Both θ and ϕ are given in radians, with the origin, $(0, 0)$, in the bottom left corner of each plot. Note that this is the first of a series of *colored* sky-plots; gresyscale prints of these plots can give a misleading impression of the color values.

5.5.2 Explaining the sky-position dependence

Given that LISA's orbital motion is confined to a nearly circular orbit on the ecliptic, one may expect the SNR plots to be axisymmetric. This is indeed the case for the network comprising the two Michelson variables, as can be seen in Fig. 5.9, where the focus is limited to their geometric sensitivity and momentarily ignore the fact that they will be severely

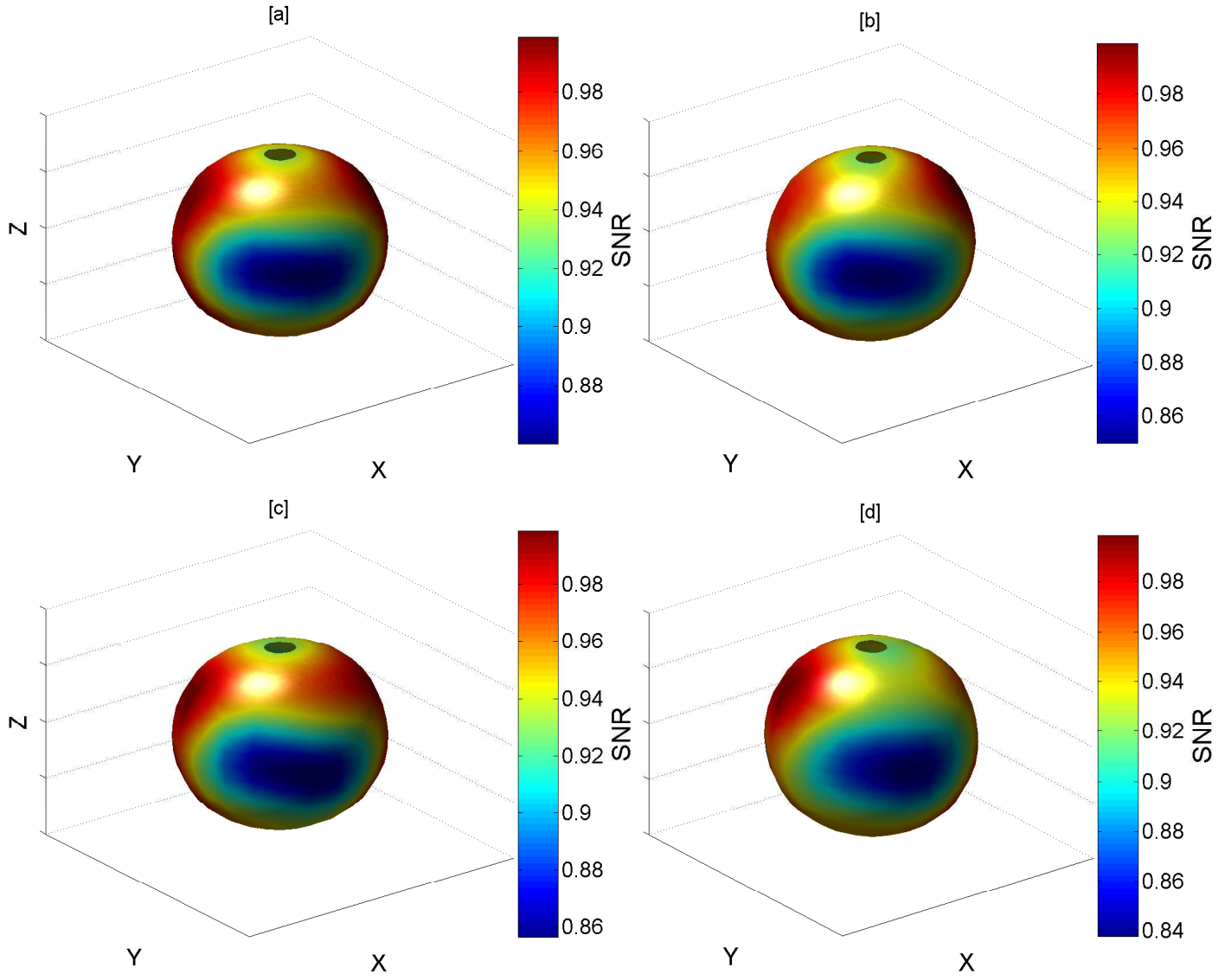

Figure 5.8: Spherical renditions of the template-norm-squared plots shown in Fig. 5.7.

limited by the laser frequency-fluctuation noise. Figures 5.9a and 5.9b reveal that although the SNR for neither of the Michelson variables is axisymmetric, their quadrature combination is so. For comparison, the analogous plots for the $\bar{A}$ and $\bar{E}$ TDI variables in Figs. 5.10 are presented. All these plots are normalized relative to the maximum value attained among the template norms of the individual Michelson and $\bar{A}$-$\bar{E}$ variables.

Interestingly, however, the SNRs for the $\bar{A}$ and $\bar{E}$ TDI variables, plotted in Fig. 5.10,

are more dumbbell-shaped than axisymmetric, where the pattern depends on the initial orientation of LISA. Also, since there is a slight difference between the overall sensitivities of the two variables, their quadrature combination is more of an inflated version of the $\bar{A}$ variable. As one would expect, it also resembles well the SNR of Fig. 5.8a.

Figure 5.11 illustrates the sensitivity of a single arm to all sky positions. What is evident from this figure is its striking similarity to the $\bar{A}$ TDI data combination. The features of this plot are well understood geometrically. For a single arm, spinning and orbiting the SSB, there exists a periodicity of π radians under axial rotations. However, this figure shows that there are two distinct and orthogonal directions, and their antipodes, that stand out. These locations correspond to the global maxima and minima in the sensitivity of this arm to impinging gravitational waves. These very same extrema are present in the SNR plots as well. To understand the origin of these global extrema, the orbital motion of LISA's centroid is not as important as the spin of LISA's individual arms. Therefore, consider how a single arm spins during the course of a year. Let it begin in an orientation that is parallel to the ecliptic plane. In this orientation, a low-frequency source that is in a direction perpendicular to the arm will create the maximum strain in that arm. Conversely, when such a source is in a direction along the arm, the strain caused in that arm is zero. Let us call these directions 1 and 2, respectively. With the exception of their antipodes, there is no other orbital position that will attain such extrema in the sensitivity for that particular arm during its orbit. As the arm rotates out of the ecliptic plane, the sensitivity to direction 1 will begin to degrade. However, because direction 1 will never be parallel to the same arm, it will never attain the same minima that direction 2 attained initially and, vice versa. Therefore, the orbital position where these global extrema are obtained is forever imprinted upon the integrated

results regardless of the duration of observation.

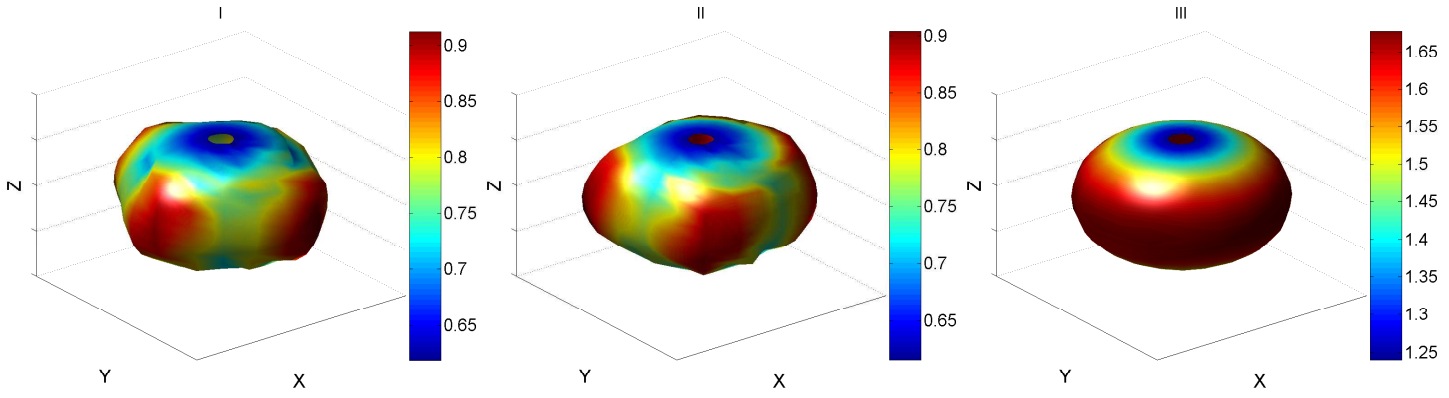

Figure 5.9: The template-norm-squared for the Michelson variables as functions of sky position: for Michelson variable I as a function of sky position (left), II. for Michelson variable II as a function of sky position (center), III. for the network comprising both Michelson variables (right). All plots are presented for the following source parameters: $\{\iota = \pi/4, \psi = \pi/3, \nu = 3 \text{ mHz}\}$

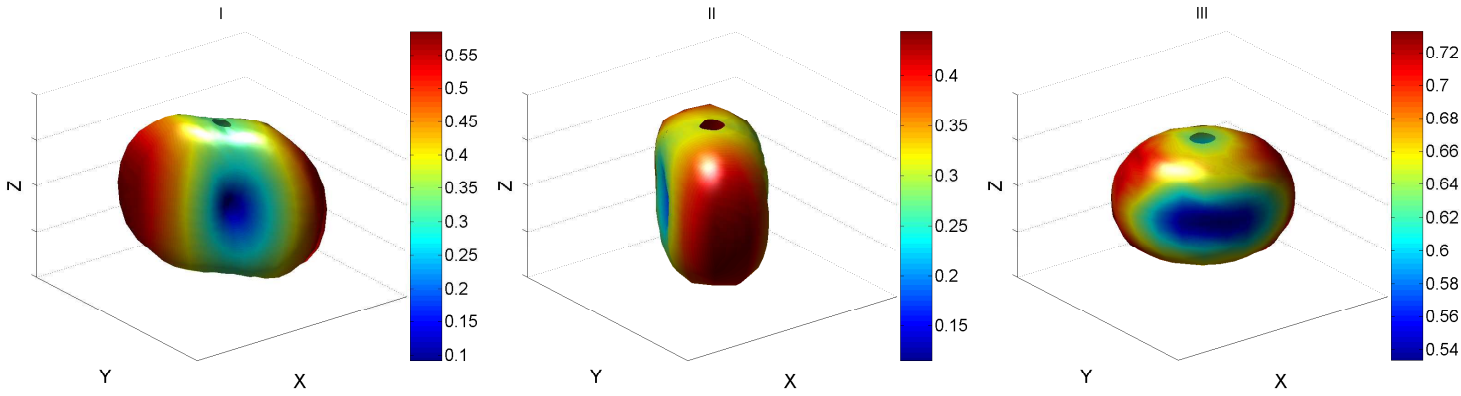

Figure 5.10: The template-norm-squared for the $\bar{A}$ and $\bar{E}$ TDI variables as functions of sky position: I. for the $\bar{A}$ TDI data combination (left), II. for the $\bar{E}$ TDI data combination as a function of sky position (center), and III. for the network comprising both $\bar{A}$ and $\bar{E}$ TDI data combinations. All plots are presented for the following source parameters: $\{\iota = \pi/4, \psi = \pi/3, \nu = 3 \text{ mHz}\}$.

5.5.3 Parameter errors

The parameter errors are plotted as functions of sky position in Figs. 5.12, 5.13, and 5.14 for the same source polarization state and frequency as described earlier in this section. Note

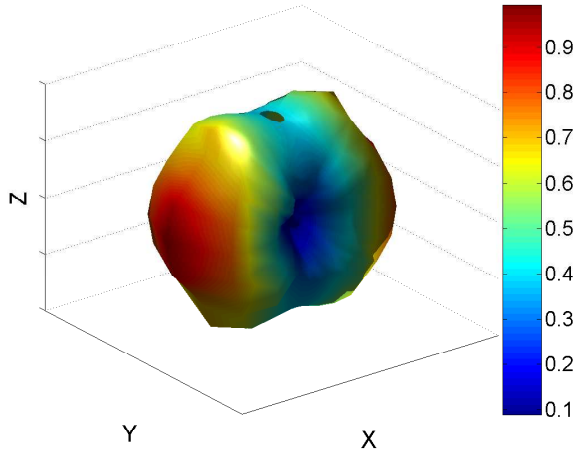

Figure 5.11: A single arm's template-norm-squared. All plots are presented using the following parameters: $\{\iota = \pi/4, \psi = \pi/3, \nu = 3 \text{ mHz}\}$.

that these parameter-error sky plots are presented for the $\bar{A}\bar{E}\bar{T}$ pseudo-detector network. Altering ν, the polarization state, or the pseudo-detector network will, in general, change the details found in these plots. However, certain qualitative aspects, discussed below, will remain unaffected.

While all four cases (i.e., (a)-(d)) are plotted for sky-position and frequency errors in Figs. 5.12 and 5.13, respectively, only the full case (i.e., case (d)) is plotted for the remaining parameters in Fig. 5.14. This is because the plot for each case of these remaining parameters strongly resembles the frequency-error sky plot of the corresponding case in Fig. 5.13. Indeed, a quick examination of all the error plots reveals that they can be divided into two sets based on their apparent symmetry: (1) those for the sky-position and (2) those for the rest of the parameters. The first set displays a *strong* axisymmetry (i.e., symmetry with respect to translations along the ϕ axis) that is missing in the other set. The reason behind this divide is that the Fisher information matrix and, therefore, the parameter covariance matrix, is predominantly block diagonal, with two blocks. The first block comprises just the

sky-position (θ, ϕ) variance-covariance and the second one comprises the variance-covariance of the rest of the parameters. The elements outside of these two blocks are not all zeros, but are much smaller than the elements within the blocks. Consequently, any error in a parameter in one set influences that in another parameter from the same set much more strongly than in the other set. This explains why the patterns in each case of the second set are so similar among all parameters within that set, as is manifest in Fig. 5.14. Also, the reason why the sky-position error plots are predominantly axisymmetric while the other ones are not is because while the latter are affected by the beam-pattern functions alone, the former are affected by them as well as their parameter derivatives. It is worth noting that the deviation from axisymmetry is still apparent in Figs. 5.12, however, this effect is significantly reduced with respect to the other parameters.

There is an alternative way of understanding the three "unphysical" cases (i.e., cases (a)-(c)) studied in Figs. 5.12 and 5.14. Starting with the last of these, case (c), note that it is identical to the physical case where the chirping is negligible. This is indeed the case when the chirp mass is as low as $0.3M_{\odot}$. As seen in Fig. 5.3, for such a case, filtering the data with chirp-less templates causes negligible SNR loss. Thus, the case (c) plots in these figures indicate the expected random errors in such a search.

Case (b) resembles the physical case where the Doppler-phase modulation is negligible, which occurs when the source frequency is below a milli-Hertz (barring the slight ruining of the sky-position estimates). Since the chirp rate was fixed in this plot, to compensate for lowering the frequency to below 1 mHz one must increase the chirp mass, which affects the signal amplitude but not the SNR-normalized error shown here. Thus, case (b) is the expected error plot for all sources that have frequencies less than about 1 mHz but chirp

masses commensurately larger than $5.3M_\odot$ (such that $\mathcal{M}_c^{5/3}\omega^{11/3} = \text{constant}$). Comparing the plots for cases (b) and (d) then shows that the SNR-normalized error tends to increase at low frequencies, more so at the poles than near the ecliptic.

Finally, case (a) represents the physical case where $\nu < 1$ mHz and $\mathcal{M}_c$ is very small, such that both Doppler-phase modulation and source chirping are negligible. (Note that the sky-position error is almost constant in the LISA band below 1 mHz (cf. Fig. 5.5).) However as Fig. 5.2 illustrates, this will not occur in the LISA band.

For parameter errors for eccentric sources please see the appendix.

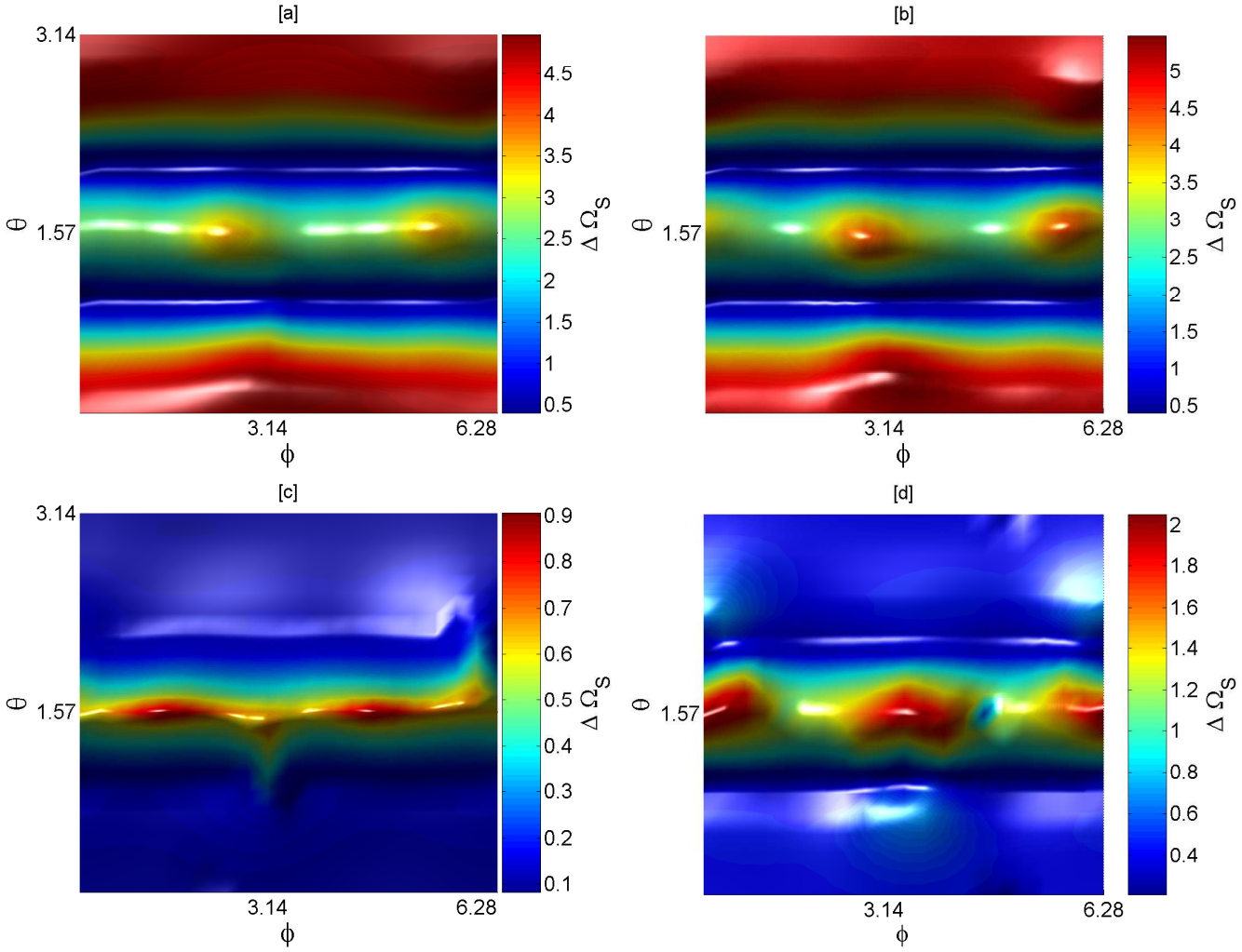

Figure 5.12: These are plots of the errors associated with determining the sky position measured in terms of a solid angle spread $\Delta\Omega_S$. The four plots are for the four cases described in Fig. 5.5. All plots are made for the following source parameters: $\{\iota = \pi/4, \psi = \pi/3, \nu = 3 \text{ mHz}\}$.

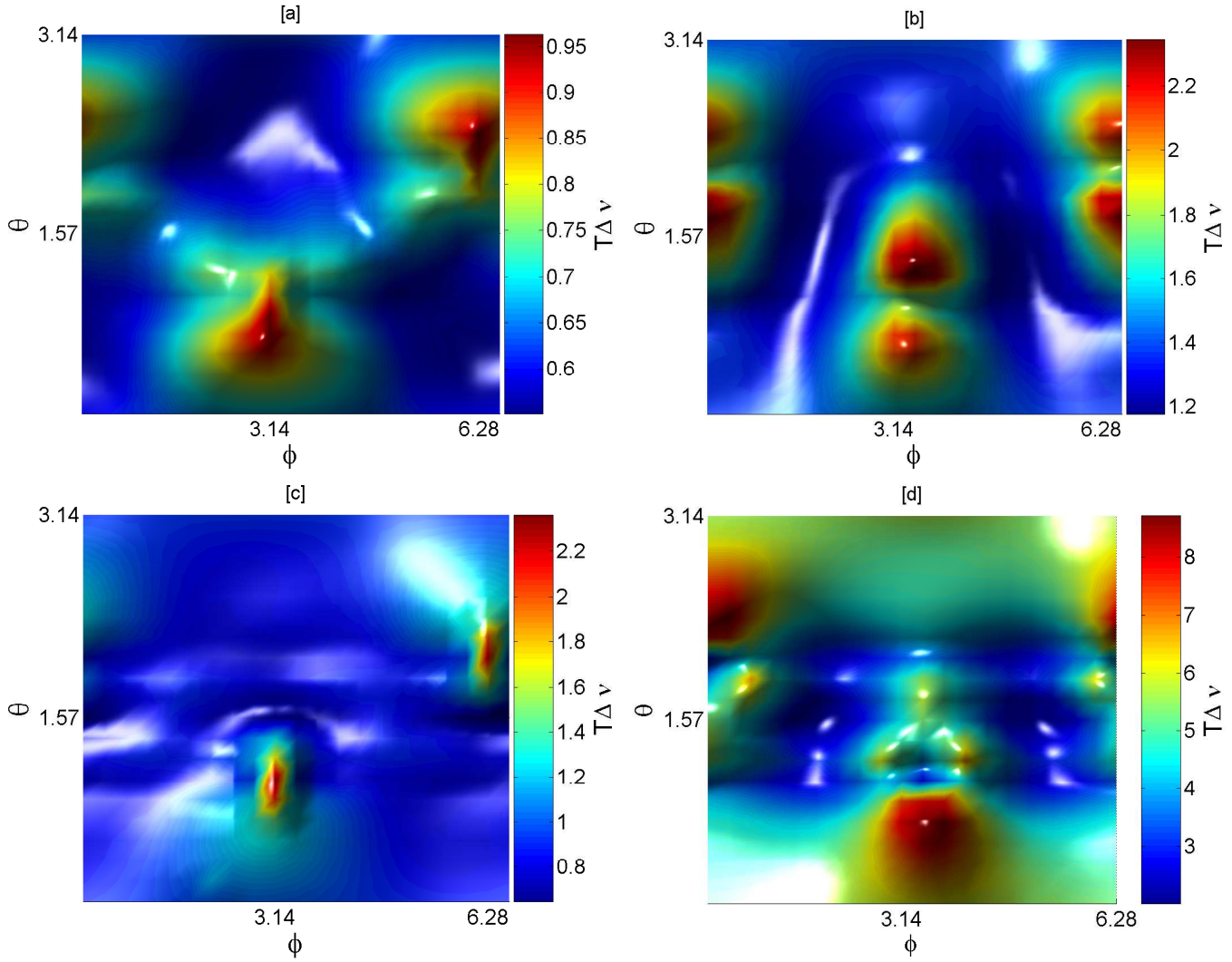

Figure 5.13: These are plots of the errors associated with determining the dimensionless emission frequency parameter $T\Delta\nu$. The four plots are for the four cases described in Fig. 5.5. All plots are made for the following source parameters: $\{\iota = \pi/4, \psi = \pi/3, \nu = 3 \text{ mHz}\}$.

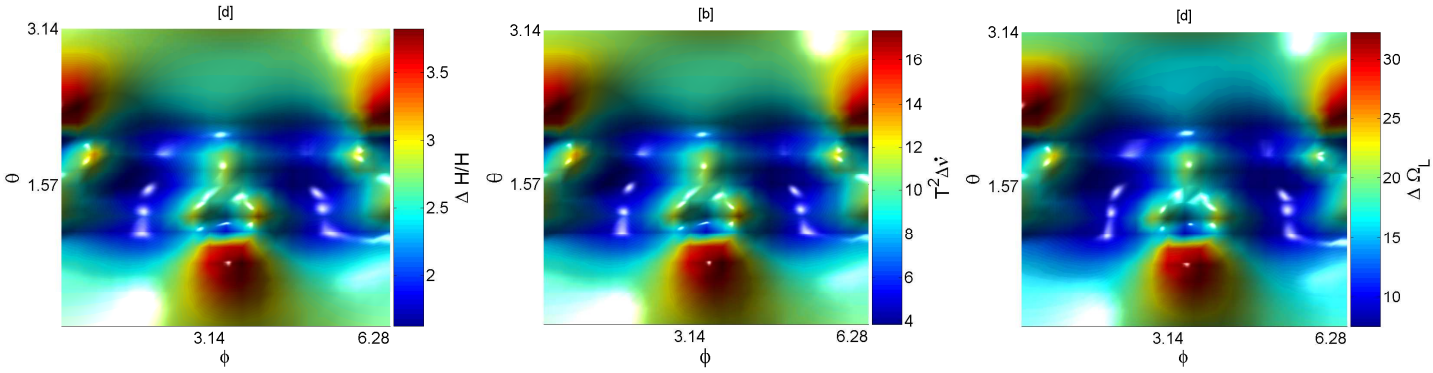

Figure 5.14: Plots of the errors associated with the remaining parameters: $\Delta H/H$, $T^2\Delta\dot{\nu}$, and $\Delta\Omega_L$. They all correspond to case (d) described in Fig. 5.5. Both Doppler-phase modulation and frequency evolution are included here. All plots are made for the following source parameters: $\{\iota = \pi/4, \psi = \pi/3, \nu = 3 \text{ mHz}\}$.

Chapter 6

LIGO Instrument Characterization and Coherent Inspiral Searches

The search for gravitational waves with LIGO is markedly different than that with LISA. Unlike LISA, LIGO has no guaranteed sources and the predicted event rates are significantly smaller than those for LISA as a result. The studies presented in this chapter will focus on searching for binary neutron star (BNS) inspirals. At LIGO's current sensitivity, population model studies have suggested the event rates for these systems range from $3^{-4} - 2.5^{-1}$ per year [92]. The improvements that will come with advanced LIGO [94, 93] increase the overall sensitivity of the detectors to impinging gravitational waves. The increased sensitivity will elevate the BSN event rates for advanced LIGO to the range of 2-1300 per year [92, 95, 94]. Considering that these signals last at most a few minutes, it is still possible to have a signal go undetected within a year's worth of data. This fact motivates the development of ever evolving search algorithms as well as monitoring tools so as to maximize the chances of recovering the first GW signal.

6.1 GainMon

6.1.1 What is GainMon?

LIGO utilizes one of the most advanced Nd:YAG laser systems in the world to continuously search for GW. In order to attain the desired sensitivities for LIGO, a suite of monitoring tools is necessary and it continues to be improved. All the monitoring tools relay current information about the state of the detector to control room operators or scientific monitors (scimons). The ultimate goal of any of these tools is to maintain the highest duty cycle for the detector. If the detector drops out of what is called "science mode" then the data collected at that time is no longer valid data to search for GW. These tools provide operators and scimons with insights that may allow them proactively prevent future detector related problems.

GainMon is a monitoring tool that allows operators and scimons to determine if the laser system drifts away from optimal alignment. Seeing that the optimal alignment is dynamic depending on environmental conditions, the information provided by GainMon to control room operators can be used to either maintain the current sensitivity during small seismic related events or possibly used to slightly increase the detector sensitivity in some circumstances. GainMon monitors the 4km and 2km Fabry-Perot that comprise the three LIGO detectors for drifts in the unity gain frequency. These drifts indicate that the laser alignment has been altered by some mechanism and therefore the operators may need to adjust the alignment manually to compensate. Ideally, the UGF should remain constant over time. However, the photodetectors can saturate if the laser drifts to far towards the center of the optics. As the laser drift towards the center of the optics, a subsequent rise

in the UGF would occur. The sudden rise in the UGF would indicate to the operator that the photodetectors may soon become saturated. The manual alignment of the laser at this point could prevent the detectors from dropping out of science mode. On the other hand if the laser alignment drifts to far towards the edge of the optics, this would cause an increase in the backscattered light. GainMon would then register a relative drop in the UGF, which would indicate to the operator that the lasers need to be recentered on the optics. The feedback that GainMon provides is in real time as it reports 1 second trends of the current UGF. This allows operators to make crucial adjustments that aid in maintaining an overall higher duty cycle.

This tool also serves a secondary function as a backup for SenseMonitor. SenseMonitor also provides 1 second trends of the detector's current range sensitivities. If the distance that is currently available to the detector varies, it would show simultaneously in both SenseMonitor and GainMon. Considering that both SenseMonitor and GainMon function in a very similar fashion, if SenseMonitor ceases to function for any period of time due to some hardware failures then the operators can use GainMon as a secondary monitor for the detectors current range sensitivity.

6.1.2 How GainMon Works

The UGF is the frequency at which the open loop gain (OLG) function, $G(F)$, is unity. Owing to the fact that the OLG function changes linearly with time, determining the OLG function at the start of a given science run will determine the OLG function and subsequently the UGF for all later times. The OLG at any later time is directly proportional to the OLG

at $t = 0$ which is written as:

$$G(f,t) = \alpha(t)\beta(t)G(f,t=0) \tag{6.1}$$

where $\alpha(t)$ and $\beta(t)$ are calibration factors that must be monitored in real time for GainMon to function effectively. Contrastingly, the open loop gain at any instant of time can also be written in terms of three response functions as follows:

$$G(f) = C(f)A(f)D(f) \tag{6.2}$$

where $C(f)$ is the sensing function, $A(f)$ is the actuation function and $D(f)$ is the digital filter function. The servo loop for LIGO is depicted in fig. 6.1 and it illustrates the roles of these three functions. The sensing function monitors the response of LIGO's optical cavities, the actuation function monitors the mechanical response of the suspended test masses, and the digital filter function describes how the digital filters are incorporated into the loop [82]. Each one of these function can vary independently of one another and must be monitored separately. The evolution of the sensing function is entirely defined by the $\alpha(t)$ calibration factor and the evolution of the digital filter response is entirely defined by the $\beta(t)$ calibration factor as shown in eqs. 6.3 and 6.4.

$$C(f,t) = \alpha(t)C(f,t=0) \tag{6.3}$$

$$D(f,t) = \beta(t)D(f,t=0) \tag{6.4}$$

GainMon monitors these individual response functions for any changes and then calculates the OLG in 1 minute intervals. Considering that the interferometer calibrations are assumed to change in a linear fashion, GainMon interpolates the OLG to the frequency

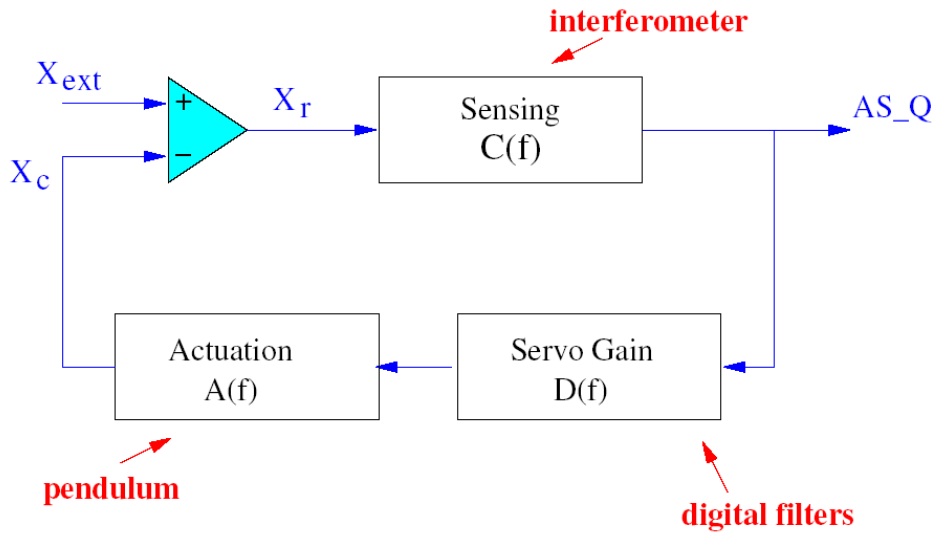

Figure 6.1: The servo loop for the three LIGO detectors [82].

where it is unity and reports this in 1 minute trends. A secondary output by GainMon is the actual α and β factors. GainMon also reports the amplitude of the injected calibration lines, which are used to track the interferometers response to possible signals [84]. The output from GainMon is used to trend the UGF as well as the various calibration factors for LIGO operators to monitor in the two LIGO control rooms. The trends produced by GainMon were incorporated into the LIGO Figures of Merit (FOM) at the start of Science Run 5 in November 2005 and will continue to be used as an effective monitoring tool for all future science runs.

6.2 LIGO Coherent Search

The ultimate goal of any interferometer detector is to detect the first GW signal. This daunting task is hindered by the overall sensitivity of the individual detectors used in searching for these elusive GW signals. The inspiral pipeline [85, 90, 91] uses an algorithm developed to

identify chirp waveforms [86] in interferometric detectors. Incorporating the coherent code into the full inspiral search pipeline is the driving force behind the remainder of this chapter. The coherent search is a multi-detector search algorithm that combines the output from as many as four interferometers in an effort to obtain a larger sensitivity. The larger sensitivity increases the likelihood of detecting the first GW signal. The coherent search pipeline for LIGO was originally developed by Shawn Seader [6] and Sukanta Bose but the completion, testing and incorporation into the real time LIGO search pipeline was never realized until recently.

6.2.1 Coherent Search Statistic

The coherent code can currently combine data from up to four different interferometers (ifos) in a variety of fashions to obtain a single network statistic. The network statistic is derived in a similar fashion as the network statistic for LISA in section 4.2.2. One main difference between these two statistics is the normalization constat g_A which is now as follows:

$$g_A = \frac{4}{3} f_{s(A)}^{4/3} \int_{f_{s(A)}}^{\infty} \frac{df}{f^{7/3} P_{h(A)}(f)}, \tag{6.5}$$

where $f_{s(A)}$ is the seismic cut-off frequency and $P_{h(A)}$ is the noise PSD of the Ath detector. In this instance, the normalization constant is chosen such that

$$\langle S^A, S^A \rangle_A = 2 \tag{6.6}$$

as opposed to unity as was the case for LISA. Another main departure from the statistic developed for LISA is that the beam pattern functions for inspiral signals in the LIGO band are constant. Admittedly, the constancy of the beam pattern functions simplifies the

detection problems. However, the signal phase, which will be denoted $\Psi(f; f_s, t_c, \xi_{1,2})$, is significantly more complex than that which was presented in the earlier chapters. The signal phase for LIGO is expressed as:

$$\Psi(f; f_s, t_c, \xi_{1,2}) = -2\pi f_s \left[\frac{f}{f_s} t_c + \frac{3}{5} \xi_1 \left(\frac{f}{f_s} \right)^{-5/3} + \xi_2 \left(\frac{f}{f_s} \right)^{-1} \right] + \frac{\pi}{4}, \tag{6.7}$$

where t_c is the time that the inspiral will take to coalesce and $\xi_{1,2}$ are chirp times that are defined to be:

$$\xi_1 = 34.5 \left(\frac{\mathcal{M}}{M_\odot} \right)^{-5/3} \left(\frac{f_s}{40Hz} \right)^{-8/3} \text{sec.}, \tag{6.8}$$

$$\xi_1 = 0.0837 \left(\frac{743}{84} + \frac{11\mu}{M} \right) \left(\frac{M_\odot}{\mu} \right)^{-5/3} \left(\frac{f_s}{40Hz} \right)^{-2} \text{sec..} \tag{6.9}$$

The phase at any other detector can be defined by replacing t_c with $t_c + \tau_{(A)}$ where $\tau_{(A)}$ is the relative time delay between detectors. Therefore, the phase at any other detectors can be written in terms of 6.7 as $\Psi_{(A)}(f; f_s, t_c, \xi_{1,2}) = \Psi(f; f_s, t_c, \xi_{1,2}) - 2\pi f \tau_{(A)}$. With these quantities defined as such, the statistic will follow the same outline that was derived for the LISA case with some minor deviations due to these quantities defined above.

Although the coherent code has the capabilities to combine output from as many as four detectors, the joint searches with non-LIGO detectors is just now coming to fruition and to date no coherent study has been completed on these cases. Therefore, the primary focus of this section will be to outline the search strategies that incorporate only the two Hanford detectors as well as the Livingston detector. The network statistic for the various types of networks can be written in terms of the constituent detector's quadrature phase values. For the three LIGO detectors, there are a total of three possible ways of combining

the constituent detectors quadrature phases.

Case 2a would only include the two Hanford detectors. These detectors are co-located, have identical orientations and share the same noise PSD. As a result, the signal measured by these two detectors are not statistically independent. Therefore the network statistic is written as:

$$\Lambda_{2a} = \frac{1}{\sqrt{2}} \mid C_1^* + C_2^* \mid = \frac{1}{\sqrt{2}} \sqrt{\rho_1^2 + \rho_2^2 + 2(c_{1;0}c_{2;0} + c_{1;\pi/2}c_{2;\pi/2})}, \tag{6.10}$$

where $\rho_i = \sqrt{c_{i;0}^2 + c_{i;\pi/2}^2}$. At this point it helps to redefine some parameters. For the purpose of presentation, the cross term will be defined to be cross$= 2(c_{1_0}c_{2_0} + c_{1_{\pi/2}}c_{2_{\pi/2}}) = 2\rho_1\rho_2 cos(\phi)$ and the ρ^2 without any index will imply the sum of the individual ρ^2's. So for this two detector case, $\rho^2 = \rho_1^2 + \rho_2^2$.

Case 2b would be the network that incorporates a single Hanford detector and the Livingston detector. These detectors are physically separated with different orientations and noise PSD. As a result, these detectors are statistically independent and the network statistic is then written as:

$$\Lambda_{2b} = \sqrt{\mid C_1 \mid + \mid C_2 \mid} = \sqrt{\rho_1^2 + \rho_2^2}. \tag{6.11}$$

For this particular case, the coherent statistic Λ is equivalent to the total ρ^2 as defined above.

Case 3 would be the network that incorporates all the LIGO detectors. The two Hanford detectors are co-located and statistically dependant where as the Livingston detector would be statistically independent. The network statistic can then be written as:

$$\Lambda_3 = \sqrt{\mid C_1^* + C_2^* \mid + \mid C_3 \mid} = \sqrt{\rho_1^2 + \rho_2^2 + \rho_3^2 + 2(c_{1;0}c_{2;0} + c_{1;\pi/2}c_{2;\pi/2})}, \tag{6.12}$$

where index 1 refers to H1, index 2 refers to H2, and index 3 indicates the L1 detector.

6.3 New Functionality and Changes

The end result of the coherent code is to provide as much information about possible signals as possible. In an effort to achieve this goal, many new additions have been implemented within the code to provide necessary information or just additional information to make analysis of triggers more straight forward in the future. All of these functionalities will be discussed at great length throughout the rest of this chapter. The first necessary functionality that was incorporated into the coherent code as the ability to track the source location in geocentric coordinates. Another useful functionality that was incorporated into the coherent code is the ability to output the quadrature phase values from all detectors that are involved with a particular trigger. The ability to perform time slides was also built into the coherent code. This required appropriately tracking the events at the single detector level as well.

Although the conversion from equatorial coordinates to geographical coordinates was not a difficult change to implement, it does provide a more traditional astronomical measurement of the source location. The necessary changes were isolated to just coherent_inspiral.c.

Tracking the individual detector's quadrature phase values at the time of a coherent trigger proved to be a significantly more challenging change to implement. As illustrated in the previous section, the individual detector's quadrature phase values are need to construct the coherent SNR. However, these values can also be used to determine how well the phase agrees between two participating detectors when trigger has been recorded. As will be illustrated in the following section, one of the powers of the coherent code is the ability to

make signal based vetoes on certain parameters that are only available to the coherent code. The phase difference that occurs between the H1 and H2 detectors in Case 2a and Case 3 is one of the possible veto parameters that has been considered for the coherent search. Considering that a real event would have phase agreement between two collocated detectors, the ability to calculate this phase on the fly once you have a series of events is crucial to rule out noise events or other detector related issues. This change required subsequent changes in several other files such as coherent_inspiral.c, CoherentInspiralFilter.c, LIGOLwXML.c, LIGOLwXMLInspiralHeaders.h and LIGOMetadataTables.h. The actual tracking of the phase is performed in CoherentInspiralFilter.c but the output of all triggers generated is performed in coherent_inspiral.c so that needed to be altered as well. The addition of new fields to the table of events as well as outputting these entries into the xml files required altering the remaining files listed above.

The incorporation of time slides was the final change that was implemented in the coherent code. Time slides are a particular study whereby the data from one detector gets slide in time with respect to the data from another detector by some predetermined amount. When this occurs, any trigger that is found while searching over this "slide" data can not possibly be a real trigger and must be associated with a noise event. This in essence allows one to study how the "background" behaves in the absence of real events. This is important if one desires to make vetoes based on different parameters such as the phase agreement between two detectors. For example, recent searches have indicated that the background is evenly distributed in phase difference between two detectors but the injected signals are clustered near small phase differences. This suggests that this study can be used to determine what value of the phase difference can be used to rule out triggers generated by noise events.

6.4 Coherent Searches

Before the coherent search can be implemented in the real time searches, there are several studies that are required to demonstrate the functionality of the coherent search as well as to illustrate the power of the coherent search over the coincident search methods that are currently being implemented. The studies that are presented throughout the rest of this section serve as the determining factor for the Inspiral Working Group's (IWG) decision to incorporate the coherent code as the final stage of the inspiral pipeline. The studies performed were on S3 and S5 data. The S3 study consisted of studying software injections in the S3 science data, time slides of the S3 science data and then a zero-lag study. The injection and time slide studies are used as benchmarks to determine parameter tuning before you implement a real search on the S3 data whereas the zero-lag study is an actual search over the S3 data that incorporates the parameter tunings determined by the previous studies. The difference between software and hardware injections is straight forward. The software injections are performed on raw data after it has been collected by the detectors whereas the hardware injections are performed by actuating the test masses to replicate an impinging inspiral signal. The S5 study was very similar to the S3 study in that it looked at the software injections, time slides and zero-lag studies to see how well the coherent code performed during the current science run. With all these studies, the individual detector results will be presented along side the coherent results. The individual results are presented with the coherent results to serve as a direct comparison to what the current search pipeline is already capable of achieving.

6.4.1 Science Run 3

The Science Run 3 (S3) study provided the first measure of how accurately the coherent code was performing on data collected from all three LIGO detectors. It also furnished the LIGO Science Collaboration (LSC) with the first benchmarks on phase vetoes whereby possible triggers could be ruled out if the phase did not agree between the two Hanford detectors. These crucial first steps provided the foundation for all future studies using the coherent code and illustrate the necessity to incorporate the coherent code into LIGO's real time search pipeline.

S3 Vetoing

When any detector registers a possible event, the candidate event must pass a series of rigorous tests before the event can be classified as a real event or simply related to some noise event. At the single detector level, LIGO performs a series of vetoes when a trigger is registered. For example, when both Hanford detectors are operational any candidate event must occur in both detectors and the time at which they are registered by the two detectors must be within a few milliseconds. Any trigger that is does not meet these requirements are vetoed. Determining these threshold values is one of the remaining challenges that will always be associated with real time searches for current and future science runs. These values must be chosen to minimize the false alarm probability so that the detector does not continually registering false triggers. At the same time, the vetoes must be chosen in such a way so as to minimize the false dismissal probability as well so that a real event does not go undetected.

These studies must be performed separately for each science run considering that the state of the detectors, such as its sensitivity and noise power spectral densities, vary from one science run to the next. There are two main studies that are performed to determine how to apply vetoes, namely time slides and injections. As mentioned above, time slides give a measure of the noise background for the LIGO detectors. Injection studies involve injecting known signals into the data or physically inject the signals into the detector by actuating the test masses. The goal is then to see how well the detector can recover the injected signals. These two can be used to determine the false alarm and false dismissal probabilities associated with any given cuts performed. One other useful study is the zero-lag study where a real search is performed on the data without injections or time slides. In the absence of real events, this study should mimic the results obtained in the time slide studies. Figure 6.2 illustrates the bare results with no cuts performed. The axis labeled $\cos(\phi)$ refers to part of the cross term that was defined below 6.10. This is a measure of the phase agreement between the two collocated detectors. The axes labeled Log(H1) or Log(H2) refer to the Log of individual detectors search statistic. The search statistic is comprised of ρ and χ^2 as follows [89]:

$$S = \rho^4 / \left(\chi^2(\rho^2 + 250)\right), \tag{6.13}$$

where χ is a statistical quantity that measures whether observed results differ substantially from the expected results [25, 88].

As is evident from fig. 6.2, the injections have a significant separation from the background triggers. To filter out the background, a paraboloid cut in the $\mathrm{H1} - \mathrm{H2} - \cos(\phi)$ space is performed. The veto criteria is as follows:

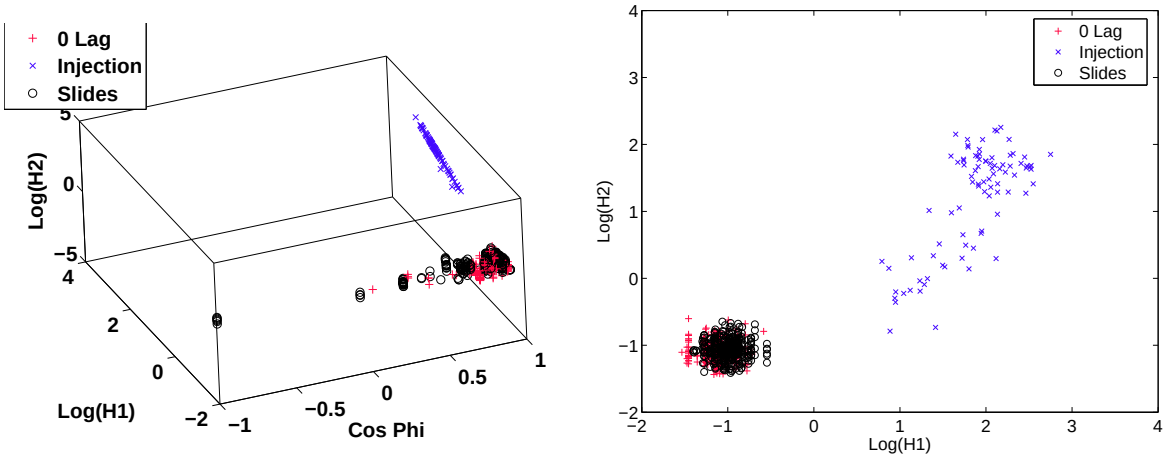

Figure 6.2: This figure shows the results of the S3 studies that were performed using time slides, zero-lag and injections before any vetoes were performed. The second plot is the same results from the first plot just projected onto the H1-H2 search statistic plane.

$$0 > \delta_{\cos(\phi)}(\cos(\phi) - \Delta_{\cos(\phi)})^2 + \quad \delta_1 \quad (\cos(\vartheta)S_{\rm H1} - \sin(\vartheta)S_{\rm H2} - \Delta_{\rm H2})^2 \tag{6.14}$$

$$- \quad \delta_2 \quad (\cos(\vartheta)S_{\rm H2} + \sin(\vartheta)S_{\rm H1} - \Delta_{\rm H1}), \tag{6.15}$$

where $\delta_{\cos(\phi)}$ determines how fast the paraboloid rises in the $\cos(\phi)$ direction, δ_1 and δ_2 determine how fast the paraboloid rises in the H1-H2 plane The parameters $\Delta_{\cos(\phi)}$, $\Delta_{\rm H1}$, and $\Delta_{\rm H2}$ determine where the apex of the paraboloid is set and ϑ determines the inclination of the paraboloid in the H1-H2 plane. Although the general expression for the veto criterion will be valid for each science run, the values for the variables chosen may change from one run to the next. For S3, the values were chosen such that all the background triggers were removed without removing a single injection. This amounted to the following values, $\delta_{\cos(\phi)}$=100, δ_1=1, δ_2=0.3, ϑ=0.661 radians, and $\Delta_{\cos(\phi)}$=1. The choice for the two other displacements were determined by a simple rotation in the H1-H2 plane defined as follows:

$$\Delta_{\rm H1} \quad = \quad {\rm H1}_0 \cos(-\vartheta) + {\rm H2}_0 \sin(-\vartheta) \tag{6.16}$$

$$\Delta_{\mathrm{H2}} \quad = \quad -\mathrm{H1}_0 \sin(-\vartheta) + \mathrm{H2}_0 \cos(-\vartheta), \tag{6.17}$$

where $\mathrm{H1}_0$=-0.4 and $\mathrm{H2}_0$=-2. Figure 6.3 illustrates the veto criterion without removing any triggers. The shaded region outlines the region of parameter space where all triggers must remain if they are to pass the veto criterion. Figure 6.4 just illustrates the effectiveness of the cut where all background triggers have been vetoed using the criterion defined in eq. 6.14 above. Although there are not many low SNR injection triggers, the choice for the apex of the paraboloid is such that it will still allow for the possibility of significantly smaller SNR triggers to pass the veto stage. This is important so that the false dismissal probability is still minimized and also provides the ability to detect actual signals from sources that are significantly further away.

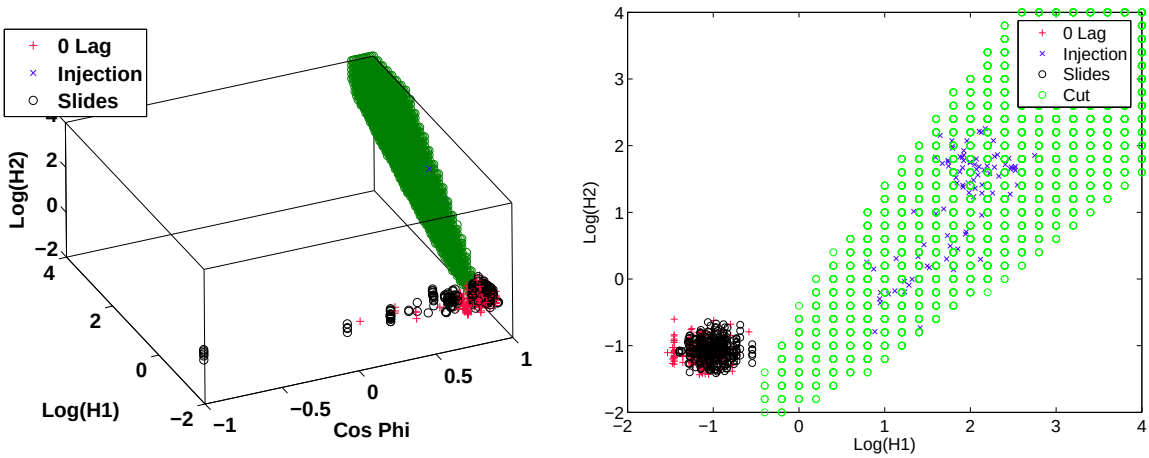

Figure 6.3: This is the same plot as fig. 6.2 just with the veto paraboloid in place but before the veto criterion has been implemented. Any triggers in the shaded region will be kept and those outside will be vetoed. The second plot is simply a projection of the first plot onto H1-H2 search statistic plane.

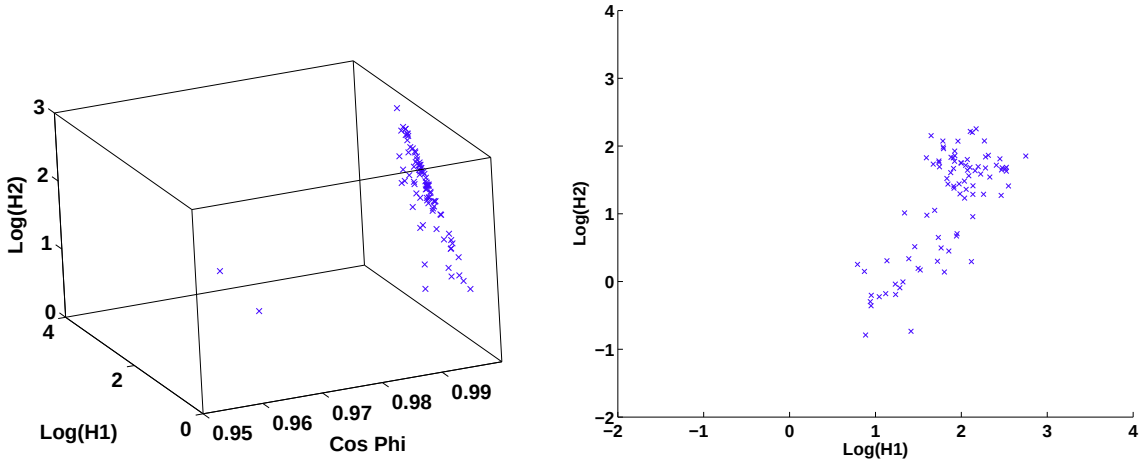

Figure 6.4: This figure shows the results of the S3 studies that were performed using time slides, zero-lag and injections after the vetoing has been performed. Notice how only the injection blue cross remain. Again, the second plot is the same results from the first plot just projected onto the H1-H2 search statistic plane.

S3 Search Accuracy

With the vetoing in place, the next logical step is to examine how accurately the searches are recovering the injected triggers. Just as the studies performed with LISA illustrated, the accuracy with which a source parameter can be identified instills confidence in the search algorithms that are being used. This process of identifying parameter accuracies is the final stage before any new search algorithm can be accepted into the search pipeline by the IWG. Another large benefit of this step is that it has and will continue to help identify possible bugs in the search pipeline. In this subsection, the parameter accuracies that will be presented should agree with those obtained in the earlier stages of the pipeline and therefore will be presented along with those results for direct comparison.

The first parameter that will be examined is the timing accuracy. This is a measure of how well the coherent search recovers the injected signal's end time. Any large outliers in the timing accuracy would be cause for concern and warrant immediate investigation. This

is important when using matched filtering because a small offset in the timing can cause the entire phase of the template to be offset with that of the injected signal. Any offset in a signal phase with a template would substantially reduce the overall SNR of the recovered trigger, which is why it is so important to accurate recover the signal end time. The timing accuracy is measured in units of seconds and can be written as a simple difference as seen below:

$$\Delta t = t_{\text{inject}} - t_{\text{recovered}}. \tag{6.18}$$

Figure 6.5 are histograms of the timing accuracies for the coherent code as well as the individual detectors that participated in the coherent trigger.

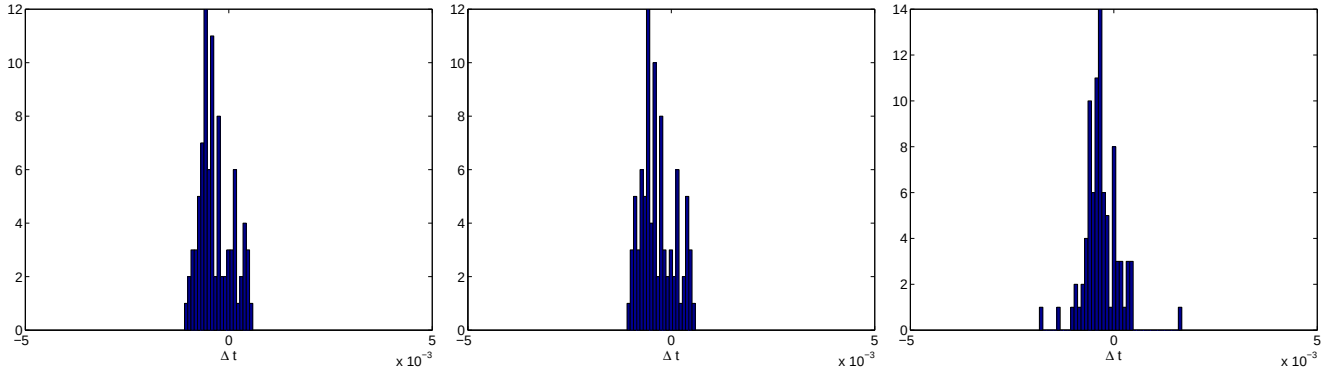

Figure 6.5: These are histograms of the timing accuracy returned from the coherent code as well as the associated triggers from the individual detectors. The histogram on the left is the results from the coherent code, the histogram in the center is the results from H1 detector and the histogram on the right is that for H2 detector.

The overall SNR of recovered triggers can be affected in a variety of ways. If the injected signal is very distant and nearing the horizon distance, which is a measure of how far the detector is capable of seeing, the SNR will be significantly lower than a similar signal that is much closer. Another mechanism that can contribute to a drop in SNR was briefly mentioned earlier, if the template used for the matched filtering does not exactly match the actual

injected signal, the overall SNR will suffer as well. Therefore, the larger the recovered SNR the better agreement the template should have with the injected signal. This is what is illustrated in fig. 6.6. The timing accuracy is plotted against the SNR of the trigger. As the SNR of the injected signals increases, the code is able to determine the start time of the signal more accurately. This effect is even more pronounced for other search parameters.

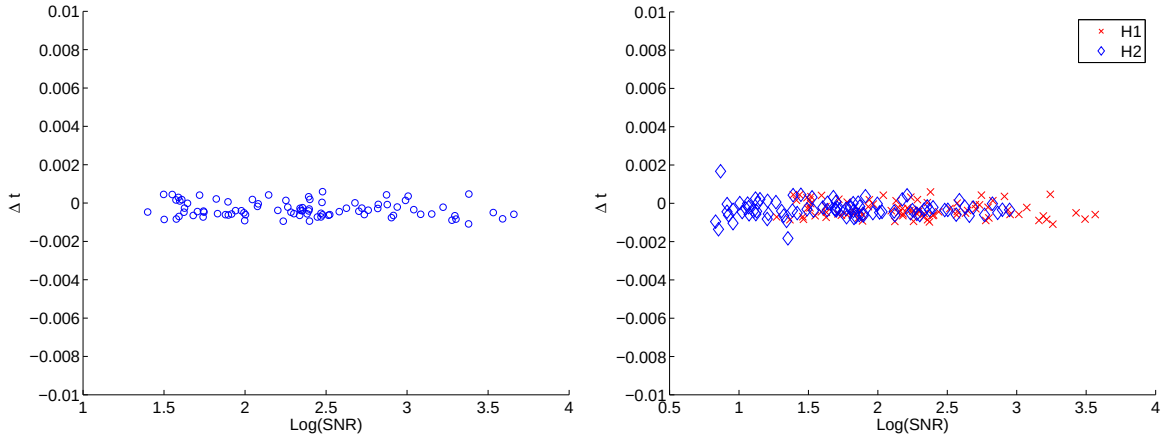

Figure 6.6: These plots illustrate how the code returns increasing more accurate values as the SNR of the associated triggers increases. The plot on the left illustrates the results from just the coherent code whereas the plot on the right has the results from both the H1 and H2 detectors.

The next parameter of interest is the chirp mass. The chirp mass has significant contribution to the signal phase seeing that it determines how fast the frequency of the chirp signal will evolve. Just as with other parameters, errors in the chirp mass can results in signals remaining undetected. Figure 6.7 are histograms of the accuracy in which the search pipeline can recover the chirp mass. The chirp mass accuracy is a unitless quantity defined to be:

$$\Delta M_{chp} = \Delta\mathcal{M} = \frac{\mathcal{M}_{\text{inject}} - \mathcal{M}_{\text{recovered}}}{\mathcal{M}_{\text{inject}}}. \tag{6.19}$$

The larger SNR triggers should again show increased resolution in the chirp mass parameter

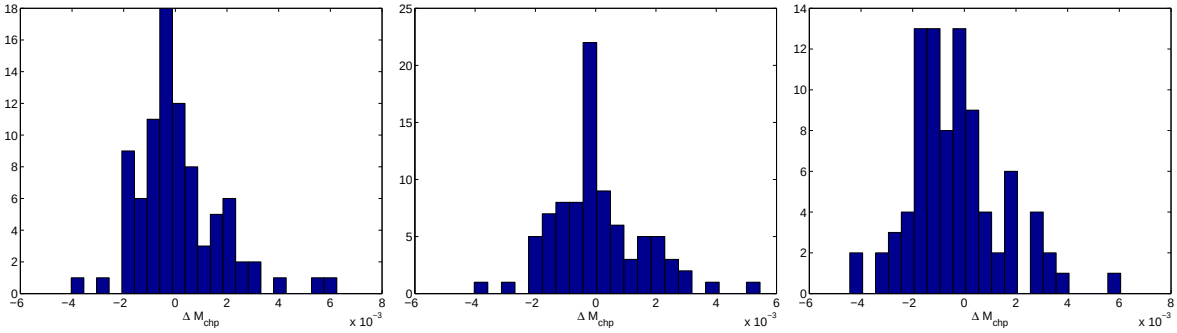

Figure 6.7: These are histograms of the chirp mass accuracy returned from the coherent code as well as the associated triggers from the individual detectors. The histogram on the left is the results from the coherent code, the histogram in the center is the results from H1 detector and the histogram on the right is that for H2 detector.

as is illustrated in fig. 6.8. Currently, the coherent code uses the chirp mass from template than rang off with the highest SNR from the individual detector when performing the coherent search. Therefore, the chirp mass accuracy as a function of SNR should resemble the largest SNR triggers in the individual detector case as illustrated in fig. 6.8. In some cases, the chirp mass accuracy is identical to the triggers from H1 and in other cases it is identical to the triggers in H2. Since a large majority of the time the larger SNR trigger is also more accurate, the current implementation of the coherent code will as a whole yield more accurate results for the chirp mass than any single detector search would. Essentially, the coherent code will more often than not chose the template for its filtering that has the more accurate chirp mass.

The next parameter that will be considered is the effective distance. The effective distance is at most equal to the actual injected distance when a detector is optimally oriented with respect to a given source. However, more often than not it can deviate from the actual distance when a detector is suboptimally oriented with respect to the source under consideration. The relationship between the actual distance and the effective distance is determined

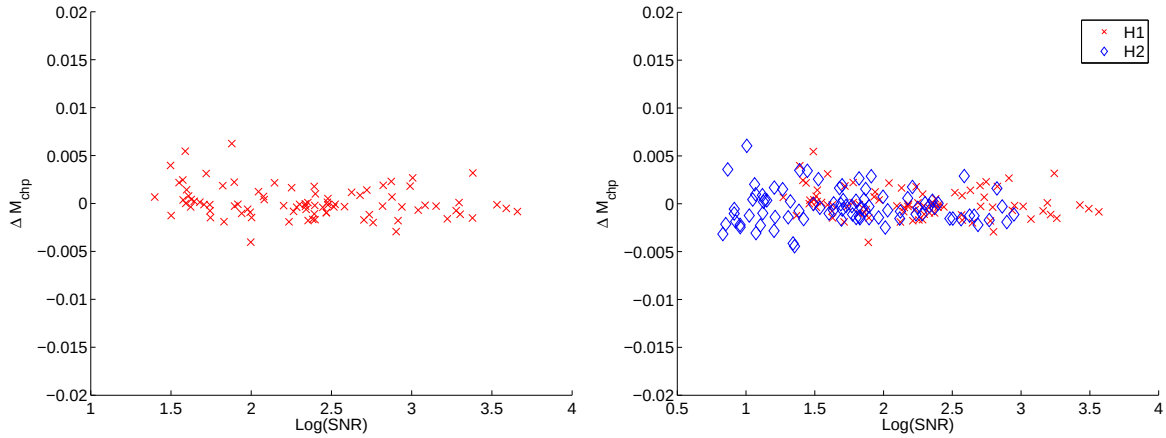

Figure 6.8: These plots illustrate how the code returns increasing more accurate values as the SNR of the associated triggers increases. The plot on the left illustrates the results from just the coherent code whereas the plot on the right has the results from both the H1 and H2 detectors.

by the following equation [83]:

$$D_{eff} = \frac{D}{\sqrt{F_+^2(1+\cos^2(\iota))^2/4 + F_x^2\cos^2\iota}} \tag{6.20}$$

Determining the effective distance from the detector dependant quantities was first developed by Duncan Brown. For the individual detector case, the effective distance can be expressed as [24]:

$$D_{\text{eff}} = \sqrt{\frac{4\Delta t T S}{N}}\rho^{-1} = \sigma/\rho, \tag{6.21}$$

where ρ is the individual detector SNR, Δt is the time point spacing, N is the total number of time points, T is the template norm and S is the detector dependant norm. For the two detector network comprising both Hanford detectors, the effective distance takes the following form:

$$D_{\text{eff}} = |\sigma_1 + \sigma_2|/(\sqrt{2}\rho_{coh}). \tag{6.22}$$

For notational simplicity, D is assumed to be D_{eff} unless otherwise specified. The distance accuracy is also a unitless quantity defined to be

$$\Delta D = \frac{D_{\text{inject}} - D_{\text{recovered}}}{D_{\text{inject}}}. \tag{6.23}$$

Figure 6.9 shows the first major problem with the coherent code. The individual detector histograms do not show any significant offset and appear to be centered at 0 as they should. However, the coherent code result does in fact show an offset. This was attributed to the method in which the coherent code was determining the effective distance. The individual detector norms were not accounted for properly and this resulted in the systematic offset that is apparent in the first histogram in fig. 6.9. Figure 6.10 is a side by side comparison of the results from the new implementation of calculating the effective distance and the previous incorrect method. What is evident from this figure is the remarkable improvement in determining the effective distance. Figure 6.11 is the accuracy vs. SNR plot. Again, it is important to note the improvements in the calculation of the effective distance above the individual detector case. The individual detector's sigma values weight each detector's contribution to the effective distance differently. This results in an overall increased resolution in effective distance when compared to the individual detector case.

Coherent analysis provides the means to measure source locations provided there are enough participating detectors. Case 2b or 3 that include at least one Hanford detector and the Livingston detector will not be sufficient to triangulate a source location. However, a two detector network can determine the cone angle at which the source is located. This is illustrated in figure 6.12. Knowing the light travel time between the Hanford and Livingston detectors (10ms) as well as the time of arrival difference between triggers generated by the

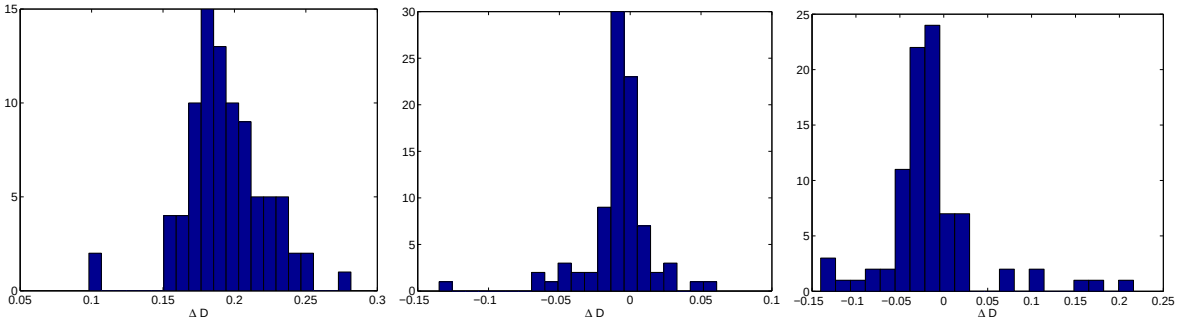

Figure 6.9: These are histograms of the distance accuracy returned from the original coherent code as well as the associated triggers from the individual detectors. As illustrated, there appears to be a significant error associated with the way the coherent code is determining the effective distance. The histogram on the left is the results from the coherent code, the histogram in the center is the results from H1 detector and the histogram on the right is that for H2 detector.

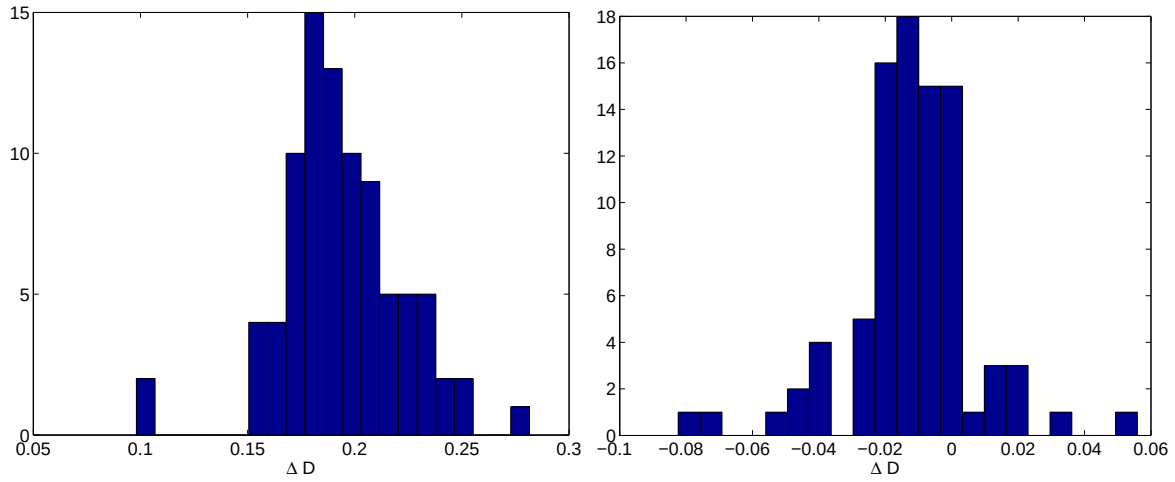

Figure 6.10: This figure illustrates the difference between the old and new implementation of the effective distance calculation in the coherent code. The histogram on the left is the old method and the one on the right is the new corrected method.

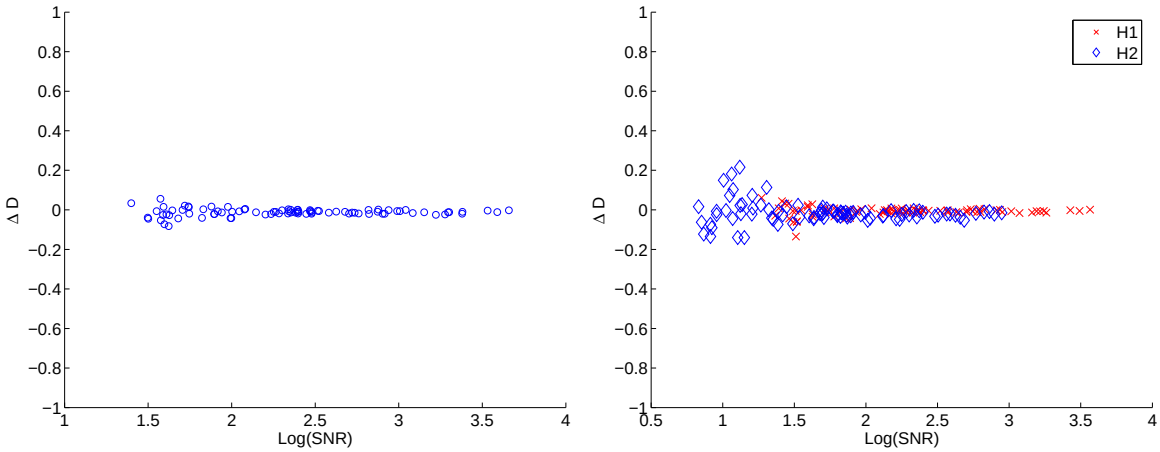

Figure 6.11: These plots illustrate how the code returns increasing more accurate values as the SNR of the associated triggers increases. The plot on the left illustrates the results from just the coherent code whereas the plot on the right has the results from both the H1 and H2 detectors.

two sites, (Δt), the cone angle is simply $\alpha = \cos^{-1}(\Delta t/10ms)$.

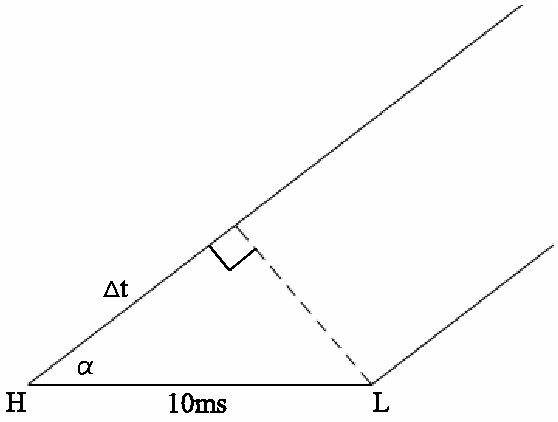

Figure 6.12: This figure illustrates how one can determine the cone angle from the time delays.

The accuracy in which the time delays can be measured is the limiting factor in this measurement. The higher stages of the pipeline do a coincidence analysis whereby the triggers from Hanford are checked for coincident triggers in Livingston data. This can provide some measurement of the time delay but as is illustrated in fig. 6.13 this method is very inaccurate when compared to the results obtained using the coherent code.

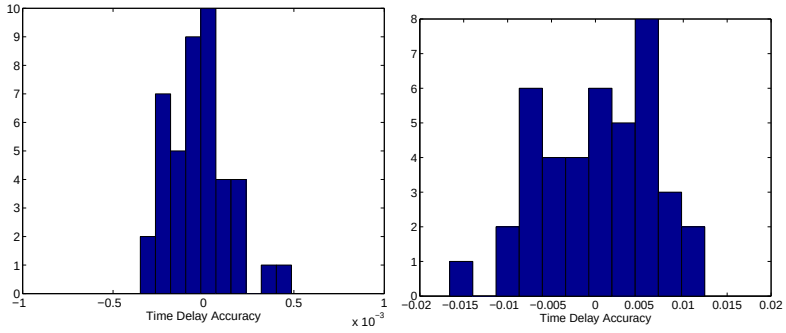

Figure 6.13: These plots illustrate one of the more powerful features of the coherent code. The histogram on the left is the results obtained by the coherent code whereas the histogram on the right is the results obtained from the single detector coincidence study.

6.4.2 Science Run 5

Science run 5 (S5) has a great many improvements over the past science runs. S5 marks the first time that LIGO will be actively searching for signals with all three detectors for an entire year of coincidence data acquisition. This science run also marks the first time that LIGO has achieved its design sensitivity. Therefore the noise in the data is significantly lower and as a result the data collected is much cleaner than in previous science runs. In addition to all the improvements that this science run has over the past science runs, it will also be the first time that the coherent code will be implemented in the real time searches. This is possible mainly in part to the results presented for the S3 searches as well as the preliminary study on the first epoch of S5 data presented in this subsection. The first epoch of S5 data covers the first 64 days of S5 and all results obtained in the following subsections reflect the runs that were performed only on this small subset of S5 data.

S5 Vetoing

The S3 study furnished the inspiral group with the first coherent veto that could effectively eliminate many background triggers without removing a single injected trigger. Although

this study laid the foundation of the coherent veto, the tuning of the parameters for S5 data is an ongoing process. For each epoch, the veto will be retuned and then applied to the inspiral search pipeline. However, to date the tuning of the first epoch veto is still a work in progress. In the S3 data, all the studies presented above were performed on what is termed "playground" data. This is 10% of the entire data set that is used for parameter tuning and adjustments before applying the tuned parameters to the full data set. This is necessary so that one does not bias the zero-lag studies that could possibly contain actual signals. However, the time slide and injection studies can be performed on the entire data set without such a bias being present. In the past, this was not necessary owing to the fact that the S3 data was very noisy and the playground study supplied a significant number of triggers to develop reasonable statistical results. The difference in S5 is that the time slides on just the playground data will not generate enough triggers to provide an accurate representation of the background. Therefore, the time slide studies are performed on the entire data set for this very reason. As a result, the study requires significant more time and will continue to evolve as LIGO continues to collect data for S5 well into 2007. The time slide study for the first epoch will be completed in the coming months and then a true coherent veto using the formula defined in eq. 6.14 can be applied for the S5 search.

S5 Search Accuracy

The S5 search is very similar to the S3 search with the exception of the veto parameters discussed previously. The results presented in this subsection are for the same parameters presented earlier in the S3 study.

Although this study involves a significantly larger population of triggers, the overall re-

sults are in very close agreement with those found in the S3 study. This provides significantly better statistics which in turn instills more confidence in the functionality of the coherent code. As already mentioned, the increased confidence in the performance of the coherent code resulted in the recent decision to implement the coherent search as the final stage of the LIGO's online search pipeline. Figures 6.14 and 6.15 are the timing accuracy results for S5. Figures 6.16 and 6.17 are the mass accuracy results for S5. Figures 6.18 and 6.19 are the distance accuracy results for S5 and 6.20 is the time delay accuracy results for S5. As illustrated in all these aforementioned figures, the coherent search in S5 just as in S3 is in many cases performing better than any single detector study that was performed. As the search methods improve and the detector sensitivities increases, overall the parameter resolutions should continue to increase just as they have from S3 to S5.

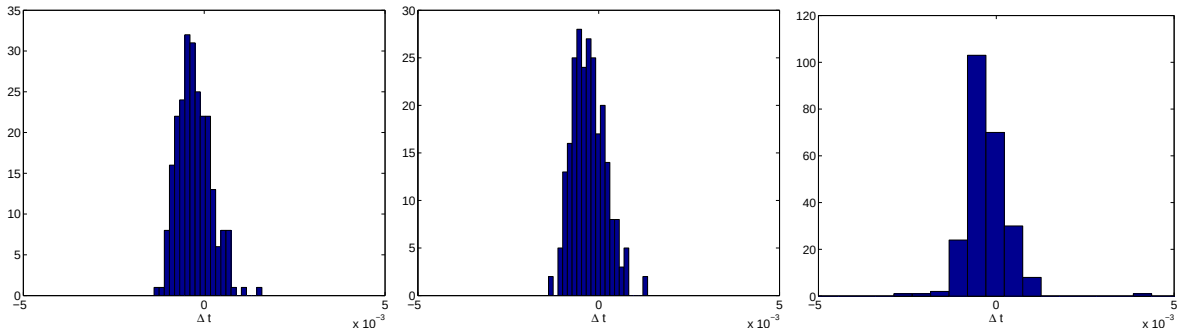

Figure 6.14: These are histograms of the timing accuracy returned from the coherent code as well as the associated triggers from the individual detectors. The histogram on the left is the results from the coherent code, the histogram in the center is the results from H1 detector and the histogram on the right is that for H2 detector.

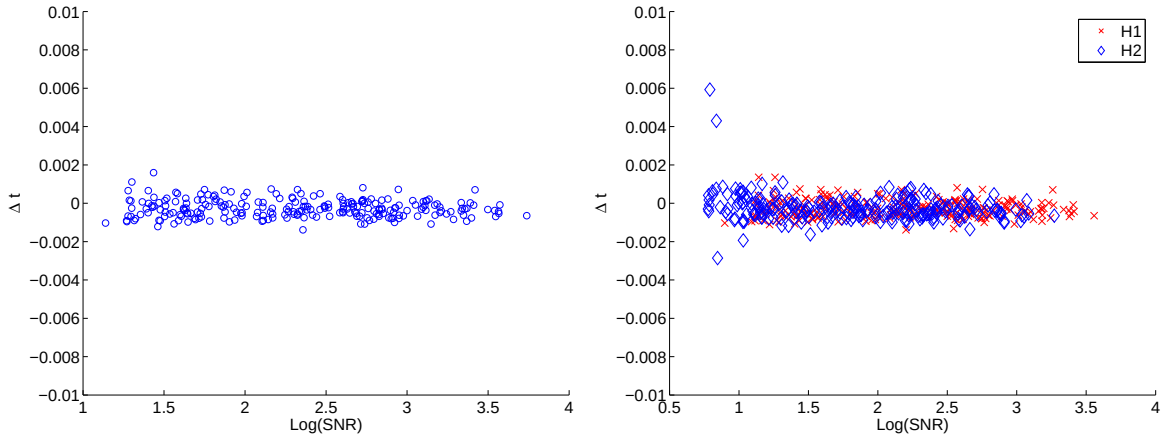

Figure 6.15: These plots illustrate how the code returns increasing more accurate values as the SNR of the associated triggers increases. The plot on the left illustrates the results from just the coherent code whereas the plot on the right has the results from both the H1 and H2 detectors.

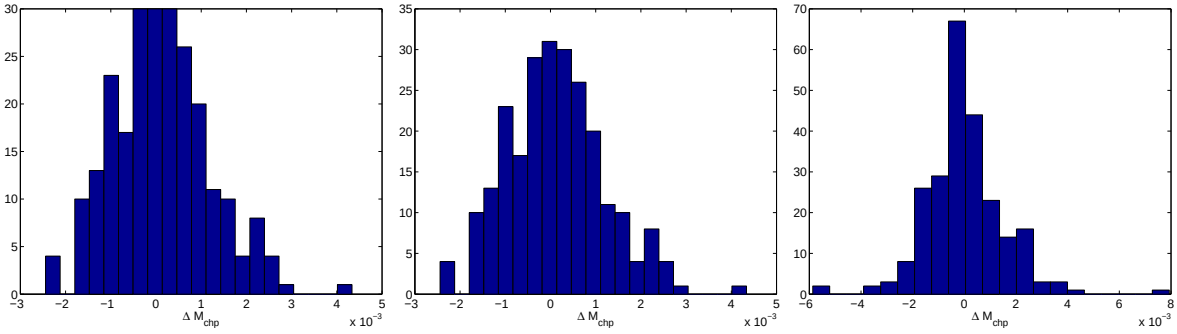

Figure 6.16: These are histograms of the chirp mass accuracy returned from the coherent code as well as the associated triggers from the individual detectors. The histogram on the left is the results from the coherent code, the histogram in the center is the results from H1 detector and the histogram on the right is that for H2 detector.

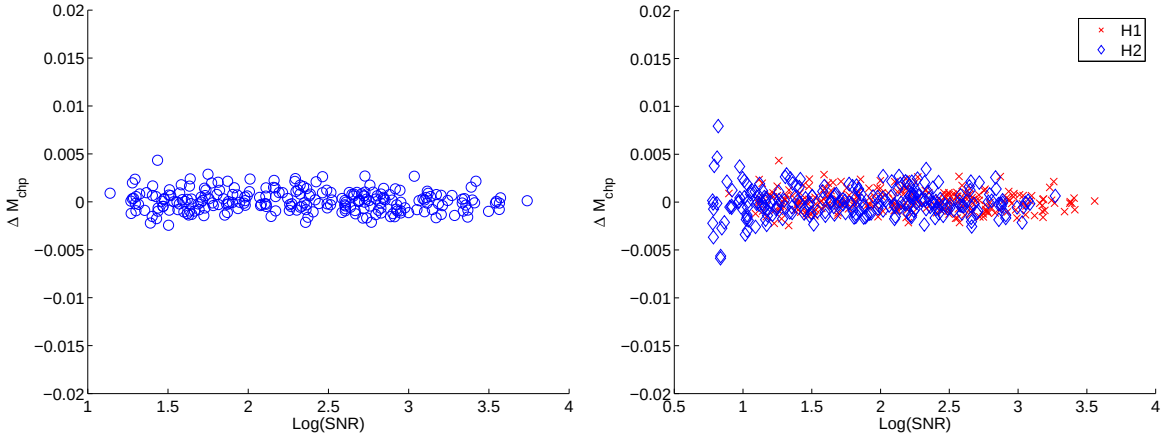

Figure 6.17: These plots illustrate how the code returns increasing more accurate values as the SNR of the associated triggers increases. The plot on the left illustrates the results from just the coherent code whereas the plot on the right has the results from both the H1 and H2 detectors.

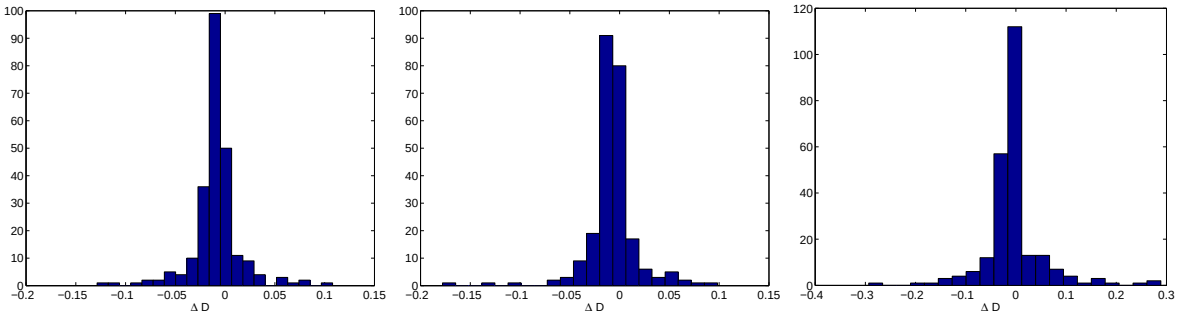

Figure 6.18: These are histograms of the distance accuracy returned from the coherent code as well as the associated triggers from the individual detectors. The histogram on the left is the results from the coherent code, the histogram in the center is the results from H1 detector and the histogram on the right is that for H2 detector.

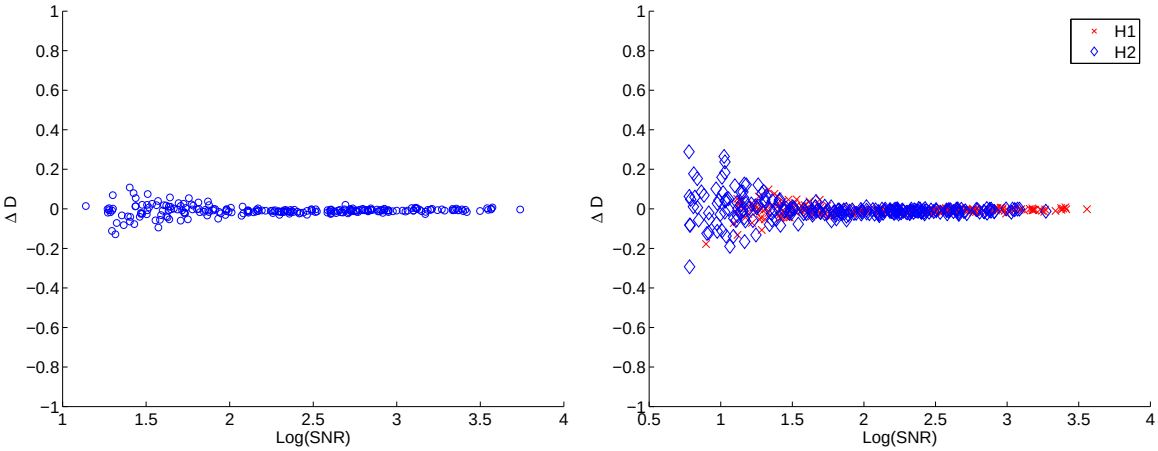

Figure 6.19: These plots illustrate how the code returns increasing more accurate values as the SNR of the associated triggers increases. The plot on the left illustrates the results from just the coherent code whereas the plot on the right has the results from both the H1 and H2 detectors.

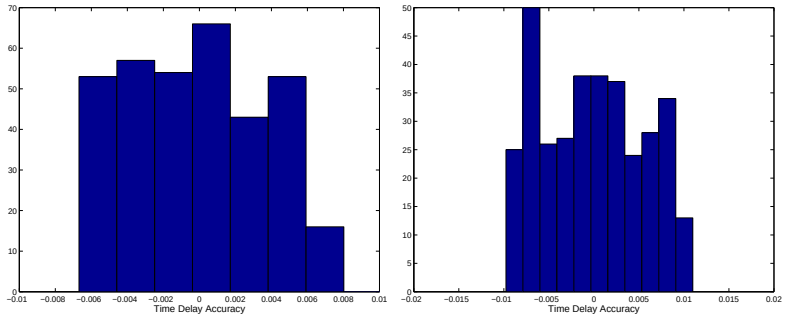

Figure 6.20: These plots illustrate one of the more powerful features of the coherent code. The histogram on the left is the results obtained by the coherent code whereas the histogram on the right is the results obtained from the single detector coincidence study.

Chapter 7

Conclusion

The search for gravitational waves can be defined by several stages that have been discussed throughout this dissertation. The first stage would be to define what a gravitational wave signal is, how the signal evolves over time and what are the parameters that define the signal. The second stage would be to devise a method to detect these signals whether it is using a bar detector, an earth based interferometric detector or space based interferometric detectors. The third stage would be to ascribe the upper limits on how well a chosen detector would perform in properly identifying a real signal as well as properly extracting the actual source parameters. The fourth stage is maintaining an operating gravitational wave detector so that future searches can be implemented. The final stage is to use the methods developed in the previous stages to complete real time searches for GW signals.

This dissertation has followed the entire progress of searching for GW signals from the very basics of gravitational wave physics through the actual real time searches that are currently being performed. The development of the search statistic for LISA as well as establishing an upper limit on LISA's ability to resolve source parameters serves as the

foundation for the proposed spaced based mission. What has been demonstrated throughout chapters 4 and 5 is that the detection and parameter estimation problem are related in a very complicated manner. Chapter 4 illustrated that searches with LISA can be accomplished with a very small template bank, however, these very same searches may not properly characterize the source accurately. This suggests the need for a hierarchical search algorithm where a course bank would be initially searched. Once a candidate event has been discovered, a second search using a significantly finer bank would then have to be performed. This point was explained in detail in the parameter estimation results presented in chapter 5, which illustrated the need to use a much finer template bank if one is to accurately identify source parameters. This is a challenge that LIGO does not face. The fine template banks that LIGO currently implements allow for the simultaneity of the detection and parameter estimation process as alluded to in chapter 6. Considering that the signals that will be available to LISA are long duration signals, the resulting template bank can afford to be very coarse without the fear of missing out on signals. However it is these same course banks that can result in misleading information about source parameters if followup searches are not performed.

It has also been demonstrated that the ability to resolve source parameters in the presence of the TDI variables as well as other noise contributions is very feasible. With NASA's current funding issues, it is studies such as those presented in this dissertation that may serve as the determining factor as to when LISA will actually fly. The upper limits established here illustrate that LISA science is achievable and if the opportunity is available, LISA will serve as a necessary counterpart to the operating Earth based GW detectors.

One of the main uncertainties involving GW detection is the ever evolving event rates for

the possible source that are available to any given detector. Since the event rates for most of the sources outlined in chapters 5 and 6 are changing periodically, the ability to detect each class of GW signal is imperative. The ability to search for as many varieties of signals as possible will increase the likelihood of eventually detecting a signal whether it is with LIGO or LISA. Another major benefit of both space based and earth based detectors functioning is that they provide complimentary information about similar sources, which can yield a complete picture of the evolution of inspiral signals. This is something that neither a Earth based or Space based detector can provide on their own.

The current generation of operating GW detectors are just now attaining design sensitivities in part to the software that has continually been refined over the past few years. Other than the obvious goal of detecting the first GW, the secondary goal of S5 is to collect a years worth of triple coincident data with all three LIGO detectors. It is new software tools like GainMon that provide the means to accomplish this task. The increased sensitivity has brought with it increased parameter resolution and a larger number of available sources, which in turn has increased the chances of detection using LIGO. The studies performed have allowed for the search methods discussed to finally be implemented into real time searches starting November 2006. The coherent search strategy will be the only search method currently be implemented that has the ability to identify source locations in addition to providing enhanced parameter resolution. The S5 science run will be the first time this search method is utilized and time will bare out its power over single detector searches. The final acceptance of the coherent code marks the end of the first stages of a GW search and the beginning of the final stage which will ultimately lead to the first GW detection.

Appendices

.1 Parameter Errors for Eccentric Sources

The parameter errors for the sources detailed in the section on eccentric waveforms in chapter 4 are significantly different from those presented in chapter 5. This is attributed to the additional information gained when incorporating the eccentricity as a parameters as well as the additional accuracy that comes with using the PN waveforms. As the eccentricity is increased, the PN waveforms departure from the Newtonian waveforms becomes more pronounced and therefore the error estimates should deviate from the Newtonian values as well. The direct comparison of the results presented here and those developed in chapter 5 is not possible. This is because those results presented in chapter 5 accounted for all the complications that arise when doing LISA data analysis including the Doppler phase as well as the incorporation of the TDI variables. The results here have been developed using a toy model that consists of analyzing just the pure monochromatic frequency using the Michelson variables and that is one reason they have been relegated to the appendix instead of incorporated directly into chapter 5. Although the direct comparison with the TDI results presented in chapter 5 can not be made, what will hold is the variation that the errors incur as you increase the eccentricity. For a more direct comparison of explicit values when there is no eccentricity, one should compare the results presented here with a similar study using Newtonian waveforms and the Michelson variables performed by Takahashi and Seto [67]. The code now exists to perform the complete study that incorporates all of the additional complications mentioned above, which leaves room for future work and publications.

All the figures in this section will be presented in a series of three plots. The first one on the left will always be the $e = 0$ case, the middle plot will always be the $e = 0.4$ case,

and the far right plot will be the $e = 0.6$ case unless otherwise specified. Just as illustrated in fig. 4.6, while all other parameters are held fixed, increasing eccentricity provides an increase in the overall SNR. As a direct result, parameter accuracies shown improvement with increasing eccentricity values as presented in fig. 1, 2, 3, 4, 5, and 6. The ability to measure the eccentricity parameter itself, which is illustrated in fig. 6, is only available once the eccentricity parameter is turned on. Therefore the left and right plots in fig. 6 are for the $e = 0.4$ and $e = 0.6$ case respectively. The parameters chosen for this study are the same as those presented in the eccentricity study in chapter 4 namely, $m_1 = 1\mathrm{M}_\odot$, $m_2 = 10\mathrm{M}_\odot$, $f = 1$ mHz, $\psi = 0$, and $\iota = 3\pi/10$ rads.

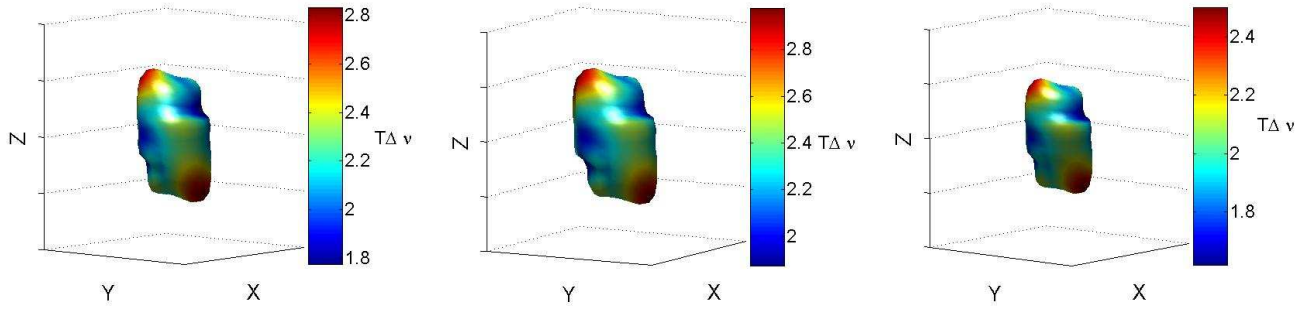

Figure 1: Frequency error plots for three different eccentric EBCOs, which have all other parameters identical, with $e = 0$, $e = 0.4$, and $e = 0.6$ (left to right).

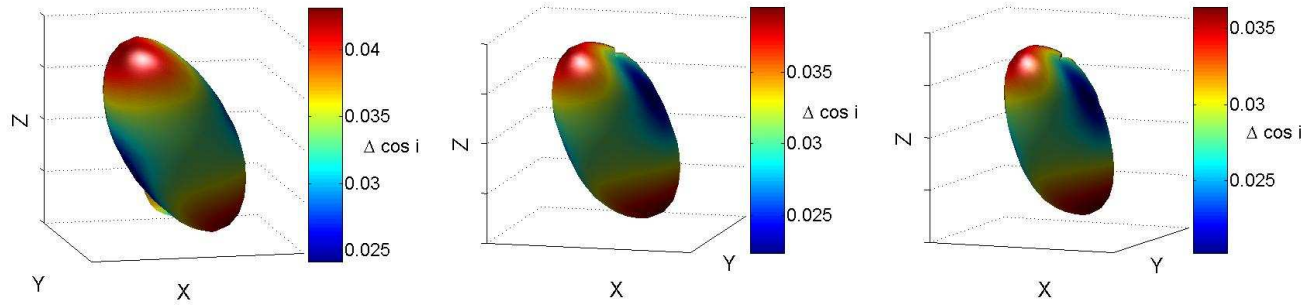

Figure 2: $\cos\iota$ error plots for three different eccentric EBCOs, which have all other parameters identical, with $e = 0$, $e = 0.4$, and $e = 0.6$ (left to right).

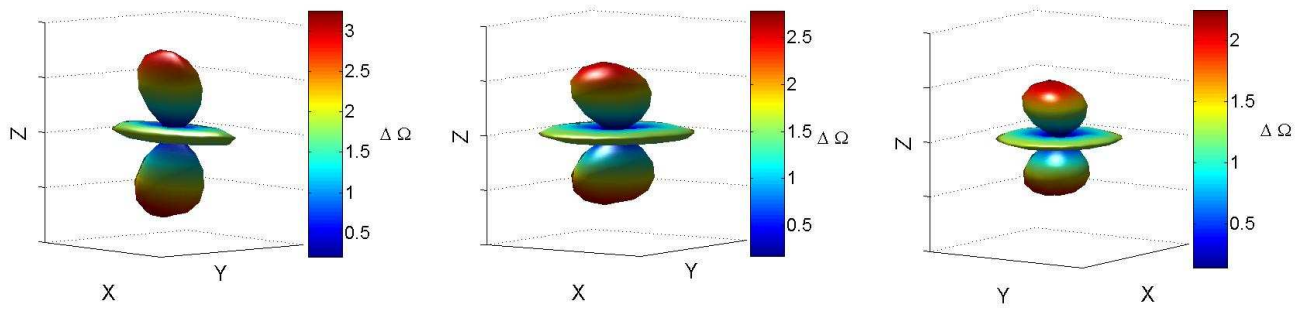

Figure 3: Source location solid angle error plots for three different eccentric EBCOs, which have all other parameters identical, with $e = 0$, $e = 0.4$, and $e = 0.6$ (left to right).

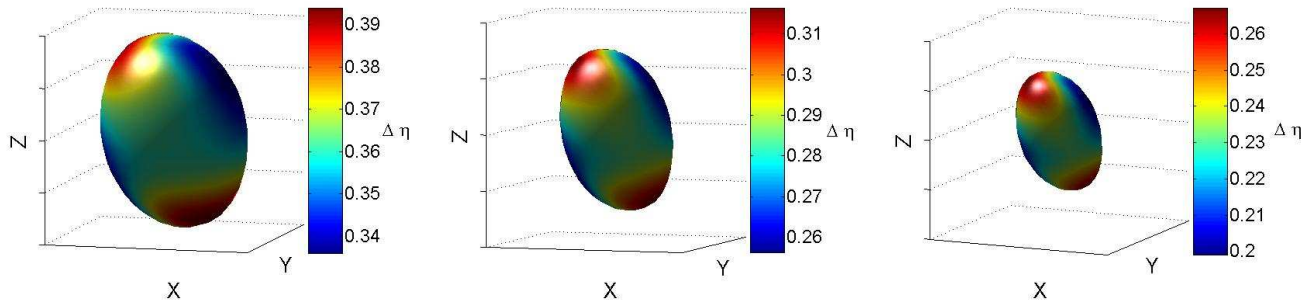

Figure 4: η error plots for three different eccentric EBCOs, which have all other parameters identical, with $e = 0$, $e = 0.4$, and $e = 0.6$ (left to right).

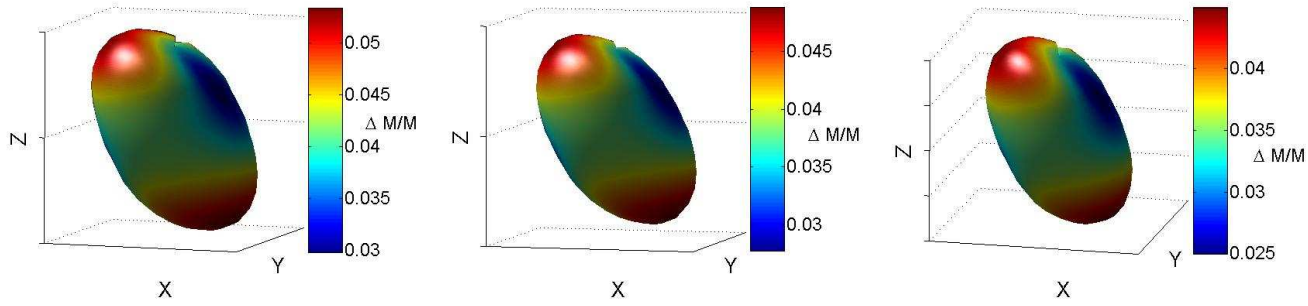

Figure 5: Total mass error plots for three different eccentric EBCOs, which have all other parameters identical, with $e = 0$, $e = 0.4$, and $e = 0.6$ (left to right).

.2 Acronyms and Abbreviations

BBH-Binary black hole
BH-Black holes
BNS-Binary neutron star

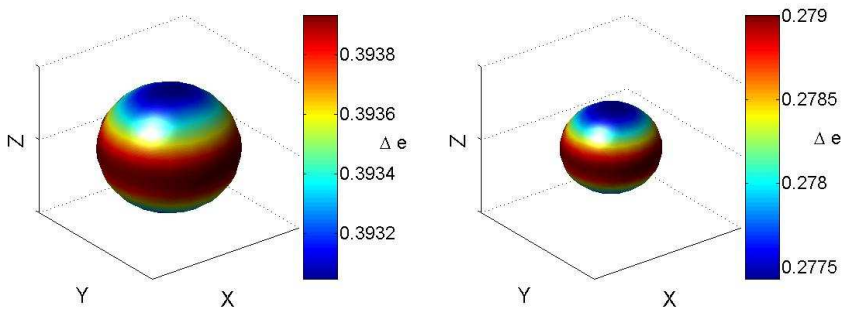

Figure 6: Eccentricity error plots for three different eccentric EBCOs, which have all other parameters identical, $e = 0.4$ and $e = 0.6$ (left to right).

CHP-chirp
EBCO-Eccentric binary compact objects
EM-Electromagnetic
EMRI-Extreme mass-ratio inspiral
FOM-Figures of merit
GW-Gravitational waves
H1-First gravitational wave detector at Hanford site
H2-Second gravitational wave detector at Hanford site
IFO(s)-Interferometer(s)
IWG-Inspiral working group
L1-Only gravitational wave detector at Livingston site
LIGO-Laser Interferometer Gravitational Wave Observatory
LISA-Laser Interferometer Space Antennae
LSC-LIGO science collaboration
LW-Long wavelength approximation
MLE-Maximum likelihood estimates
NS-Neutron stars
OLG-Open loop gain
PN-Post-Newtonian
PSD-Power spectral density
Scimon-Scientific monitor
S(1,2,3,4,5)-Science run (1,2,3,4,5)
SNR-Signal-to-Noise ratio
TDI-Time delay interferometry
TT-Transverse traceless
WD-White dwarfs
UGF-Unity gain frequency
XML-Extensible Markup Language

Bibliography

[1] M. Cerdonio *et al.*, "Status of the AURIGA gravitational wave antenna and perspectives for the *Prepared for Edoardo Amaldi Meeting on Gravitational Wave Experiments, Rome, Italy, 14-17 Jun 1994*

[2] Zeilik, M., Gregory, S., Introductory Astronomy and Astrophysics (Saunders College Publishing), 1998.

[3] Schutz, Bernard F. A First Course in General Relativity, Cambridge University Press 1985.

[4] Foster, J. and Nighingale, J.D. A Short Course In General Relativity, Springer-Verlag 1995.

[5] C. W. Misner, K. Thorne, J. A. Wheeler, *Gravitation* (W. H. Freeman, New York, 1973).

[6] Seader, S., Multi-Interferometer Search Methods For Gravitational Waves, WSU 2005.

[7] K. S. Thorne, *Prepared for 17th Texas Symposium on Relativistic Astrophysics, Munich, Germany, 12-17 Dec 1994*

[8] Miller, C., Binary Sources Of Gravitational Radiation, NASA's GWSS UTB 2005.

[9] P. C. Peters, Phys. Rev. **136**, B1224 (1964).

[10] P. C. Peters and J. Mathews, "Gravitational radiation from point masses in a Keplerian orbit," Phys. Rev. **131**, 435 (1963).

[11] NASA GSFC LISA Exhibit

http : //imagine.gsfc.nasa.gov/docs/features/exhibit/lisa_exhibit.html

[12] Arnaud, N., Angular coverage of gravitational wave detectors: network status and detection potential for burst signals, ELBA Workshop May 2002.

[13] P. Jaranowski and A. Krolak, "Optimal solution to the inverse problem for the gravitational wave signal Phys. Rev. D **49**, 1723 (1994).

[14] R. A. Hulse and J. H. Taylor, Astrophys. J. **195**, L51 (1975).

[15] N. Seto, Phys. Rev. Lett. **87**, 251101 (2001) [arXiv:astro-ph/0111107].

[16] A. Prince, M. Tinto, L. Larson and W. Armstrong, Phys. Rev. D **66**, 122002 (2002) [arXiv:gr-qc/0209039].

[17] M. Tinto and J. W. Armstrong, Phys. Rev. D **59**, 102003 (1999).

[18] A similar statistic has been obtained independently by Krolak *et. al.* recently [19]. Their method of analytically maximizing over four source parameters is manifestly. Finally, in our statistic we have retained the effect of the Doppler shift in the source emission frequency. When this effect is dropped, our (likelihood ratio) statistic is the same as is Ref. [19].

[19] A. Krolak, M. Tinto and M. Vallisneri, "Optimal filtering of the LISA data," arXiv:gr-qc/0401108.

[20] S. V. Dhurandhar, K. Rajesh Nayak and J. Y. Vinet, Phys. Rev. D **65**, 102002 (2002) [arXiv:gr-qc/0112059].

[21] K. R. Nayak, S. V. Dhurandhar, A. Pai and J. Y. Vinet, Phys. Rev. D **68**, 122001 (2003) [arXiv:gr-qc/0306050].

[22] K. R. Nayak, A. Pai, S. V. Dhurandhar and J. Y. Vinet, Class. Quant. Grav. **20**, 1217 (2003) [arXiv:gr-qc/0210014].

[23] "Lisa: A Cornerstone Mission for the Observation of Gravitational Waves," System and Technology Study Report, 2000.

[24] A. Pai, S. Dhurandhar and S. Bose, inspiraling compact binaries with a network of laser-interferometric Phys. Rev. D **64**, 042004 (2001) [arXiv:gr-qc/0009078].

[25] C. W. Helstrom, *Statistical Theory of Signal Detection* (Pergamon Press, London, 1968).

[26] B. J. Owen, Phys. Rev. D **53**, 6749 (1996). (gr-qc/9511032)

[27] S. Bose, A. Pai and S. V. Dhurandhar, Int. J. Mod. Phys. D **9**, 325 (2000) [arXiv:gr-qc/0002010].

[28] For an explanation on what the FFT algorithms are and how they work see, e.g.: W. H. Press, S. A. Teukolsky, W. T. Vellerling, and B. P. Flannery, "Numerical Recipes in C," (Cambridge University Press, second edition, 1993)

[29] C. Cutler, Phys. Rev. D **57**, 7089 (1998).

[30] R. Takahashi and N. Seto, Astrophy. J. **575**, 1030 (2002).

[31] S. Bose and A. Rogan, *in preparation.*

[32] H. K. Chaurasia and M. Bailes, "On the Eccentricities and Merger Rates of Double Neutron Star Binaries and Astrophys. J. **632**, 1054 (2005) [arXiv:astro-ph/0504021].

[33] A. V. Gusev, V. B. Ignatiev, A. G. Kuranov, K. A. Postnov and M. E. Prokhorov, "Broad-band gravitational-wave pulses from binary neutron stars in Astron. Lett. **28**, 143 (2002) [arXiv:astro-ph/0111066].

[34] Jones, D. I., Astrophy. J. **618**, L115 (2005).

[35] G. Nelemans, L. R. Yungelson and S. F. Portegies Zwart, "The gravitational wave signal from the galactic disk population of arXiv:astro-ph/0105221.

[36] C. Cutler and B. F. Schutz, Phys. Rev. D **72**, 063006 (2005) [arXiv:gr-qc/0504011].

[37] "LISA: A Cornerstone Mission for the Observation of Gravitational Waves," System and Technology Study Report, 2000.

[38] H. K. Chaurasia and M. Bailes, Astrophys. J. **632**, 1054 (2005) [arXiv:astro-ph/0504021].

[39] T. Damour and N. Deruelle N., Phys. Theor., 43, 107 (1985)

[40] S. Mikkola, Celestial Mechanics, 40, 329 (1987)

[41] D. I. Jones, Astrophy. J. **618**, L115 (2005).

[42] M. J. Benacquista, 2002, Class. Quant. Grav., 19, 1297 (2002)

[43] A. V. Gusev, V. B. Ignatiev, A. G. Kuranov, K. A. Postnov and M. E. Prokhorov, Astron. Lett. **28**, 143 (2002) [arXiv:astro-ph/0111066].

[44] M. J. Benacquista, 2002, Class. Quant. Grav., 19, 1297 (2002)

[45] T. Damour, A. Gopakumar and B. R. Iyer, Phys. Rev. D **70**, 064028 (2004) [arXiv:gr-qc/0404128].

[46] C. Konigsdorffer and A. Gopakumar, "Parametric derivation of the observable relativistic periastron advance for Phys. Rev. D **73**, 044011 (2006) [arXiv:gr-qc/0509012].

[47] M. Tessmer and A. Gopakumar, "Accurate and efficient gravitational waveforms for certain galactic compact objects," submitted for publication.

[48] P. Jaranowski, A. Krolak and B. F. Schutz, "Data analysis of gravitational-wave signals from spinning neutron stars. Phys. Rev. D **58**, 063001 (1998) [arXiv:gr-qc/9804014].

[49] A. Rogan and S. Bose, "Optimal statistic for detecting gravitational wave signals from binary Class. Quant. Grav. **21**, S1607 (2004) [arXiv:gr-qc/0407008], www.iop.org/journals.cqg.

[50] A. Rogan and S. Bose, "Parameter estimation of binary compact objects with LISA: Effects of arXiv:astro-ph/0605034.

[51] A. Vecchio and E. D. L. Wickham, Phys. Rev. D **70**, 082002 (2004) [arXiv:gr-qc/0406039].

[52] P. L. Bender, et al., *LISA Pre-Phase A Report; Second Edition*, MPQ 233 (1998).

[53] B. Abbott *et al.* [LIGO Scientific Collaboration], Nucl. Instrum. Meth. A **517**, 154 (2004) [arXiv:gr-qc/0308043].

[54] F. Acernese *et al.*, Class. Quant. Grav. **22**, S869 (2005).

[55] M. Ando *et al.* [TAMA Collaboration], Class. Quant. Grav. **22**, S881 (2005).

[56] B. Willke *et al.*, Class. Quant. Grav. **19**, 1377 (2002).

[57] N. Mio [LCGT Collaboration], Prog. Theor. Phys. Suppl. **151**, 221 (2003).

[58] C. Cutler and K. S. Thorne, arXiv:gr-qc/0204090.

[59] K. R. Nayak, S. V. Dhurandhar, A. Pai and J. Y. Vinet, Phys. Rev. D **68**, 122001 (2003) [arXiv:gr-qc/0306050].

[60] P. L. Bender and D. Hils, Class. Quant. Grav. **14**, 1439 (1997).

[61] D. Hils & P. L. Bender, ApJ **537**, 334 (2000).

[62] G. Nelemans, L. R. Yungelson & S. F. Portegies Zwart, A&A **375**, 890 (2001).

[63] N.J. Cornish & S.L. Larson, Phys. Rev. D**67**, 103001 (2003).

[64] M. S. Mohanty, & R. K. Nayak, gr-qc/0512014 (2005).

[65] J. Crowder, N. J. Cornish and L. Reddinger, Phys. Rev. D **73**, 063011 (2006) [arXiv:gr-qc/0601036].

[66] C. Cutler, Phys. Rev. D **57**, 7089 (1998).

[67] R. Takahashi and N. Seto, Astrophy. J. **575**, 1030 (2002).

[68] B. F.Schutz, Nature **323**, 310 (1986).

[69] L. Barack and C. Cutler, Phys. Rev. D **69**, 082005 (2004) [arXiv:gr-qc/0310125].

[70] J. W. Armstrong, F. B. Estabrook, and M. Tinto, Astrophys. J., **527**, 814 (1999).

[71] M. Tinto, F. B. Estabrook, and J. W. Armstrong, Phys. Rev. D **65**, 082003 (2002).

[72] Note that the indices i and $i\pm1$ can take only 1, 2, and 3 as values. These three numbers are ordered clockwise in Fig. 4.1. By convention, whereas $i+1$ equals the number next to i while going clockwise in that figure, $i-1$ equals the number preceding i. E.g., when $i=3$, we take $i-1=2$ and $i+1=1$; when $i=1$, we take $i-1=3$ and $i+1=2$.

[73] These combinations are identical to $X^{(3)}$, $X^{(4)}$, and $-X^{(1)}+\zeta_3 X^{(2)}$, respectively, used by Dhurandhar et al. in Ref. [20].

[74] There is a typographical error in Eq. (18) of Ref. [49]: In the expression for $P^{(3)}(f)$, the $\cos(2\pi fL)$ factor should appear as squared.

[75] N. J. Cornish and R. W. Hellings, Class. Quant. Grav. **20**, 4851 (2003) [arXiv:gr-qc/0306096].

[76] D. A. Shaddock, M. Tinto, F. B. Estabrook and J. W. Armstrong, Phys. Rev. D **68**, 061303 (2003) [arXiv:gr-qc/0307080].

[77] M. Tinto, F. B. Estabrook and J. W. Armstrong, Phys. Rev. D **69**, 082001 (2004) [arXiv:gr-qc/0310017].

[78] M. Tinto, 8th Anual Gravitational Wave Data Analysis Workshop, (2003).

[79] M. Gel'fand, R. A. Minlos, and Z. Ye. Shapiro, *Representations of the Rotation and Lorentz Groups and their Applications* (Pergamon Press, New York, 1963).

[80] P. Jaranowski and A. Krolak, Living Rev. Rel. **8**, 3 (2005).

[81] S. Bose and A. Rogan, *In preparation.*

[82] Gonzalez, G., et. al., "Calibration of LIGO Detectors for S2" LSC Distribution Draft 2004.

[83] S. W. . Hawking and W. . (. Israel,

[84] Brown, D., et. al., "Specifications for Storing Calibration Data for LIGO" LSC Distribution Draft 2005.

[85] Brown, D., "Searching for Gravitational Radiation from Black Hole MACHOS in the Galactic Halo", UWM 2004.

[86] B. Allen, W. G. Anderson, P. R. Brady, D. A. Brown and J. D. E. Creighton, "FINDCHIRP: An algorithm for detection of gravitational waves from arXiv:gr-qc/0509116.

[87] B. Abbott *et al.* [LIGO Scientific Collaboration], "Search for gravitational waves from primordial black hole binary Phys. Rev. D **72**, 082002 (2005) [arXiv:gr-qc/0505042].

[88] B. Abbott *et al.* [LIGO Scientific Collaboration], "Search for gravitational waves from galactic and extra-galactic binary Phys. Rev. D **72**, 082001 (2005) [arXiv:gr-qc/0505041].

[89] B. Abbott *et al.* [LIGO Scientific Collaboration], "Search for gravitational waves from binary inspirals in S3 and S4 LIGO data," submitted for publication.

[90] B. Abbott *et al.* [LIGO Scientific Collaboration], Phys. Rev. D **69**, 122001 (2004) [arXiv:gr-qc/0308069].

[91] B. Abbott *et al.* [LIGO Scientific Collaboration], "Search for gravitational waves from binary black hole inspirals in LIGO Phys. Rev. D **73**, 062001 (2006) [arXiv:gr-qc/0509129].

[92] V. Kalogera, R. Narayan, D. N. Spergel and J. H. Taylor, Astrophys. J. **556**, 340 (2001) [arXiv:astro-ph/0012038].

[93] A. Bertolini *et al.*, "Recent progress on the R & D program of the seismic attenuation system Nucl. Instrum. Meth. A **461**, 300 (2001).

[94] T. Creighton, Class. Quant. Grav. **20**, S853 (2003).

[95] J. Mason and P. Willems, *Prepared for 3rd Edoardo Amaldi Conference on Gravitational Waves (Amaldi 99), Pasadena, California, 12-16 Jul 1999*